NTNU

Norwegian University of
Science and Technology

Investigations of $Pd_3Au(100)$ as a catalytic model system

Gaute Osaland Hådem

Nanotechnology
Submission date: July 2018
Supervisor: Hilde Johnsen Venvik, IKP
Co-supervisor: Ingeborg-Helene Svenum, SINTEF
Mehdi Mahmoodinia, IKP
Marie Døvre Strømsheim, IKP

Norwegian University of Science and Technology
Department of Chemical Engineering

This page is intentionally left blank

This thesis is typeset using LaTeX and KOMA-Script report-class. Sketches and illustrations are created with PGF/Ti*k*Z, Autodesk Fusion 360 or ASE, and data plots with PGFPLOT. The thesis is intended to be printed in color.

Abstract

Catalysts are defined as materials that lowers the activation energy of a reaction, without being consumed. In heterogeneous catalysis they are commonly transitions metals which have been refined to small particles using various methods and are embedded on a oxide support. Since heterogeneous catalysis is a surface phenomenon, one way of studying interaction between reactive gases and the catalysts is by employing single crystals of the same metal as a model system and study these under ultra-high vacuum conditions (UHV). This study aims at investigating the Pd_3Au model system with orientation (100) to gain a better understanding of how the composition in the surface region changes with temperature and exposure to hydrogen and oxygen gas. It is crucial to predict and control the amount of palladium (Pd) and gold (Au) in the surface when Pd-Au systems are employed as catalysts for CO oxidation and used as a hydrogen permeable membrane.

Investigations were performed using both theoretical and experimental methods. First-principle calculations were performed using Density Functional Theory and experimental investigations involved x-ray photoelectron spectroscopy (XPS) with a fixed photon energy, high-resolution XPS with synchrotron radiation, low-energy electron diffraction (LEED) for determination of the average surface structure and local investigations on the surface were performed with scanning tunnelling microscopy (STM).

From first-principle calculations, various terminations of the $Pd_3Au(100)$ surface were calculated and the effect of carbon on the surface and in the subsurface determined. The most stable surface in vacuum was found to be Au terminated with a surface energy of 79.12 meV/Å^2, while the least stable was the Pd terminated with a surface energy of 110.27meV/Å^2. The adsorption energy of carbon is found to increase with increasing Pd coverage. To determine the reason for this increase in adsorption energy, the d-band model proposed by Hammer and Nørskov [1] was employed and the calculated d band center shifts towards the Fermi level with an increasing amount of Pd adjacent to the adsorbed carbon, in agreement with the increasing adsorption energy. This is caused by Pd having d-band center closer to the Fermi level, making them more reactive.

Experimental investigations involved hydrogenation of the sample and through characterization by XPS it was revealed that at 300 °C, hydrogenation of residual carbon on the surface is occurring. This also coincided with the lowest amount of Au measured, which indicates that there is a preferential segregation of Pd to the surface under these conditions. Investigations with HRXPS after exposing the surface to large amounts of oxygen caused a preferential segregation of Pd to the surface with Au being found below the surface. Heating the sample to 200 °C causes desorption of oxygen found on the surface, but does not significantly cause migration of Au to the surface. Further heating to 300 °C causes segregation of Au to the surface, but there is still Pd in the topmost layer. Finally, heating to 500 °C causes the surface to become covered with Au and Pd is found in layers below. From valence band measurements obtained after annealing to 300 and 500 °C, the center of the band has a shift to higher energies with higher temperature, caused by more Au in the surface. This is in agreement with the calculations performed. Using the scanning tunnelling microscope (STM), it is found that the surface is highly stepped with many clusters on the surface after exposure to large amounts of oxygen. The origin of these clusters and what they are made of is still unclear.

Based on the findings in this report, the termination of the $Pd_3Au(100)$ was found to be important to control in order to have a reactive surface. H_2 and O_2 exposure at elevated temperatures caused more Pd to be found in the surface and the temperature range and pressure of the reactive gases is important to control in order to have reactive Pd sites in the surface.

Sammendrag

Katalysatorer er definert som materialer som senker aktiveringsenergien for en kjemisk reaksjon uten selv å bli konsumert i reaksjonen. I heterogen katalyse benyttes vanligvis innskuddsmetaller som har blitt produsert til små partikler og som sitter på en bærer, typisk et oksid. Heterogen katalyse er et overflatefenomen og en metode for å studere interaksjonen mellom gasser og metallet på, er å ta i bruk enkrystaller av det samme materialet brukt i reaksjonen man vil undersøke og studere disse i et ultra-høy vakuum-miljø. Denne studien har som mål å studere Pd_3Au-sysemet med (100) orientering for bedre å forstå hvordan komposisjonen i overflaten endres med temperatur og eksponering til hydrogen- og oksygengass. Det er viktig å forutse og kontrollere mengded palladium (Pd) og gull (Au) i overflaten når systemer av Pd-Au benyttes som katalysatorer i oksidasjon av CO og som permeable membraner for hydrogenproduksjon.

Undersøkelser ble utført med både teoretiske beregner og experimentelle teknikker. Følgende eksperimentelle metoder ble brukt: røntgenfotoemisjonsspektroskopi (XPS), høyoppløst XPS med varierende fotonenergi, lav-energi elektrondiffraksjon (LEED) for bestemmelse av overfatestruktur og sveipetunnelleringsmikroskop (STM) for undersøkelser på nanoskala.

Ab initio beregninger er utført ved å bruke tetthetsfunksjonalteori hvor forskjellige termineringer av $Pd_3Au(100)$ overflaten har blitt beregnet og effekten av adsorbert karbon på overflaten og karbon som befinner seg rett under overflaten har blitt studert. Den mest stabile overflaten av Pd_3Au (100) er den som er fullstendig dekket av Au, med en overflateenergi på 79.12 meV/Å^2. Den minst stabile overflaten er fullstendig dekket av Pd og har en overflateenergi på 110.27 meV/Å^2. Adsorpsjonsenergien for karbon øker med økende antall Pd atomer i overflaten og for å forstå grunnen til dette har man studert elektronstrukturen til overflateatomene gjennom d-båndmodellen av Hammer og Nørskov [1]. Grunnen til den økende adsorpsjonsenergien er at d-båndsenteret forflytter seg nærmere Ferminivået når det er et økende antall Pd-atomer i overflaten. Dette skyldes elektronstrukturen til Pd som har flere elektroner tilgjengelig nærmere Ferminivået, noe som gjør dem mer reaktive.

Eksperimentelle undersøkelser involverte hydrogenering av modellsystemet og fra målinger utført med XPS ble det påvist betraktelig redusering av karbon på overflaten ved 300 °C. Her ble også den laveste konsentrasjonen av Au målt, noe som indikerer at det er foretrukken segregering av Pd-atomer til overflaten under disse reaksjonsbetingelsene. Ved å eksponere overflaten til oksygen og utføre målinger med HRXPS, er overflaten dekket av Pd og Au er funnet i lagene under overflaten. Oppvarming til 200 °C gjør at oksygenet på overflaten desorberer, men forårsaker ikke betraktelig segregering av Au til overflaten. Videre oppvarming til 300 °C gjør at Au segregerer til overflaten, men det er fortsatt Pd atomer til stede. Oppvarming til 500 °C gjør at overflaten blir fullstendig dekket av Au, mens Pd er tilstede i lagene under overflaten. Ved å måle valensbåndene etter oppvarming til 300 og 500 °C, viser senteret seg å skifte til høyere energi med en økende andel Au i overflaten. Dette er i samsvar med beregningene som er utført. Ved å studere overflaten med sveipetunneleringsmikroskopi (STM) etter okysgeneksponering viser overflaten seg å være svært lagvis med mange klynger til stede. Hva disse klyngene består av er fortsatt uvisst.

Basert på funnnene i denne oppgaven, er det viktig å kontrollere mengden Au/Pd i overflaten for å kunne ha en reaktiv overflate. Eksponering til H_2 og O_2 ved høyere temperaturer fører til segregering av Pd til overflaten, men både trykk og hvor høy temperaturen er spiller en stor rolle for mye Pd man får i overflaten.

Preface

This thesis is submitted in partial fulfillment of the requirements for the degree of Master of Science in Nanotechnology at the Department of Chemical Engineering (IKP) at the Norwegian University of Science and Technology (NTNU). This work is a continuation of a project performed in the Fall of 2017, where the same system was investigated. Part of the work is reused here, especially sections of the theory chapter. This project builds upon previous work on catalytic model systems at the NTNU Department of Chemical Engineering and Department of Physics, where $Pd_{75}Ag_{25}$ (100) and Pd_3Au(100) have been studied extensively [2–7].

Everything presented is entirely the work of the author, with the exception of some figures where the reference to the source is mentioned.

Acknowledgements

I am grateful for the help and support from several people during this project, which has been a truly exciting and meaningful journey into the world of catalysis and surface science. Firstly, I thank my supervisor Prof. Hilde J. Venvik for letting me take on this project from several different angles, prioritizing her students in a busy schedule and allowing me to join the group when we went to Aarhus for synchrotron experiments.

Secondly, I thank my fantastic co-supervisors. Thanks to Mari Helene Farstad, former post doc. at IKP, for the excellent training I received in using ultra-high vacuum instruments.

Thanks to Ingeborg-Helene Svenum from SINTEF for the training I received in using the XPS, analysis of the results and also teaching me the first steps about atomistic calculations. I wish you all the best as an Associate Professor II at NTNU.

Thanks to post doc. Marie Døvre Strømsheim for sharing her knowledge about STM, the discussions about synchrotron results and for very good feedback in the writing process with this thesis.

Thanks to Mehdi Mahmoodinia for all the time we've spent at the XPS and STM lab doing experiments together, while discussing various calculations and for your help in interpreting the results from the calculations performed. Your help truly accelerated my learning process.

This thesis concludes my five years at NTNU, and I am grateful to have been part of MTNANO 2018 these five years. Thank you for broadening my horizon in so many aspects, the heated discussions and all the fun we've had together!

This project is part of iCSI - industrial Catalysis Science and Innovation, appointed by the Research Council of Norway. Computational resources were provided by NOTUR and performed at the Stallo cluster.

Gaute Osaland Hådem
Trondheim, July, 2018

Contents

List of Figures

List of Tables

Chapter 1.

Introduction

One of the long-time goals of surface science is a better comprehension of oxygen interaction with metal surfaces to develeop more effective heterogeneous catalysts [8]. The oxidation of carbon monoxide (CO) on platinum-group metals is possibly the most investigated catalytic reaction in surface science and a reaction which serves as a model for more complex reactions [9–13]. The formation of thin surface oxides on late transition metals has been discovered, and the high activity for CO oxidation on Platinum (Pt), Palladium (Pd), and Rhodium (Rh) coincides with the formation of thin surface oxides [9, 10, 14, 15]. Since most metals are oxidized under reaction relevant conditions, understanding how these oxides affects the catalytic properties is important in order to develop more efficient catalysts [16].

1.1. Model catalysts

Catalysis is a microscopic phenomenon which is exploited in chemical reactions and an essential technology for our society in that around 90% of all chemicals worldwide are produced using it [17]. The definition of a catalyst is something that reduces the activation energy barrier between the reactants and the products, without being consumed. It is a highly dynamic reaction where the surface of the solid catalyst is continually changing due to adsorption, desorption, segregation and diffusion mechanisms. To be able to explain what is going on at the surface of a catalyst, a simplified model system involving single crystals of the catalytic material are studied under ultra-high vacuum (UHV) conditions. Significant progress has been made in the understanding of adsorbate-adsorbate and adsorbate-substrate interactions by studying the surface of such systems with atomic resolution. It has been suggested that it may not be the bare metal surface, but rather its oxidized form which is the most active phase under the same conditions as in real-world catalytic oxidation reactions [9, 18, 19].

In practical applications of oxidation catalysis, oxygen reacts with the metal to create a metal oxide layer on the metal surface. This oxide layer represents an entirely new compound and since oxides have very different chemical properties compared to their parent metals, the transformation of a metal surface to a metal oxide can cause a large change in the catalytic performance of the metal. Since metal oxidation occurs while the catalyst is operating in realistic gaseous environments, understanding the growth and chemical properties of oxide layers on transition metals is essential [20]. This is important for bridging what is termed the pressure gap [21]. The "pressure gap" is what separates UHV and technical catalytic investigations. Over the last decades a growing number of experimental techniques have been adapted to bridge this gap in order to obtain insight on the atomic scale about the structure, composition and other properties of model catalyst surfaces under near realistic conditions. Examples of these novel techniques are Scanning Tunneling Microscopy (STM) [10, 19, 22], Surface X-ray Diffraction [23, 24] and near ambient/high pressure X-ray Photoelectron Spectroscopy (XPS) [12]. The working principle behind STM and XPS equipment is explained more thoroughly in the Theory chapter. In addition to bridge the "pressure gap", there is also a need to bridge what is termed the "material gap". Modelling catalysts with single crystals has enhanced our understanding of several reaction categories, but despite its success there is a need to develop models with higher level of complexity closer to the catalysts applied in actual reactions. A specific issue is related to how very small metal particles interact with the ambient and the interactions between the metal particle and the support [25].

1.2. Palladium alloys

Palladium (Pd), atomic number 46, is used as a catalyst in a wide array of different reactions. It can be used for oxidation of hydrocarbons in automotive exhaust [26, 27] and as a catalyst for combustion of methane [28, 29]. It is also the most promising metal for hydrogen permeable membranes as it has the ability to dissociate molecular hydrogen into monatomic form for diffusion through its lattice. Pure Pd has been a research topic as a catalyst for direct synthesis of hydrogen peroxide for many years with the first reported study in 1914 [30]. The effect of alloying Pd with other transition metals such as copper (Cu), silver (Ag) and gold (Au) have been studied for a wide array of chemical reactions, some of which are explained in the following sections.

Oxidation of CO and hydrocarbons

The use of fossil fuels for internal combustion engines creates emissions that have environmental and health implications as hydrocarbons, nitrogen oxides and CO are released. Incomplete combustion of gasoline and diesel creates CO and unburned hydrocarbons as well as soot. Pd-Au bimetallic alloys is a promising material for low-temperature oxidation of CO as Pd dissociates O_2, and Au adsorbs CO under reaction conditions [31]. Large Au particles as well as bulk Au do not activate O_2 as no oxidation is observed between molecular CO and molecular O_2 on pure Au surfaces. However, theoretical calculations have predicted that Au nanoparticles have the ability to oxidize CO even below room temperature [32], thus making a surface composed of Pd and Au highly interesting from a catalytic perspective as one can have independent sites of single Pd or Au atoms embedded in it. By varying the temperature, pressure and/or chemical environments the elemental and chemical compositions of the Pd-Au alloy surfaces can be altered. To have the best synergistic effect of alloying Pd with Au, it is crucial to predict and control the amount and distribution of Au in the surface [31, 33].

Hydrogen separation

Thomas Graham discovered in 1866 that Pd is capable of absorbing approximately 600 times its own volume in hydrogen while still maintaining its structural integrity and physical properties [34]. Its high selectivity, permeability and solubility for hydrogen makes it a suitable material for hydrogen separation. This is because Pd and its alloys have the ability to allow monatomic hydrogen to selectively diffuse through its structure to produce purities in excess of 99.9999 % [35].

Pure Palladium suffer from effects of embrittlement due to a disparity between the α- and β-hydride phase lattice parameters. This can lead to internal stresses and cause membrane failure [36]. The obvious drawback of using pure Pd is the inherent material cost, where its price has rapidly risen over the last years. As a result of the large interest in Pd and its increasing price, research aims have been geared towards developing Pd alloy membranes that contain as little Pd as possible without sacrificing the membrane properties. Several elements such as Ag, Au, Cu and Pt can be alloyed with Pd to form substitutional solid solutions which can lower the critical temperature of the phase transformation between α and β hydride phases below room temperature [37].

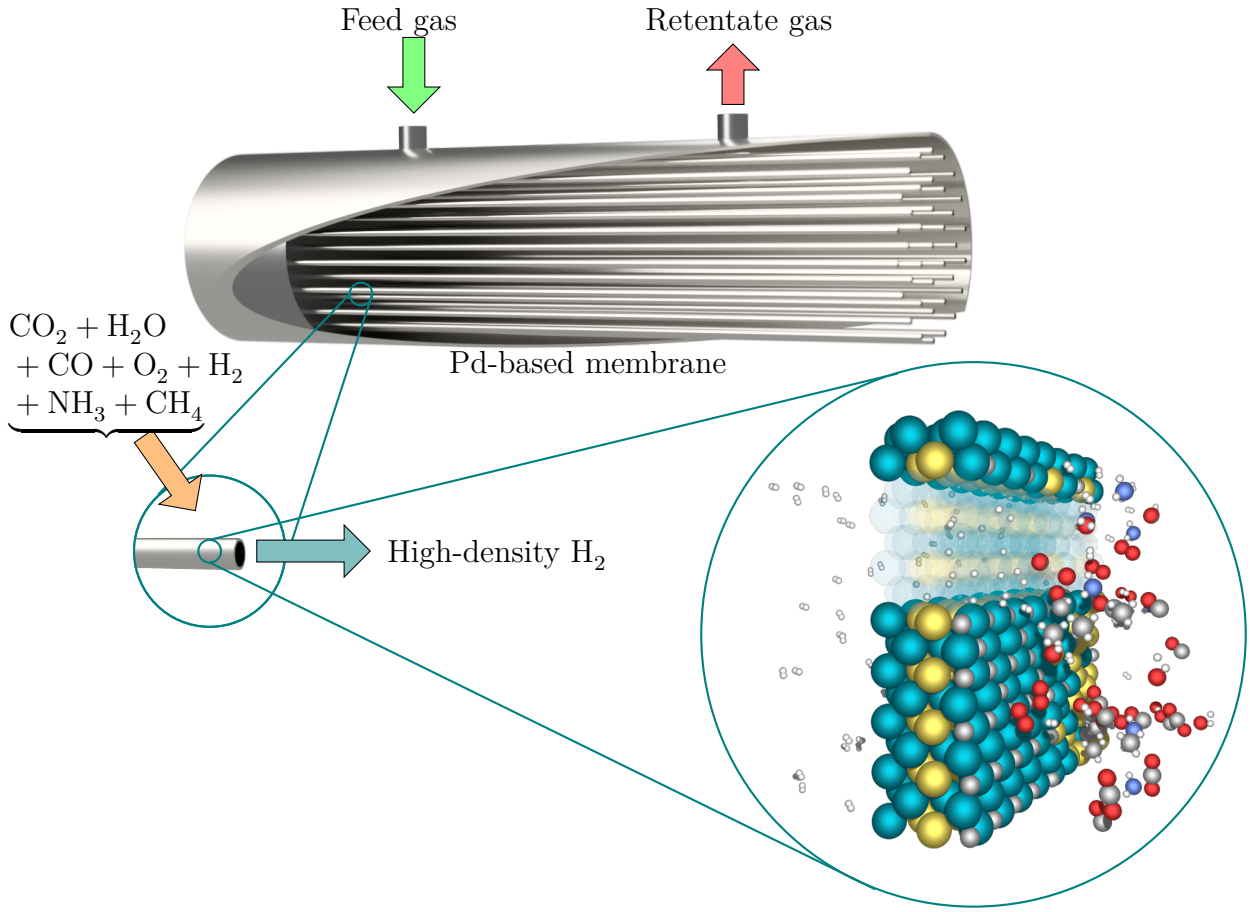

Figure 1.1.: Sketch of a proposed Pd tube bank (small rods) with thin palladium alloy membrane purifiers for high-density hydrogen production. Small inset shows a section of one tube. Large inset: Atomistic sketch of a hydrogen permeable membrane of Pd_3Au. H_2 gas molecules are adsorbed, dissociated and able to diffuse through the membrane to the low pressure and H_2 rich side while the other molecules are restricted. Atomic color code: Oxygen (red), carbon (gray), palladium (blue), gold (yellow), nitrogen (light blue), and hydrogen (white).

1.3. Previous work

This thesis is a continuation of the specialization project performed in the fall of 2017 by the author where Pd_3Au (100) single crystals were investigated using LEED, STM and XPS. In XPS, the sample was measured at both normal and grazing emission angle (60°) to be more surface sensitive. Results from this project showed a large increase of carbon in the surface region as a result of annealing temperature and annealing time, seen in Figure 1.2.

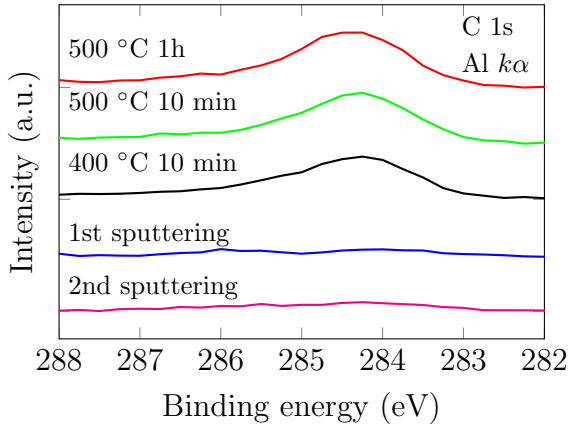

Figure 1.2.: XP spectrum of C 1s showing the increasing amount of carbon in the surface region of a $Pd_3Au(100)$ single crystal with increasing annealing temperature and time.

1.4. Objectives

The scope of this project is to investigate the surface of a $Pd_3Au(100)$ catalytic model system to gain a better understanding of the phenomena occurring on the catalytically active surface during oxidation and hydrogenation reactions. Focus is put on gaining a better understanding of how the surface composition is affected by temperature treatments and exposure to hydrogen and oxygen gas through experimental investigations. Due to the increasing amount of C found in the surface by annealing from previous investigations, adsorption of carbon and how this affect the stability and reactivity of the surface is explored using first-principle calculations.

Thesis overview

Chapter 2 contains the necessary information in order to develop a thorough understanding of the physical phenomena observed on catalytic model systems and the working principle behind the characterization methods used are explained.

Chapter 3 explains the theory behind the computational methods, while Chapter 4 explains the computational methods, how to interpret the results and implementation.

Chapter 5 explains the experimental methods, i.e. how the experimental results were acquired and analysed.

Chapter 6 gives an introduction to the material system.

Chapter 7 presents the findings from calculations with the experimental findings followed thereafter in Chapter 8. To aid in the readability of the thesis, the results obtained from various methods are presented and discussed for themselves.

Chapter 9 concludes the results obtained in this project and suggests topics that are of relevance for future work.

Chapter 2.

Theory

This chapter explains the theory behind the physical phenomena observed in the work with this project and the physical principles behind the experimental techniques used. Much of the theory describing surface related phenomena is based on introductory books in surface science, where Prutton [38], Hudson [39] and Kolasinski [40] are most used. As natural when treating surface related phenomena, a general description of surfaces and alloys is given. From there, the growth of thin films on surfaces is discussed, how adsorbates form structures and how the underlying substrate affects the morphology of the adsorbate and vice versa. In order to characterize these surfaces, the working principle behind the characterization techniques are presented with a major focus on XPS. This chapter is written with the goal of developing intuition about catalytic model systems and how to characterize them. Parts of this chapter is adapted from the project performed prior to this thesis.

2.1. Catalytic model systems

2.1.1. Surfaces

The surface of a solid is inherently different from the rest of the solid. On a macroscopic scale they can appear flat and smooth, but at the atomic level they are usually complex and highly anisotropic landscapes that are far from being the ideal defect-free surface.

In surface science one can subdivide surfaces into three subdivisions; clean surface, surface in the presence of an adsorbate and the surface of the adsorbate. Among clean surface structures, ideal flat surfaces are the result of cleaving the bulk structure of a perfect crystal. The atoms residing on the surface have broken bonds which puts them in a higher energy configuration compared with the bulk atoms.

The surface free energy γ is related to the cohesive energy of the solid ΔH_{coh} and

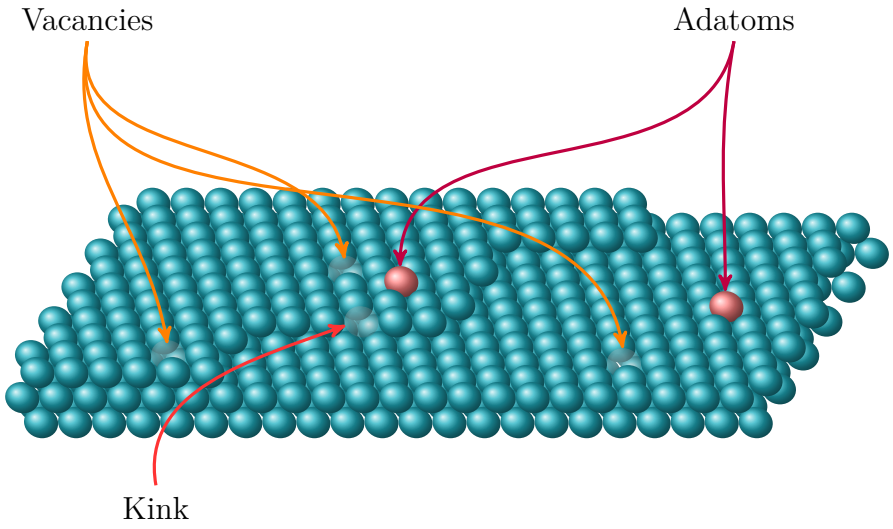

Figure 2.1.: A stepped surface with adatoms, kinks and vacancies.

to the number of new dangling bonds which were created when the bulk structure was cleaved.

$$\gamma = \Delta H_{\text{coh}} \frac{Z_s}{Z} N s, \tag{2.1}$$

where Z_s is the number of dangling bonds of a surface atom, Z is the coordination number of a bulk atom and N_s is the surface density of atoms.

Structures made by cutting a crystal along a higher index (surfaces with h, k or $l > 1$) will expose second and third layer of atoms. A small miscut angle leads to viscinal surfaces which are not perfect flat surfaces, and the surface cannot maintain the perfect (hkl) structure over long distances. In order to stay as close to a low index structure as possible, while still maintaining the macroscopic surface structure, step-like discontinuities are formed on the surface. These viscinal surfaces are composed of terraces and steps and termed *stepped surfaces*. Step edges are considered defects as they cause the surface to deviate from a perfect surface. Point defects can be found on both terraces and step edges. Most common are vacancies, which are lattice points with a missing atom. An illustration of a stepped surface with terraces, kinks, adatoms and vacancies is seen in Figure 2.1.

2.1.2. Bimetallic alloys

The degree of segregation or mixing and atomic ordering in alloys depends on several factors. The relative strengths of A-A, B-B and A-B bonds, determines to a first ap-

proximation if the alloy favours mixing or segregation. If A-B bonds are strongest, then alloy formation will be exothermic, thus mixing is favourable. Surface energies of the bulk elements present determines which element tends to segregate to the surface and to the bulk. Adsorbing gas will affect which of the components in the alloy that segregates to the surface, and the element forming the strongest bond with the adsorbate will be enriched at the surface [41–43]. To form an intermetallic compound, the relative atomic sizes are important for determining whether lattice strain influences the segregation behaviour. If there's a large mismatch in atomic radii, surface segregation is expected for intermetallic compounds.

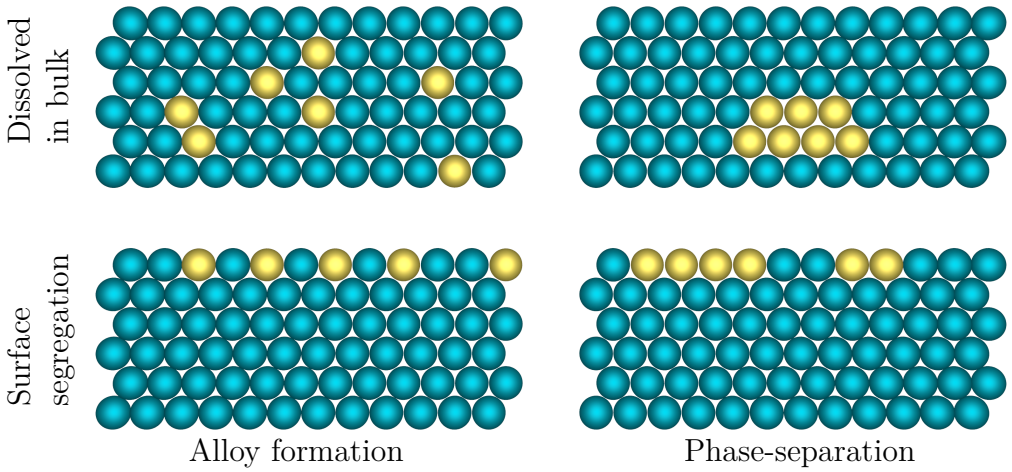

Figure 2.2.: Top: Alloy formation and phase-separation for minority atoms dissolved in the bulk. Bottom: Alloy formation and phase-separation for minority atoms which segregates to the surface.

2.1.3. Thin film growth modes

The equilibrium shape of the adsorbate deposited on the substrate depends on the energy balance between the surface free energies of the adsorbate and substrate. Depending on their values, three growth modes are accessible, resulting in different morphologies. The amount of new material from the gas phase that can adsorb on a surface is described by Equation (2.2). When a particle has condensed on the surface, it might diffuse across the surface or re-evaporate. The diffusion might lead to adsorption, particularly at energetically favourable sites, such as edges or other defects.

There are three different modes, illustrated in Figure 2.3, of film growth observed and they can be explained from thermodynamic and surface free energies, γ, of the interfaces present. Which growth mode is favourable depends on adsorbate-adsorbate and

Figure 2.3.: The three growth modes.

adsorbate-substrate interactions, lattice mismatch, strain, pressure and temperature. The three growth modes observed are:

- Frank-van der Merve (FM): Layer-by-layer growth
- Stranski-Krastanov (SK): Layer-plus-island growth
- Vollmer-Weber (VW): Island growth

2.1.4. Adsorption

From a kinetic point of view, the rate of molecular impingement I (molecules/cms) can be developed from the kinetic theory of gasses, also known as the *Hertz-Knudsen equation*, and states as

$$I = \frac{dN}{dt} = \frac{p}{\sqrt{2\pi m k_B T}}. \tag{2.2}$$

Where m is the mass of a particle (kg), p the pressure (Pa), k_B Boltzmann's constant and T the temperature (K). When a gas molecule approaches a surface it will experience an initial attractive force, which will increase to a maximum and further decrease at even closer distances as repulsive forces starts to act on the molecule.

The molecule may be trapped in the position where is has the lowest potential energy. The probability to escape is given by absolute rate theory as

$$v_{\text{des}} = v_0 \exp\langle \frac{-\Delta G^*_{\text{des}}}{k_B T} \rangle, \tag{2.3}$$

where v_{des} is the desorption frequency v_0 an attempt frequency on the order of the atomic vibrational frequency of the crystal lattice. The free energy of activation for the escape process is ΔG^*_{des}. From the desorption frequency we can find the mean surface lifetime of species by taking the reciprocal:

$$\tau_a = \frac{1}{\upsilon_{\text{des}}}. \tag{2.4}$$

From Equation 2.3 and 2.4, we see that the time-averaged concentration is going to be higher near the surface than in bulk of the gas phase.

The binding energy of an adsorbate depends on its position on the surface as there are more and less energetically favourable sites. This gives rise to different binding sites which are separated by energetic barriers. The adsorbate will have to hop from one site to another by overcoming these energy barriers and motion from one potential well to another represents diffusion. For a uniform potential the surface diffusion is expected to be dictated by the Arrhenius equation

$$D = D_0 \exp\left(\frac{-E_{\text{dif}}}{RT}\right), \tag{2.5}$$

where E_{dif} is the activation energy, D_0 the pre-exponential diffusion factor, D the diffusion coefficient, R the gas constant and T the temperature (K). Equation (2.5) has two extremes which does not describe diffusion. At very low temperatures the movement of light adsorbates such as H can be governed by quantum effects [44]. The other extrema occurs when $RT \gg E_{\text{dif}}$. In this regime, the state of 2D motion on the surface is known as a *two-dimensional gas* and the adsorbed species are free to move in the x and y directions. In most cases, the temperature required to form a 2D gas is sufficiently high to cause significant desorption. For temperatures between these extremes, the adatoms moves by a random walk process with mean square distance $\langle x^2 \rangle$ over time t, given by

$$\langle x^2 \rangle = 2Dt. \tag{2.6}$$

This is for a uniform 1D potential and is particularly simple, but has several important implications. Since different sites has different binding energies, their diffusion barriers will also have different energies. This is important in understanding how adsorbates diffuse anisotropically and can lead to anisotropic structures.

When an atom adsorbs on a surface, it can become adsorbed by two different mechanisms, physiosorption and chemisorption. Physiosorption involves polarization of one or both species adjacent to each other, which results in weak van der Waal bonds and is stable only at cryogenic temperature. From a catalysis perspective, chemisorption is more interesting as it involves electron exchange and will form a much stronger bond. A thorough explanation of chemisorption and how the electronic structure changes how much an adsorbate will bond to the surface is given in Section 4.3.2 in Chapter 4.

Impinging atoms or molecules will adsorb on different sites depending on the mono-

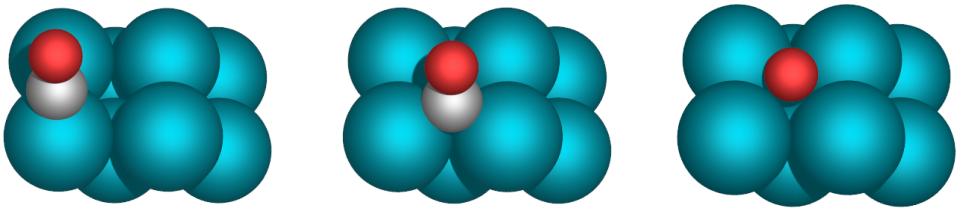

(a) CO on-top **(b)** CO bridge **(c)** O hollow

Figure 2.4.: On-top, bridge and hollow adsorption sites on a fcc(100) surface of Pd.

layer (ML) coverage and type of adsorbing specie. The most common adsorbate sites are named on-top site, bridge sites and hollow sites and are displayed in Figure 2.4. Carbon, nitrogen, oxygen and sulphur prefer sites with high coordination and are typically found on three- and four-fold positions on the surface. Depending on the gas pressure, CO will adsorb on Pd at different sites in a $Pd_{70}Au_{30}(111)$ alloy. Increasing CO gas pressure from UHV to 10 mTorr results in CO shifting from hollow and bridge sites to on-top site, even though the on top sites are energetically less favourable. This is caused by a large steric repulsion between adjacent CO molecules [45].

2.1.5. Relaxation and reconstruction

The atoms in a higher energy state on the surface belonging to the outer atomic layer(s) can be moved to new positions in a process known as *relaxation* of the surface unit cell. Surfaces of transition metals are in tension with the largest to smallest contraction reported for (110), (100) and (111) respectively [46]. The number of broken bonds are used to argue for which surface will have the largest relaxation.

When a new surface is created, the original distribution of electrons leads to a corrugated electron distribution at the surface. These electrons will re-distribute themselves to achieve a more even charge density. This creates an asymmetric charge distributions around the ions in the first layer. By a redistribution of the electron cloud, the total energy is lowered on the surface. This charge smoothing is called the Smoluchowski effect. [47]

In a reconstruction, the periodicity parallel to the surface changes with respect to that of the bulk to cope with the energetically unfavourable dangling bonds present. For transition metal surfaces, which have extended, delocalized states that correlate poorly with unoccupied/dangling bonds on a single metal atom, the low index planes can be stabilized by relaxations. However, if relaxation does not sufficiently stabilize the surface, as is the case for Au(111) and Pt(100), they will reconstruct. [40] Reconstruction

produces a modified 2D surface lattice.

A common way of describing superstructures and surface reconstructions is to express them using base vectors of the unit cell of the truncated bulk. With $\mathbf{a}_1$ and $\mathbf{a}_2$ being vectors spanning the surface unit cell of a truncated bulk lattice, the lattice vectors of the adsorbate/reconstruction unit cell on the surface, $\mathbf{b}_1$ and $\mathbf{b}_2$ are described by the matrix $\mathbf{G}$:

$$\begin{pmatrix} \mathbf{b}_1 \\ \mathbf{b}_2 \end{pmatrix} = \begin{pmatrix} G_{11} & G_{12} \\ G_{21} & G_{22} \end{pmatrix} \begin{pmatrix} \mathbf{a}_1 \\ \mathbf{a}_2 \end{pmatrix} = \boldsymbol{G} \begin{pmatrix} \mathbf{a}_1 \\ \mathbf{a}_2 \end{pmatrix} \tag{2.7}$$

If the angle between $\mathbf{b}_1$ and $\mathbf{a}_1$ is the same as that between $\mathbf{a}_2$ and $\mathbf{a}_2$, the reconstruction can be denoted using Woods notation , introduced by E. A. Wood in 1964 [48]. Some structures described using this notation can be seen in Figure 2.5. The two-dimensional truncated surface lattice vectors are here given as $\mathbf{a}_1$ and $\mathbf{a}_2$. Possible adsorbate layers are denoted $\mathbf{b}_1$ and $\mathbf{b}_2$ and the relation is stated as

$$N \left(\frac{|\mathbf{b}_1|}{|\mathbf{a}_1|} \times \frac{|\mathbf{b}_2|}{|\mathbf{a}_2|} \right) R\Theta. \tag{2.8}$$

Here N is either p or c for primitive or centred cells respectively and Θ is the angle by which the $\mathbf{b}_i$ vectors have to be rotated with respect to the surface lattice vectors $\mathbf{a}_i$. Unreconstructed surfaces with one adsorbate species per site are denoted to have a (1×1) ordering

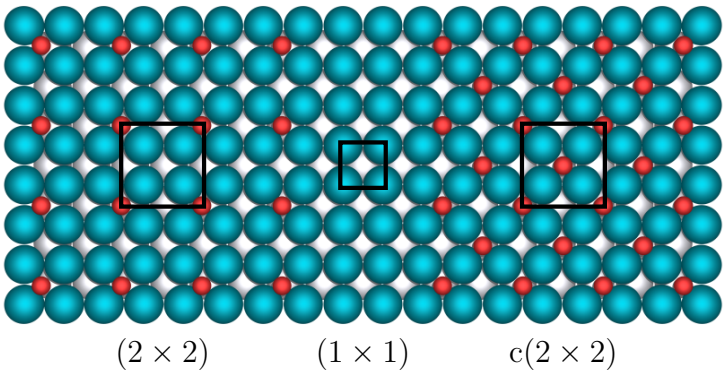

Figure 2.5.: Examples of structures described by the Woods terminology on a Pd fcc(100) surface. Red balls indicates adsorbed oxygen atoms.

2.1.6. Oxidation

Metal surfaces can be oxidized in UHV by exposing them to oxygen. Oxygen can be adsorbed on the surface and if the conditions are right, a ordered layer of bulk metal oxide is formed. Oxide films that are less than about 1 µm in thickness can be described using the theory established by Cabrera and Mott [49] which describes oxidation in atomistic terms. The first assumption is that electrons are free to pass from the metal to ionize the adsorbed O at the surface/gas interface so that the electrochemical potential is equal in the metal and the adsorbed layer. A uniform field is created by a positive surface charge on the metal and a negative contribution from the O ions. The field created by the transport of electrons causes ions to be transported across the film in the opposite directions of the electrons, illustrated in Figure 2.6. Oxidation will continue as long as both metal and oxygen ions are able to overcome the activation energy barrier for diffusion through the film. The activation energy barrier will increase with increasing thickness of the oxide film and when the energy barrier is too large, the oxidation process stops [50].

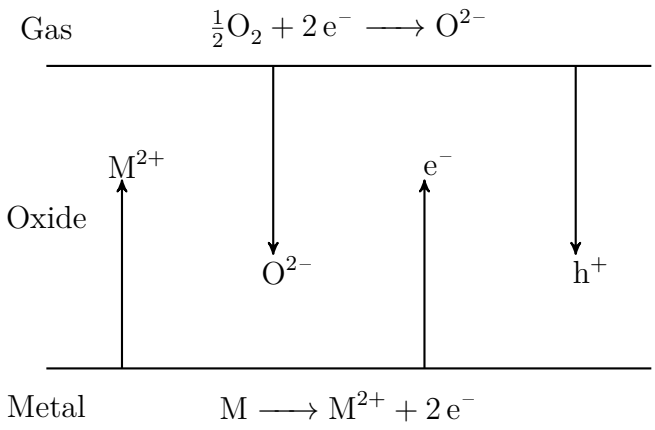

Figure 2.6.: Transport of ions and electrons across a growing oxide film.

Quantum mechanics

Atoms are commonly described as point like nucleus and electrons in stationary circular orbits according to the Bohr model. This is a semi-classical description of the atom and its electrons, but despite its simplicity, the model describes many aspects of atoms correctly and these need to be reinterpreted when a complete quantum mechanical treatment is imposed on a system. It is the anti-symmetry of the electron wave function that gives rise to the various electronic states and orbitals.

The semi-classical theory by Bohr has some flaws where quantum mechanics are needed to get a more correct interpretation of the system. One is that it does not obey the particle-wave duality that all matter possesses. Instead of treating the electrons as charged point particles moving around the nucleus they should be viewed as propagating wave packets, described by wave functions.

The complete quantum state of a system is descried by its wavefunction, ψ, which is found by solving the Schrödinger equation. For simple systems such as the Hydrogen atom, the equation can be solved analytically, but for more complex many-body systems one has to take into account electron-electron Coulomb repulsion, particle indistinguishability as the electrons exchange, the coupling between multiple spins (S) and orbital angular momenta (L). For many-body systems, the Schrödinger equation becomes impossible to solve exactly and one has to rely on numerical methods. Chapter 3 is dedicated to explaining how we can approximate solutions to many-body systems by using Density Functional Theory (DFT).

The characterisation methods in the following section are based on or have to take into account effects emerging from quantum mechanics. Low-energy electron diffraction uses the wave-like nature of electrons to study the periodicity of surfaces, the scanning tunnelling microscope relies on the quantum mechanical tunnelling effect and for X-ray photoemission spectroscopy the uncertainty principle determines the broadening of peaks and the wave-functions of electrons are needed to describe the initial and final states of a photoemission process.

2.2. Characterization techniques

The following section describes the physical principles behind the characterization methods used to study the surface of single crystals in this project. The three techniques are Low-Energy Electron Diffraction (LEED) to study the average order of clean and oxidized surfaces, STM for investigations of the surface on a nanoscale and XPS to determine the average surface composition.

2.2.1. Low-energy electron diffraction

There are two major applications for LEED. The first is to learn something from the pure inspection of the surface diffraction pattern. This gives direct information about the surface order and quality. When a surface is reconstructed or covered with an ordered adsorbate layer, the LEED pattern can give some information about the surface structure and periodicities. The second application of LEED is quantitative structure

determination. This is more difficult as one has to measure the diffraction intensities as a function of the electron kinetic energy and compare them to scattering calculation for a model system. This model has to be changed until good agreement with the measured intensities [40].

In the common electron energy range of LEED, 50-400 eV, the electron mean free path is small and just a few atomic layers, giving it extreme surface sensitivity. A typical LEED system is seen in Figure 2.7 and has two major components. An electron gun producing a beam of electrons with the same energy and a detector system that detects only the elastically scattered electrons.

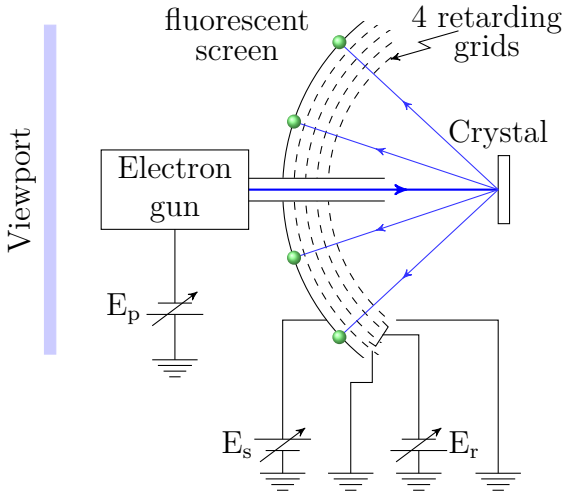

Figure 2.7.: A LEED system.

The detector is composed of four retarding grids at different voltages and a fluorescent screen. The first grid from the sample is grounded to ensure that no electric field around the sample affects the electrons The two next grids (E_r) in the middle are set to the retarding voltage. This voltage is just slightly lower than the electrons' kinetic energy, which will allow elastically electrons to pass, but repels inelastically scattered electrons. The elastically scattered electrons pass the next grid which is set to ground potential and are finally accelerated to fluorescent screen which is set to a hight positive voltage (E_s) [51].

Diffraction of electrons

In order to understand the diffraction pattern formed on the fluorescent screen, an explanation of the incident electron wave and how it interacts with the periodic lattice is required. The electron wave incident on the surface is represented by a wavevector $\mathbf{k}_0$ whose amplitude is given by the de Broglie equation [39]

$$\mathbf{k}_0 = \frac{2\pi}{\lambda} = 2\pi\sqrt{\frac{2\mathrm{meV}}{h^2}} \simeq 2\pi\sqrt{\frac{E_\mathrm{p}}{150}}. \tag{2.9}$$

If V is taken in volts, then $\mathbf{k}_0$ will be in $\mathrm{\AA}^{-1}$. For a two-dimensional case, the lattice can be defined using only two vectors, $\mathbf{a}$, $\mathbf{b}$. To characterize the interaction between the incoming wave and the periodic lattice, it is more convenient to deal with the reciprocal lattice. A reciprocal lattice is the Fourier transform of another lattice, usually a periodic spatial function in real-space (the direct lattice).

For an infinite three dimensional lattice defined by its primitive vectors (e.g. $\mathbf{a}, \mathbf{b}, \mathbf{c}$), its reciprocal lattice can be described using three reciprocal vectors generated by

$$\mathbf{a}^* = \frac{2\pi\mathbf{b}\times\mathbf{c}}{\mathbf{a}(\mathbf{b}\times\mathbf{c})}, \tag{2.10}$$

$$\mathbf{b}^* = \frac{2\pi\mathbf{c}\times\mathbf{a}}{\mathbf{a}(\mathbf{b}\times\mathbf{c})}, \tag{2.11}$$

$$\mathbf{c}^* = \frac{2\pi\mathbf{a}\times\mathbf{b}}{\mathbf{a}(\mathbf{b}\times\mathbf{c})}. \tag{2.12}$$

These vectors now represent the criterion for constructive interference to take place; which is when the change in the electron wave vector must be equal to a reciprocal lattice vector:

$$\mathbf{G} = \mathbf{k}' - \mathbf{k}_0 = h\mathbf{a}^* + k\mathbf{b}^* + l\mathbf{c}^*, \tag{2.13}$$

where the Miller indices, $h, k, l = 0, 1, 2....$ To illustrate the criterion for maximum diffraction an Ewald sphere can be constructed. The Ewald sphere represent the incident plane wave on to the crystal with a wave vector $\mathbf{k}_0$ whose length is $2\pi/\lambda$. The diffracted plane wave has a wave vector $\mathbf{k}'$. Since the surface lattice is two-dimensional, there are only two Laue conditions because the introduction of the surface has destroyed the periodicity of the solid in the direction perpendicular to it. Energy is conserved in elastic scattering, implying that the wave vectors have to have the same length, i.e.

$$\mathbf{k}_0 = \mathbf{k}' \tag{2.14}$$

When drawing the Ewald construction for a two-dimensional surface, the discrete points which are present in the three-dimensional case are replaced by rods perpendicular to the surface. Constructive interference is expected whenever a rod intersects the sphere defined by the wave vectors, illustrated in Figure 2.8.

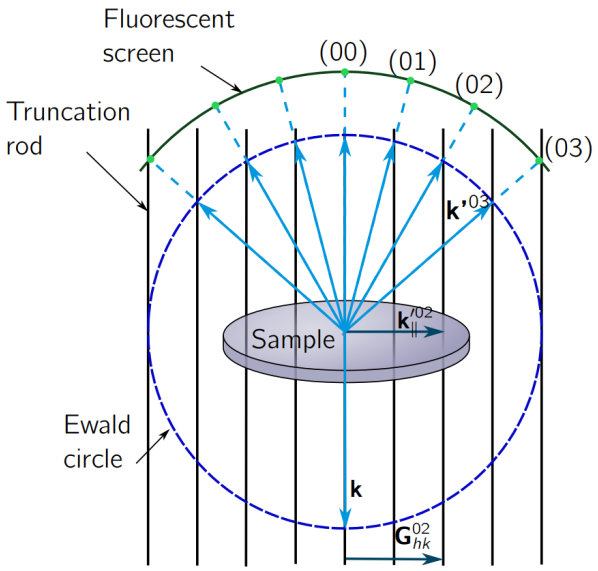

Figure 2.8.: Ewald-construction for surface scattering caused by the incoming wavevector **k** and the scattered wavevector **k'**. Diffraction occurs where the wave vector intersects the vertical rods, representing the reciprocal lattice of the surface. Adapted with permission from [52].

The broken crystal periodicity in the direction normal to the surface of the reciprocal lattice causes the last component to vanish, and the reciprocal lattice vector can be written as

$$\mathbf{G} = h\mathbf{a}^* + k\mathbf{b}^*. \tag{2.15}$$

The LEED pattern on the fluorescent screen can be characterized using Equations (2.7) or (2.8) and used to determine the structure of any superstructures formed by a reconstruction of the substrate surface or by adsorbed species.

2.2.2. Scanning tunnelling microscopy

Another technique extensively used in surface science is STM, which is based on the quantum mechanical tunnelling effect. The technique was invented by G. Binnig and H. Rohrer in 1981 [53] and their work earned them a Nobel prize in physics in 1986 together with E. Ruska [54]. The basic principle of STM is scanning a sharp tip sufficiently close (a few Å) to the surface under investigations such that electrons can tunnel from the occupied states in one metal to unoccupied states in the other by applying a small voltage between them. Piezoelectric crystals are used to move either the sample or tip such that a topographical image of the electron distribution of a small area on the surface can be created. The basic components in a STM are illustrated in Figure 2.9.

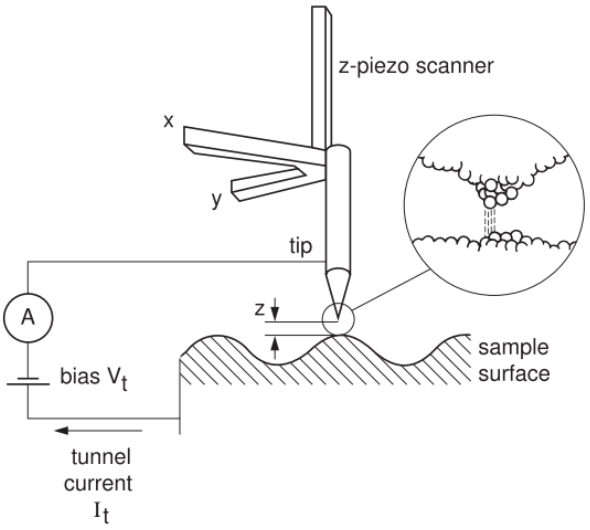

Figure 2.9.: Schematic illustration of an STM setup with a sharp tip, conducting sample and piezo scanner. A feedback control and scanning unit records the tunnelling current between the tip and sample when a voltage V_t is applied. The current recorded is directly related to the electronic density of states at the surface and can be used to create a topographic image of the surface. Adapted from [51].

Physical principles

In classical physics, an electron is not able to pass between two electrodes separated by vacuum because its energy is not sufficient to overcome the barrier. A quantum mechanical particle on the other hand, cannot be trapped completely by a finite potential step, due to its delocalized electron wave function. This allows an electron to tunnel through a potential barrier, which according to classical physics is impossible.

To approximate the tunnelling current the formalism of Tersoff and Hamann (TH) is commonly used [55]. In this approximation the experiments takes place at room temperature, at small voltage ($\sim$ 10 meV for metal-metal tunnelling) and the tip is modelled as a spherical potential well closest to the surface, illustrated in Figure 2.10. Since the tip is modelled as spherical, it can be described by spherical symmetric s-wave functions only. The obtained tunnelling current is expressed as

$$I \propto V R^2 \exp\left(-\sqrt{\frac{8m\phi}{\hbar}}d\right) \rho(\mathbf{r}_0, E_\mathrm{F}) \tag{2.16}$$

with

$$\rho(\mathbf{r}_0, E_\mathrm{F}) \equiv \sum_v 1\psi_v(\mathbf{r}_0)|^2 \delta(E_v - E_\mathrm{F}). \tag{2.17}$$

Where V is the applied voltage, ϕ height of the tunnel barrier and E_v the eigenenergy

of the wavefunction ψ_v belonging to the sample. The local density of states (LDOS) of the surface at the Fermi level at position $\mathbf{r}$ is expressed as $\rho(\mathbf{r}_0, E_\mathrm{F})$. The exponential function tells us that the tunnel current decays exponentially with increasing distance, d.

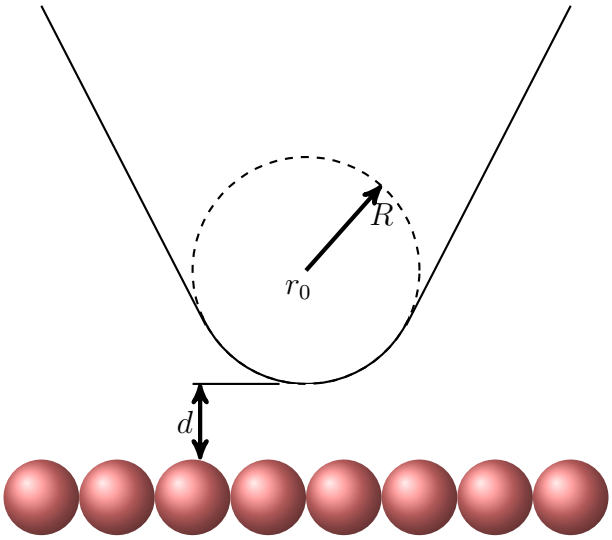

Figure 2.10.: Schematic illustration of tunnelling geometry in the Tersoff-Hamann model. The tip is assumed to have local spherical symmetry with radius of curvature R and center at distance r_0. Nearest distance to the surface, denoted d.

By scanning the tip sufficiently close across the surface, the tunnelling current gives information about the LDOS of the sample. This is used to obtain topographical images of the surface. There are two main modes in scanning the surface, constant current imaging (CCI) and constant height imaging(CHI). In constant current imaging, the tunnelling current is kept constant while the height of the tip is altered through a feedback circuit where the actual tunnelling current is compared to the preset constant current, typically 0.5-5 nA. Recording the feedback signal or lateral height, a map of the surface topography can be obtained. In constant height imaging, the tip is fixed at a certain distance and the topographic image is created from the difference in measured tunnelling current. Constant height imaging requires a very flat surface while scanning to not damage the tip. Since the tunnelling current is strongly dependent on the distance between the sample and tip, STM has resolution down to a few picometers in the z-direction. In x and y directions the resolution depends on the shape of the tip which ideally is terminated by a single atom. In practice the actual current is due to a number of atoms on the tip, but as long as they are sufficiently localized there can be good tunnelling conditions [56, p. 575].

2.2.3. X-ray photoelectron spectroscopy

A commonly used surface analysis technique is XPS. It is based on the photoelectric effect, where an incident photon ejects an electron from the solid and can provide both qualitative and quantitative information. In this technique, the photoemission of an electron as a function of kinetic energy is analysed. The photoemission process where an incident photon of energy $h\nu$ causes the emission of an electron having an kinetic energy E_{kin} can be stated as [57]:

$$E_{\text{kin}} = h\nu - E_{\text{bin}} - \Phi_{\text{A}}, \tag{2.18}$$

where E_{bin} is the binding energy of the electronic level excited by absorption of the photon and Φ_A is the work function of the electron analyzer. A concentric hemispherical analyzer is commonly used to count the number of photoelectrons. To differentiate between the different kinetic energies of the electrons emitted from the sample a voltage is applied between the two hemispheres, as seen in Figure 2.11 for the electron chromotomator. This voltage gives rise to an electric field which will bend the electrons, thus passing on the electrons with the right kinetic energy and causing others to crash in the outer if the kinetic energy is too large or crash in the inner if the kinetic energy is too low. The effect of the applied electric field can be varied, and is the so-called pass energy.

Electrons that are emitted from X-ray excitation below the uppermost surface region cannot penetrate far enough to escape from the sample and reach the detector. The electron escape depth as a function of the electron kinetic energy is illustrated in 2.12 for some metals.

Only the emitted photoelectrons that have not lost energy are contributing to the photoemission peak. Electrons that have lost energy, but still escapes from the surface will contribute to the background signal. To determine bulk values by XPS, the surface has to be atomically clean since its a surface sensitive technique.

The photoemission process

An instructive approach to describe the photoemission process is the *three-step model* [60]:

1. Optical excitation of an electron from an initial state i of wave function ψ_i into a final electron state f of wave function ψ_f within the crystal.

2. Propagation of the excited electron to the surface.

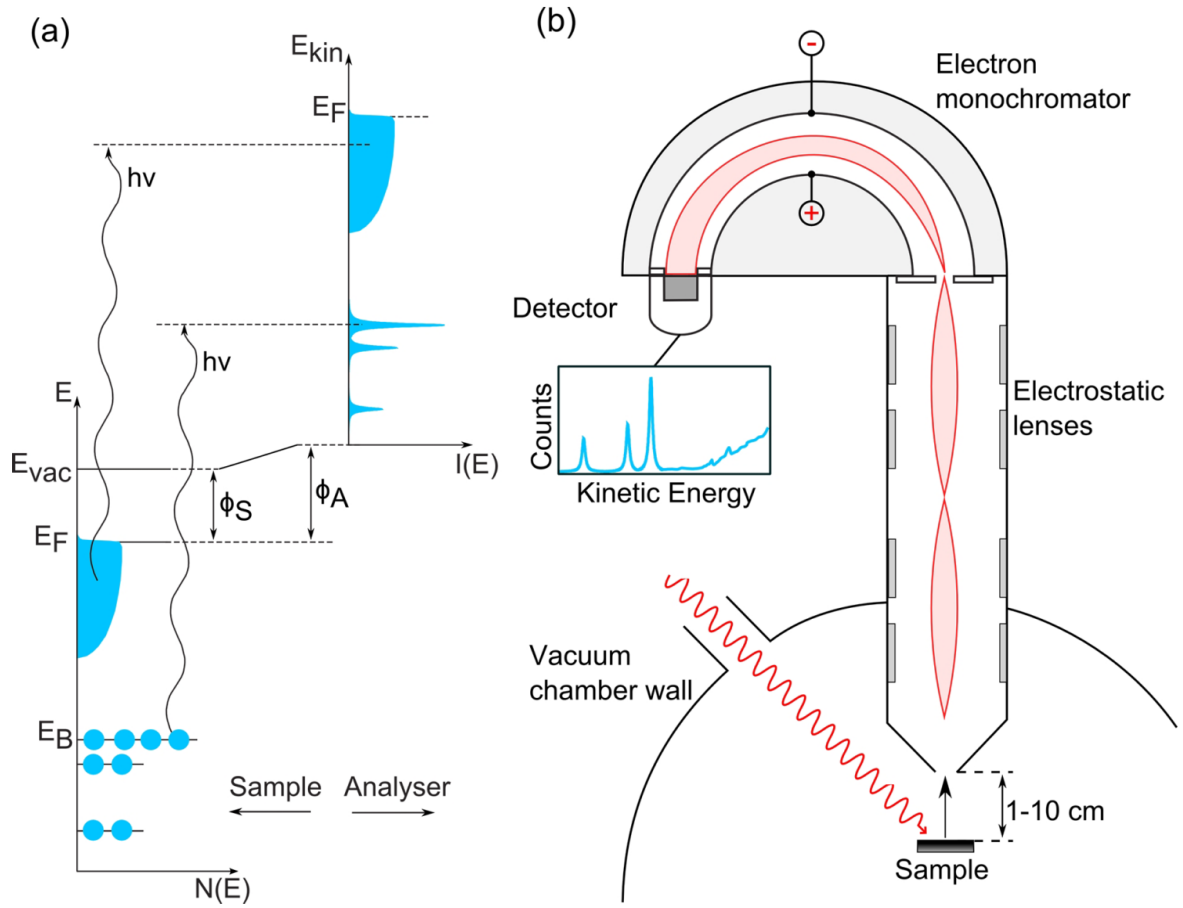

Figure 2.11.: (a) The photoemission process where electrons with binding energy E_{bin} can be excited above the vacuum level E_{vac} by incident photons having energy $h\mu > E_{\text{bin}} + \Phi_{\text{A}}$ greater than combined binding energy and work function of the sample. The result is a intensity spectrum, which is related to the DOS. (b) The main compartments of an XPS analysis chamber. Electrostatic lenses are used to focus the emitted electrons into the hemispherical analyzer. Adapted from [58].

3. Emission of the electron from the solid into the vacuum. The electron traverses the surface.

Core levels

The energy reference points in XPS are the vacuum level E_{vac} for free atoms and molecules and the Fermi level E_F for solids. XPS measures the energy difference between the total energy of the final ionized state of the ion, having $N-1$ electrons and energy E_f^{N-1} and the initial state with N electrons and E_i^N. The exact binding energy of an

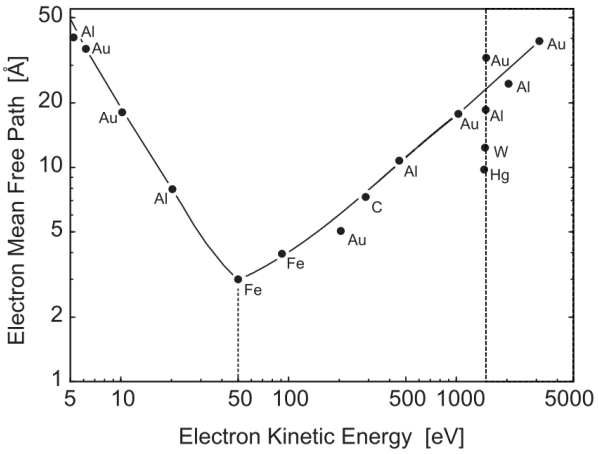

Figure 2.12.: Electron escape depth as a function of their kinetic energy for some metals. The stapled line along the scatter data points are values obtained at $E_{\text{kin}} = 1480$ eV. Adapted with permission from [59].

electron measured by XPS can be stated as

$$E_B = E_f^{N-1} - E_i^N. \tag{2.19}$$

These total energies are not trivial to calculate and one has to rely on approximations to obtain them. Koopman's approximation is the best known, stated as $E_B, k \simeq -\epsilon_k$, which means that the binding energy equals the negative energy of orbital k where the electron was excited. The approximation neglects relaxation energies, i.e. it does not produce any change in the other orbitals. To correct for this, there are two contributions which has to be taken into account to adjust the energy of the orbital which has an electron less. One is from intra-atomic relaxation, relaxation of the orbitals on the same atom, the other from extra-atomic relaxation, in which charges flow from the crystal onto the ion with an additional hole.

With increasing positive charge on an ion in a molecule the binding energy also increases, while the binding energy decreases with increasing negative charge. This is a consequence of the electron screening around the nuclei, and this binding energy shift is denoted ΔE_{CS}.

Core level binding energy in ionic solids, has to account for two special cases. The first is called the polarisation term and describes final state effects where the created hole can polarize its environment and lower its energy. The second term is called the repulsion term and accounts for ions repelling its nearest neighbours in the initial state, which also lowers the energy. These effects are accounted for in the Madelung potential ΔE_M [57].

Final state effects, such as how the electrons react to the ionization of the target body are accounted for by the relaxation effects term, ΔE_R [61, 62]. Together with the Koopman's approximation for the binding energy, E_B mentioned earlier, these effects can be summed to obtain the total measured binding energy:

$$E_B^{\text{exp}} = E_B + \Delta E_{CS} + \Delta E_M + \Delta E_R. \tag{2.20}$$

Photoemission from core-levels always produces a final state with spin and angular momentum. The coupling between core-hole orbital and angular momentum leads to a number of different final states. Spin in a certain state, such as s^2 which have a net spin of $s = 1/2$ for the hole, can couple parallel or antiparallel to the spin of the valence-shell configuration, which leads to an exchange splitting. This coupling is termed core polarization and will lead to core level splitting in the observed spectra. Since spin-orbit coupling is most important for heavier elements, splitting is often observed for the transition metals. The two main peaks used for analysis in this thesis are Au 4f and Pd 3d. Pd 3d is spin split into Pd $3d_{3/2}$ and $3d_{5/2}$ and magnitude of the spin-orbit split is 5.26 eV for pure Pd while pure Au 4f is split into $4f_{5/2}$ and $4f_{7/2}$ with a separation of 3.7 eV [63].

In many-electron systems, electrons interact with each other via the Coloumb and exchange interaction. By removing an electron via the photoemission process, excitations in the remaining systems will occur and will lead to signals in the spectrum with a higher binding energy (smaller kinetic energy). These smaller peaks are termed *satelittes* and represents the excited states.

Chemical shifts

Atoms residing on the surface have a different environment than atoms in the bulk. Laboratory XPS probes up to several nanometers and the topmost surface will only contribute with a small fraction. By cutting through a crystal, the atoms on the surface will have dangling bonds, which will bind atoms and molecules available in the vacuum. This can be used to distinguish between the surface and the bulk contributions as the surface atoms will have a *surface core level shift* (SCLS), a core level shift different than the core level shift for the bulk atoms. SCLS are small so detection requires high resolution and short electron escape depth in order to have a large surface contribution. The use of different photon energies changes the kinetic energy and thus the electron mean free path and the electron escape depth. To meet these requirements, synchrotron radiation can be used. A method of increasing the surface to bulk signal ratio is by tilting

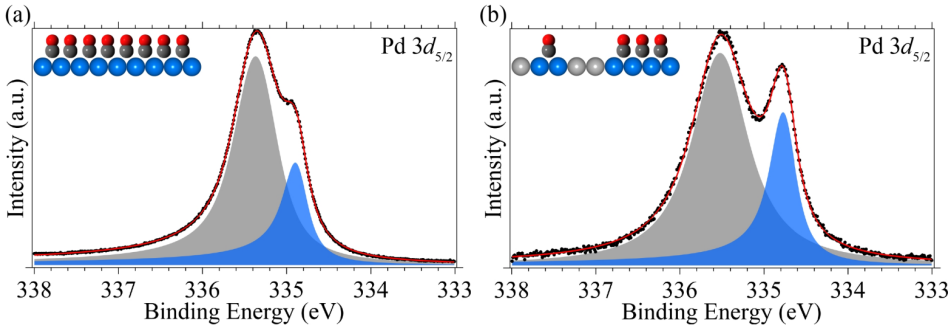

Figure 2.13.: Core level shifts for Pd $3d_{5/2}$ on (a) Pd(100) and (b) $Pd_{75}Ag_{25}$(100) due to adsorbed CO. Adapted from [58].

the sample with respect to the detector. This causes the electrons from the bulk to have a longer path, which in turn lowers the signal from the bulk contribution measured by the detector.

CO can be used to probe the local overlayer structure since the adsorbate may change the binding energy (BE) of the surface atoms. For CO on Pd, the adsorption shifts the Pd 3d surface emission to higher binding energies with the magnitude of the shift depending almost linearly on the number of Pd-CO bonds. The measured shift per bond formed is close to 0.5 eV. [64]

An example of Pd $3d_{5/2}$ core level shift due to adsorbed CO on Pd and $Pd_{75}Ag_{25}$ (100) surfaces is seen in Figure 2.13. For Pd(100) the CLS is +0.5 eV towards higher binding energy and +0.7 eV for $Pd_{75}Ag_{25}$(100) [2].

Core level analysis

To extract information available in the photoemission (PE) spectra, the peaks will have to be decomposed into several contributions based on their chemical environment. The spectra of core levels should to a first approximation be one narrow line. In actual PE spectra a broadening of individual peaks is seen and the contributions can be divided into three different types, Gaussian, Lorentzian and asymmetric.

Gaussian broadening is caused by phonon interaction, small chemical shifts, disorder, the limited resolution of the electron analyzer and can be described by

$$I_{\mathrm{G}} = I_0 \exp\left[-\ln 2 \frac{(E-E_0)^2}{4\sigma^2}\right], \tag{2.21}$$

where I_0 is the measured intensity without any overlayer on the surface and σ is the Gaussian full width half maximum (FWHM) [65].

The photoemission process from the core level of an atom produces a Lorentzian line.

The linewidth is determined by the finite life-time, t of the excited state and has an uncertainty in the energy, ΔE according to Heisenberg's uncertainty principle [66]:

$$\Delta E = \frac{\hbar}{t}, \tag{2.22}$$

with the life-time, t, the intensity decays exponentially over time from the initial state, I_0:

$$I(t) = I_0 \exp -2\gamma t. \tag{2.23}$$

The Fourier transform of Equation (2.23) with respect to energy results in a Lorentzian contribution to the line shape as

$$I_{\mathrm{L}} = I_0 \frac{\gamma^2}{(E - E_0)^2 - \gamma^2}, \tag{2.24}$$

where 2γ is the Lorentzian FWHM. Excitation of additional electrons during the photoemission process can lead lead to a partial energy loss for the photoelectron. The additional excited electrons is coupled to the created hole through electron-hole pairs in the conduction band, which affects the line shape. For metals, the smallest possible energy for such an excitation is zero and will lead to the peak developing a tail towards higher binding energies. This loss of energy results in an asymmetric line shape where α denotes asymmetry and can be expressed as

$$I_\alpha(E) \propto \frac{1}{(E - E_0)}^{(1-\alpha)/2}. \tag{2.25}$$

Which goes to infinity for $E = E_0$ and has to be combined with the lifetime for the electron hole. The resulting lineshape is called a Donjiac-Sunjik line [67], and can be expressed as

$$I_{\mathrm{DS}} = I_0 \frac{\Gamma(1-\alpha)\cos\left[\frac{\pi\alpha}{2} + (1-\alpha)\arctan\left(\frac{E-E_0}{\gamma}\right)\right]}{[(E-E_0)^2 + \gamma^2]^{(1-\alpha)/2}}. \tag{2.26}$$

Here Γ is the Γ-function and 2γ the lifetime. For symmetric line shapes, $\alpha = 0$ and the equation is reduced to Equation (2.24).

Donjiak-Sunjik line profiles are used to fit peaks with asymmetry. For Pd 3d core levels, the line profile fails to properly describe the line shape in the spectrum. This is caused by a rapid change of density of states around the Fermi level. On the higher energy side of the peak the asymmetry parameter does not properly describe the shape and leads to a small "hump" in the spectrum. By introducing adsorbates, this feature

disappears due to the induced core level shift. To properly describe a Pd 3d lineshape, an additional component can be added which does not represent any induced core level shift, but accounts for the excitations caused by the photoelectron during transport to the surface. [68]

Inelastically scattered electrons contributes to the spectrum and has to be removed by a suitable procedure in order to extract the primary spectrum, i.e. the main peaks. The background spectrum is modeled using different methods where the most common are a linear function, Shirley background [69] and Tougaard background [70].

Chapter 3.

Computational theory

Ab initio calculations based on Density Functional Theory (DFT) utilises quantum mechanical laws and principles and not empirical data to model the properties of materials. Being a ground-state theory, all calculations are performed at 0 K. Given that DFT calculations describe reality semi-quantitatively, they have been widely adopted as a basis for the analysis of catalytic processes at surfaces. This chapter introduces the fundamentals and gives a brief introduction to DFT and its application through the Vienna *Ab initio* Simulation Package (VASP). For a more thorough introduction to DFT, the reader is referred to the book "Density Functional Theory - A Practical Introduction" [71].

3.1. Schrödinger equation

The total energy of a system can be described by the Hamiltonian ($\hat{H}$) operator. It is described by the sum of kinetic ($\hat{T}$) and potential ($\hat{V}$) energy of the system:

$$\hat{H} = \hat{T} + \hat{V}. \tag{3.1}$$

The potential energy can be further divided and for a molecule consisting of M nuclei (n) and N electrons (e), the Hamiltonian takes the shape

$$\hat{H} = \hat{T}_{\mathrm{e}} + \hat{T}_{\mathrm{n}} + \hat{V}_{\mathrm{e\text{-}n}} + \hat{V}_{\mathrm{e\text{-}e}} + \hat{V}_{\mathrm{n\text{-}n}}. \tag{3.2}$$

These terms are:

$\hat{T}_{\mathrm{e}} = -\frac{1}{2}\sum_{i}^{N}\Delta_i^2$ Kinetic energy operator for each electron

$\hat{T}_{\mathrm{n}} = -\frac{1}{2}\sum_{I}^{M}\frac{1}{M_I}\Delta_I^2$ Kinetic energy operator for each nuclei

$$\hat{V}_{\text{e-n}} = -\sum_{i}^{N}\sum_{I}^{M}\frac{Z}{|\boldsymbol{r}_i - \boldsymbol{R}_I|} \quad \text{Potential acting on the electrons due to the nuclei}$$

$$\hat{V}_{\text{e-e}} = \frac{1}{2}\sum_{i}^{N}\sum_{i\neq j}^{N}\frac{1}{|\boldsymbol{r}_i - \boldsymbol{r}_j|} \quad \text{Coloumbic electron-electron repulsions}$$

$$\hat{V}_{\text{n-n}} = \frac{1}{2}\sum_{I}^{M}\sum_{J\neq I}^{M}\frac{Z_I Z_J}{|\boldsymbol{R}_I - \boldsymbol{R}_J|} \quad \text{Coloumbic nuclei-nuclei repulsions}$$

Inserting the terms above into Equation (3.2) creates the complete Hamiltonian for a system of atoms:

$$\hat{H} = -\frac{1}{2}\sum_{i}^{N}\Delta_i^2 - \frac{1}{2}\sum_{I}^{M}\frac{1}{M_I}\Delta_I^2 - \sum_{i}^{N}\sum_{I}^{M}\frac{Z}{|\boldsymbol{r}_i - \boldsymbol{R}_I|} + \frac{1}{2}\sum_{i}^{N}\sum_{i\neq j}^{N}\frac{1}{|\boldsymbol{r}_i - \boldsymbol{r}_j|} + \frac{1}{2}\sum_{I}^{M}\sum_{J\neq I}^{M}\frac{Z_I Z_J}{|\boldsymbol{R}_I - \boldsymbol{R}_J|} \tag{3.3}$$

Having written out the Hamiltonian, the total energy of the system can be evaluated by solution of the Schrödinger equation (SE). For a stationary electronic state, not taking into account relativistic quantum effects, the system is described by the wave function $\psi(\boldsymbol{r_1}, \ldots, \boldsymbol{r}_N)$; the many-electron time-independent Schrödinger equation (TISE):

$$\hat{H}\psi = E\psi \tag{3.4}$$

3.2. The Born-Oppenheimer approximation

In a crystalline solid the interactions between nuclei and electrons, nuclei and all other nuclei and each electron and all other electrons must be considered, yielding a Schrödinger equation which is impossible to solve exact. The many-electron TISE is simplified using the Born-Oppenheimer approximation where the motion of the electrons is assumed independent of the motion of the nuclei. Since the mass of nuclei is much larger than for an electron they can be viewed as stationary [72]. Doing this, the degrees of freedom in the Hamiltonian is reduced and Equation (3.4) can be written as

$$\left[\underbrace{-\frac{\hbar^2}{2m}\sum_{i=1}^{N}\Delta_i^2}_{\substack{\text{Kinetic energy}\\ \text{of each electron}}} + \underbrace{\sum_{i=1}^{N}V(\boldsymbol{r}_i)}_{\substack{\text{Interaction energy between each electron and}\\ \text{the collection of (fixed) nuclei}}} + \underbrace{\sum_{i=1}^{N}\sum_{j<i}U(\boldsymbol{r}_i, \boldsymbol{r}_j)}_{\substack{\text{Interaction energy}\\ \text{between different electrons}}}\right]\psi = E\psi \tag{3.5}$$

where ψ is the total electron wave-function and E is the ground state energy. The equation contains all the information about the system and is exactly solvable for some simple cases, such as a square 2D potential or the hydrogen atom.

Going from one to two particles, the result is a SE of one two-particle function. The former 3 dimensional equation becomes 6 dimensional and the complexity of the equation describing the system increases rapidly with the number of particles in the system. This causes the SE to become impossible to solve exactly for more complex systems.

3.3. Hohenberg-Kohn theorems

Solving the SE for large systems is currently not feasible. That's why DFT is applied, which is based on an approximate solution to the SE of a many-body system. DFT is based on two fundamental theorems devised by Hohenberg and Kohn [73]:

1. In an external potential, V_{ext}, the total energy of a system is a functional of the electron density. A functional is a function of a function (e.g. $(E[n])$ of a function $(n(\boldsymbol{r}))$)
$$E = E[n(\boldsymbol{r})] = \int \mathrm{d}\boldsymbol{r} V_{\text{ext}} n(\boldsymbol{r}) + F[n(\boldsymbol{r})]. \tag{3.6}$$
The electron density fully determines the Hamiltonian of the many-body system. In other words, the ground state energy E, in Equation (3.5) is related to the electron density $n(\boldsymbol{r})$.

2. The electron density that minimizes the energy of the overall functional is the true density corresponding to the full solution of the SE. The electron density is related to the individual electron wavefunction, ψ_i, with
$$n(\boldsymbol{r}) = 2\sum_{i=1} \psi_i^*(\boldsymbol{r})\psi_i(\boldsymbol{r}), \tag{3.7}$$
which reduces the N dimensional problem to three dimenstions. However, the true form of the energy functional is not revealed from the first or the second theorem and consequently it has to be approximated.

3.4. The Kohn-Sham equation

Rewriting Equation (3.5) for the individual electron wavefunction gives

$$\left[\underbrace{-\frac{\hbar^2}{2m}\Delta^2}_{\substack{\text{Kinetic energy} \\ \text{of the electron}}} + \underbrace{V(\boldsymbol{r})}_{\substack{\text{Interaction energy} \\ \text{of the electron and} \\ \text{the collection of} \\ \text{(fixed) nuclei}}} + \underbrace{V_{\mathrm{H}}(\boldsymbol{r})}_{\substack{\text{Hartree} \\ \text{potential}}} + \underbrace{V_{\mathrm{XC}}(\boldsymbol{r})}_{\substack{\text{Exchange-correlation} \\ \text{potential}}} \right] \psi_i(\boldsymbol{r}) = E_i \psi(\boldsymbol{r}_i), \tag{3.8}$$

where both the exchange correlation and the Hartree potential contains the unknown electron-electron interaction. The Hartree potential, V_{H} describes the repulsion between the electron and the electron density and can be calculated using

$$V_{\mathrm{H}}(\boldsymbol{r}) = e^2 \int \frac{n(\boldsymbol{r'})}{|\boldsymbol{r} - \boldsymbol{r'}|} \, \mathrm{d}^3 r'. \tag{3.9}$$

This potential includes an electron self-interaction which is corrected for by the exchange correlation potential, V_{XC}. The exchange interaction is due to the Pauli principle, which states that two electrons with the same spin must not occupy the same state. This gives rise to an effective repulsion between electrons of the same spin state. The correlation interaction stems from electrons repelling each other due to the Coulomb interaction. To minimize the effect of the unknown $V_{\mathrm{XC}}^{\mathrm{true}}$ an assumption is made in which the ground state density of the original interacting system is equal to that of some chosen non-interacting system that is exactly soluble. All the difficult terms is then included in some approximate functional of the density.

Exchange-correlation approximations

The components in Equation (3.8) might at first glance looks similar in composition and complexity, but they are all rather easily solved except for the exchange correlation term. The local density approximation (LDA) takes advantage of the fact that the exchange-correlation potential is precisely known for the uniform electron gas, where the electron density is independent of the position, $\boldsymbol{r}$. This gives the known potential for constant electron density:

$$V_{\mathrm{XC}} = V_{\mathrm{XC}}^{\text{electron gas}}[n(\boldsymbol{r})]. \tag{3.10}$$

The LDA is easily applied to many systems, but it is not the most accurate approximation. Another, more precise approximation is the general gradient approximation (GGA) which takes the gradient of the electron density into account.

$$V_{\mathrm{XC}} = V_{\mathrm{XC}}^{\text{electron gas}}[n(\boldsymbol{r})]F_{\mathrm{XC}}[n, \Delta n]. \tag{3.11}$$

There are more sophisticated and accurate functionals available, but they are also (much) more computationally costly and are not explained here. In this project the GGA by Perdew, Burke and Ernzerhof (PBE) [74, 75] functional is utilized.

Chapter 4.

Computational methods

The result from a DFT calculation is the total energy of the system and the Kohn-Sham orbitals which describe the density. These are fundamental properties which gives the desired insight into the system when analyzed.

4.1. Surface energy

The (100) surface was modelled with a (2×2) surface cell with six atomic layers. The slabs were separated by 16 Å of vacuum in the direction normal to the surface. The configurations of interest are the extremes, i.e. pure Pd and pure Au terminated surfaces, some possible configurations in between and the bulk terminated surface. These alloyed surfaces are formed from redistributing atoms in the top four layers and the total slab is stoichometric for all configurations investigated. To mimic the continuation of the system into the bulk, the bottom two layers are fixated in bulk configuration for all calculations.

To find the surface energy of the pure Pd and Au slabs and the bulk terminated surface, the following equation was used:

$$\gamma_{\mathrm{u}} = \frac{E_{\mathrm{slab}} - N \cdot E_{\mathrm{bulk}}}{2A} \tag{4.1}$$

Where E_{slab} is the energy of the slab, N is the total number of atoms (in this case 48), and E_{bulk} is the energy per atom of the bulk. A is the surface area and it is found by multiplying $a \cdot a$ from the converged calculation.

The factor 2 in Equation (4.1) accounts for both sides of the slab. For alloy systems where the configuration on one side is changed and no longer in bulk configuration, this has to be accounted for when calculating the surface energy. During relaxation, the top surface was allowed to relax and the bottom one was kept fixed. This model does

not provide an isolated relaxed surface and both sides of the stoichiometric slabs are considered in the calculation of the energy. Their different surface energies (γ_{r}) and (γ_{u}) are used for the relaxed and unrelaxed sides respectively. The unrelaxed surface energy is found from calculating the bulk terminated slab. These values are useful for calculating the average surface energy of terminations A and B of (100), as the slabs are asymmetric and complementary [76].

$$\gamma_{\mathrm{r}} + \gamma_{\mathrm{u}} = \frac{E_{\mathrm{slab}} - N \cdot E_{\mathrm{bulk}}}{A} \tag{4.2}$$

A lower value of the surface energy found using Equation (4.1) or Equation (4.2) indicates a more stable configuration.

4.2. Adsorption energy

The adsorption energy is a measure of how strongly an adsorbate binds to the surface. The more negative the value (higher), the harder it is to remove the adsorbed atom/-molecule from the surface. If the adsorption energy is negative, the binding between the adsorbate and the surface is favourable. The energy of adsorption was calculated with respect to a free carbon atom in gas phase.

Two different types of adsorption energies are calculated; one is the total adsorption energy,

$$E_{\mathrm{ads}}^{\mathrm{tot}} = E_{[\mathrm{slab\ +\ nC}]} - E_{\mathrm{slab}} - n \cdot E_{\mathrm{C}} \tag{4.3}$$

where n is the number of adsorbed atoms. In this case, all the adsorbed atoms share the total energy added to the system equally. Equation (4.3) gives a measure of the stability of the system. If the total energy is below 0, the system is stable and if the value decreases with more added adsorbates, the system is further stabilized when the coverage increase.

Another type of adsorption energy is the differential adsorption energy which tells us how the system reacts to addition of more adsorbates:

$$E_{\mathrm{ads}}^{\mathrm{diff}} = E_{[\mathrm{slab\ +\ nC}]} - E_{[\mathrm{slab+(n\text{-}1)C}]} - E_{\mathrm{C}}. \tag{4.4}$$

If the value of $E_{\mathrm{ads}}^{\mathrm{diff}}$ is positive, the last added atom is not stable on the surface but if its negative, the last added atom is allowed to adsorb.

4.3. Analysis of electronic structure

There are a range of tools which can help in understanding how a surface will react to adsorbates by looking at their electronic structure before and after adsorption.

4.3.1. Density of states

Decomposing the electron density of atoms into different orbitals, one can determine which particular orbitals and from which atoms the contributions to adsorbate interaction arises. Projections onto the orbitals (s, p and d) are found for selections of atoms using the pymatgen package in Python. Once these projections are determined, several interesting properties can be investigated. The total number of states in the band is found by integrating across all possible energies:

$$N_{\text{states}} = \int_{-\infty}^{\infty} \rho \mathrm{d}E, \tag{4.5}$$

where ρ is the sum of the projections onto the wanted orbital. The number of occupied states is found by integrating up to the Fermi level, which is set to zero.

$$N_{\text{states}} = \int_{-\infty}^{0} \rho \mathrm{d}E, . \tag{4.6}$$

The average energy of the d band, also called the d band center is denoted ϵ_{d} and calculated using

$$\epsilon_{\mathrm{d}} = \frac{\int \rho \cdot E \mathrm{d}E}{\int \rho \mathrm{d}E}. \tag{4.7}$$

To investigate adsorption phenomena on transition metal surfaces, it is the center and density of states of the *d* orbital which is of most interest. In this work, the integration was done numerically using Simpson's method.

4.3.2. The d band model

Adsorption of a molecule or atom onto a metal surface results in a two-level interaction. The Pauli principle states that the wave functions must be orthogonal to each other. This drives up the energy of the system and has a repulsive effect on the adsorbate. Hybridization of the orbitals forms bonding and antibonding states due to the interaction with the metal surface. The bonding state is lower in energy and will be occupied first. Hybridization will have an attractive effect if only the bonding state becomes occupied, cancelling out the energy loss caused by the orthogonalization. On the other hand, if

both the bonding and antibonding states becomes occupied, no energy is gained due to hybridization which causes the total effect of the interaction to be repulsive [1].

The filling and the center of the d band determines how large this attraction is. Figure 4.1 illustrates this: When the band is low and broad only a single state can be been at the bottom of the band. As the band shifts upwards closer to the Fermi level, an antibonding state appears above the band. These antibonding states above the Fermi level are empty and the bond becomes stronger as the number of empty antibonding states increases [77]. The d band centre gives thus a good indication of how favourable adsorption will be and how reactive the surface is.

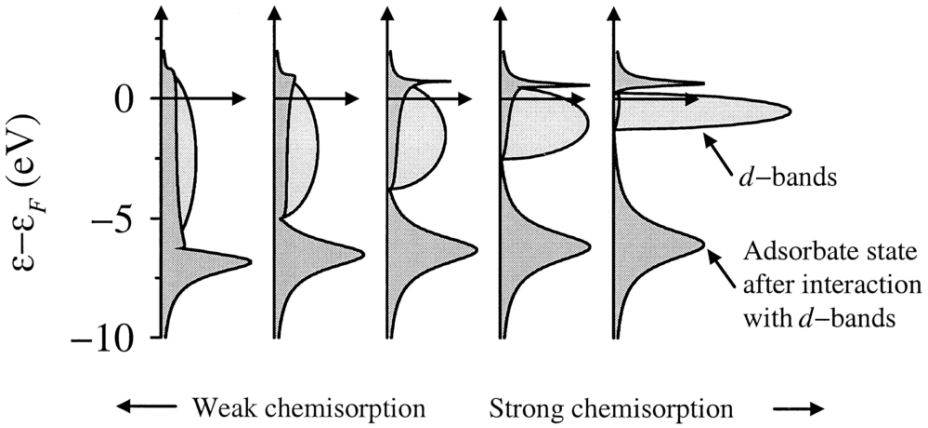

Figure 4.1.: The local density of states projected onto an adsorbate interacting the d bands of atoms on the surface. The transition between "weak" and "strong" chemisorption occurs when the antibonding states are shifted above the Fermi level and becomes more empty. Adapted with permission from [77]

The origin of the main peaks in the density of states is seen in Figure 4.2. Formation of the bond between an adsorbate and a surface atom can be viewed as two distinct steps. First, the valence 2p electrons of the adsorbate, in this case an O atom, interacts with the metal s electrons. This gives rise to a single resonance and since all 2p resonances are well below the Fermi level they are completely filled. The d bands are narrow which gives rise to strong interaction as it splits the oxygen resonance into two states, one state which is binding with respect to the adsorbate and the d states of the metal and another above the d bands which is antibonding [78].

4.3.3. Bader analysis

To determine the charge transfer between surface atoms and adsorbates, the Bader charge analysis [79] is performed. It involves decomposition of electronic charge density

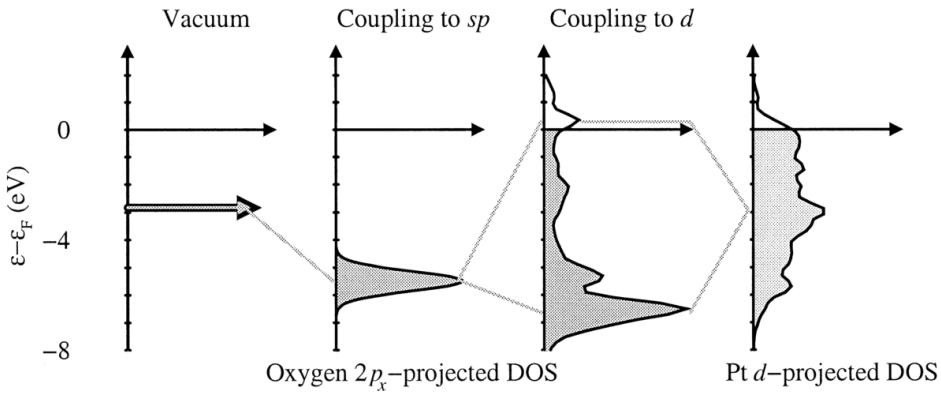

Figure 4.2.: Formation of a chemical bond between an oxygen atom's valence electrons and the s and d states of a Pt surface atom. Adapted with permission from [77]

into atomic contributions. The space is divided into atomic regions where the dividing surfaces are the minimum of the charge density, i.e. the gradient of the charge density is zero along the surface normal. These charge minima typically occur between two atoms, which means the charge enclosed within the Bader volume is a good approximation for the charge of the atom. This analysis can show if there is charge transfer between atoms, with its unit reported in electrons (e). To calculate the charges on selected atoms, the software from Henkelman's group was used [80]. To illustrate how the electron density is concentrated around individual atoms and affected by an adsorbate, isosurfaces can be produced. These are made by subtracting the electron density volume with the electron density volume calculated before adsorption. To subtract electron density volumes and visualize the isosurfaces, the VESTA software was used [81].

4.4. Computational implementation

Solving the Schrödinger equation using the Hohenberg-Kohn theorems is an iterative process which can be illustrated using a flow diagram

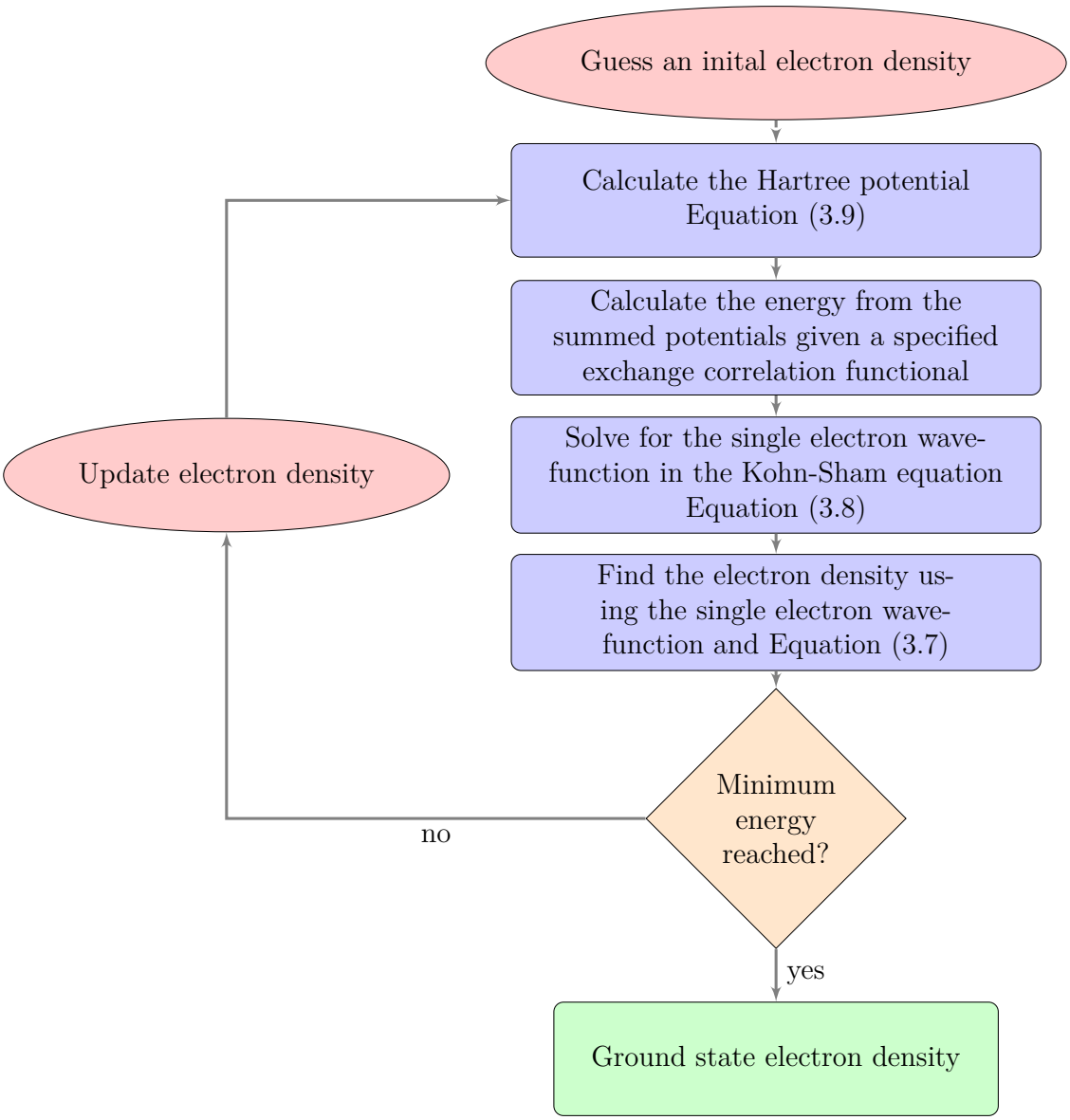

Figure 4.3.: The electronic convergence loop.

The forces between the ions can be calculated once the ground state electron density is found. The Hellmann-Feynman force acting on an ion i, is given by:

$$\boldsymbol{F}_i^{\text{H-F}} = -\frac{\delta E}{\delta \boldsymbol{R}_i}, \tag{4.8}$$

where E is the Kohn-Sham energy (sum of the orbital energies) and $\boldsymbol{R}_i$ is the position of ion i. The Hellmann-Feynman forces are used to move the ions such that the net forces acting on the ions are minimized. For every new configurations of the ions in the lattice, the electronic convergence loop must be performed.

The Kohn-Sham equation for a single electron, Equation (3.8) is in crystalline solids expressed as a plane wave with the periodicity of the crystal lattice:

$$\psi_{\boldsymbol{q}(r)} = \sum_{G} c_{\boldsymbol{q}+\boldsymbol{G}} e^{i(\boldsymbol{q}+\boldsymbol{G})\boldsymbol{r}}, \tag{4.9}$$

where $\boldsymbol{q}$ is the wave vector, $\boldsymbol{G}$ is a reciprocal lattice vector and $\boldsymbol{r}$ is the position of the ion in the unit cell. To find the wavefunction for each $\boldsymbol{q}$, Equation (4.9) will have to be summed over infinitely many reciprocal lattice vectors ($\boldsymbol{G}$). Computationally this would be very costly. In order to limit the summation, the total energy of the wavefunction is considered:

$$E = \frac{\hbar^2}{2m}|\boldsymbol{k} + \boldsymbol{G}|^2. \tag{4.10}$$

The system will always try to minimize its energy and therefore the lower energy states are more important than the higher. To cope with this in DFT, the $\boldsymbol{G}$ vectors are only considered up to a maximum, $\boldsymbol{G}_{\text{cut}}$. This maximum is related to the cut-off energy through

$$E_{\text{cut}} = \frac{\hbar^2}{2m} G_{\text{cut}}^2, \tag{4.11}$$

which is found for each unique system and is determined by the convergence of the system with respect to the cutoff energy. Higher values of the cut-off energy results in better convergence, but is more computationally expensive. Another simplification performed in numerically solving the SE is to discretize the first Brillouin zone to avoid continuous integration over all possible wave vectors within it. The density of the mesh points determines the accuracy of the calculations. Higher k-point density yields more accurate calculations and is important to consider when e.g. calculating the band diagram for a given solid. The minimum density for which the system converges is therefore chosen as the k-point density in the calculations on that system.

To further lower the computational cost of DFT calculations, pseudopotentials are used where the core electrons and nucleus are replaced with a constant potential that matches various physical properties. This means that the calculations can be performed using only the valence electrons. Potentials which takes many valence electrons into consideration are termed hard potentials and requires higher cutoff energies, making the calculation more demanding. Soft potentials on the other hand have fewer valence electrons and require lower cutoff energies, but are less accurate than simulations performed with hard potentials.

4.4.1. VASP - Vienna *Ab initio* Simulation Package

The Vienna *Ab initio* Simulation Package is a computer simulation program that uses DFT for atomic scale materials modelling. For a thorough introduction to the theoretical background of the simulation package, the reader is referred to the articles by Kresse and coworkers [82–84]. In order to run a VASP simulation, four different input files are required. These are INCAR, POSCAR, POTCAR and KPOINTS, with examples given in Appendix E.

INCAR: Defines the input parameters, i.e. what we want VASP to calculate. It also describes how the calculations are performed.

POSCAR: Gives information about the unit cell or super-cell. It gives the number of atoms, type of element, length and direction of the lattice vectors. A larger structure, a supercell, is used in the calculations for the surface to have the desired accuracy.

POTCAR: Defines the pseudopotentials to be used for each different atom in the system.

KPOINTS: Defines the k-point density for the calculations. For a facecentered cubic lattice, the k-mesh is given as $i \times j \times k$, where i, j, k are integers specifying the number of k-points on the mesh in the respective lattice direction.

VASP generates several output files depending on the tags/parameters in the INCAR files, but all calculations have one OUTCAR and one CONTCAR file generated.

OUTCAR: Contains information from the performed calculation including total energies and forces.

CONTCAR: Has the same format as a POSCAR file, but the CONTCAR file is generated after every ionic state.

Packages in Python

To create the required input files and analyze the results, two different Python packages have been used extensively. Atomic Simulation Environment (ASE) [85] has been used

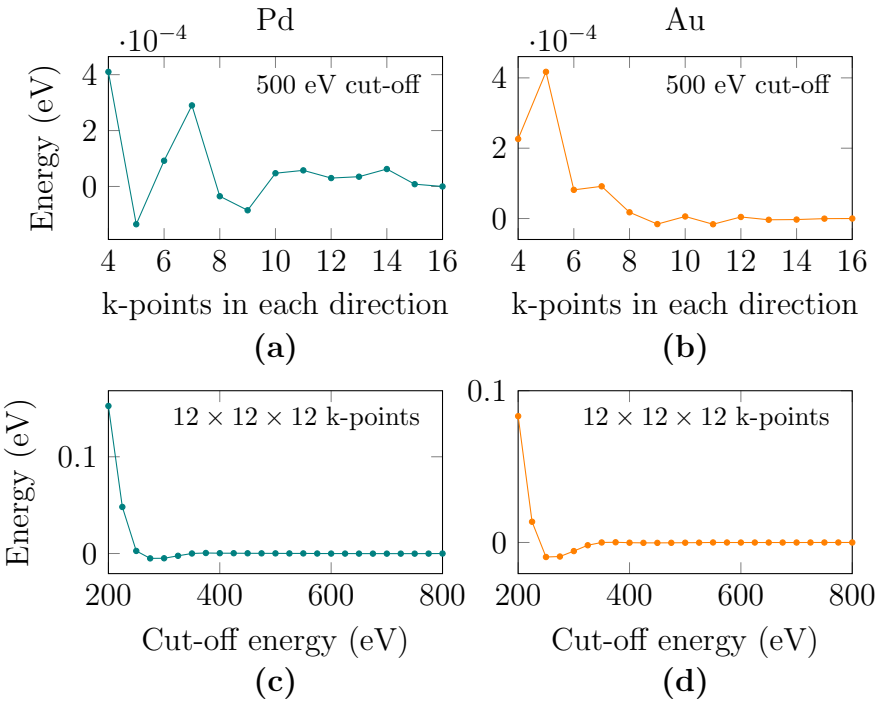

Figure 4.4.: Energy cut-off and k-points convergence tests for bulk Pd and Au.

to create the structures, define input parameters and to call the VASP calculator to perform the desired calculation.

Python Materials Genomics (pymatgen) [86] has been used to read results from calculations, verify the results in terms of convergence and extract information about the density of states.

4.4.2. Choice of computational parameters

The accuracy of the calculations is depending on a range of parameters. To determine these parameters convergence tests are needed. The accuracy of the description of the electron density is depending on the energy cut-off value. To integrate over the Brillouin zone a Monkhorst-Pack grid [87, 88] was used and the k-point mesh defines how rigorously this is done. Both values should be chosen a bit conservatively to allow for changes in structure and composition of the system. These tests are presented for bulk Pd and Au in Figure 4.4 and based on these, a $12 \times 12 \times 12$ k-point mesh and a cut-off energy of 500 eV was chosen for the bulk systems.

The spacing of k-points is dependent on cell size, meaning that larger supercells requires fewer points. Due to this, a $5 \times 5 \times 1$ grid was used for the surface slabs and the cut-off energy was set to 550 eV, 50 eV higher than for the bulk systems due to the

introduction of adsorbates. When investigating alloys, no symmetry is found and the larger number of k-points is necessary to have the desired accuracy. For calculations of the electronic structure a grid consisting of $7 \times 7 \times 1$ kpoints was used to have better sampling in reciprocal space. Calculations with adsorbates on the surface also included correction of dipole moment in the z-direction. As mentioned in the beginning of the chapter, the (100) surface was modelled with a (2×2) surface cell with six atomic layers. The slabs were separated by 16 Å of vacuum in the direction normal to the surface and to mimic the continuation of the system in the bulk, the bottom layers were fixed in position and not allowed to relax.

Chapter 5.

Experimental methods

5.1. Vacuum systems

All experiments involving STM, LEED and XPS were performed inside a UHV chamber. The different compartments of a vacuum chamber are connected by flanges which are sealed by copper gaskets to minimize leakages. To achieve a good vacuum the vacuum chambers has to baked if they have been evacuated or if there is too much H_2O present. Baking is a process where the stainless steel chamber is insulated using a solid insulating frame, covered in aluminium foil or special blankets and heated to above the boiling temperature of water to evaporate as much gas from the inside of the chamber walls. The chamber is kept at an elevated temperature for an extended period of time. After bake-out, the insulating walls, foils or blankets are removed and all the parts which cannot handle the baking temperatures are reconnected to the system. The base pressure is reached when an equilibrium between the amount of particles pumped out equals the amount of particles that desorb from the walls. The base pressures was on the order of 10^{-9} mbar in the STM chamber, 10^{-10} mbar in the analysis chamber of the XPS, and $5 \cdot 10^{-9}$ mbar in the analysis chamber on MATline in Aarhus.

To monitor the pressure an ion gauge is used. A filament emits electrons that are accelerated inside a grid. In the grid, the electrons hit rest gas molecules and ionise them. The ions are collected at the wire in the middle of the grid and the current from that wire is a measure of the pressure.

Connected to vacuum chambers is a quadrupole mass spectrometer, which in this work was used for leak testing. It has three sections, first rest gas is ionized as in the ion gauge. The ions are then accelerated and focused into the second section, the mass filter. It consists of four bars which set up an electrical quadrupole field and let only ions with same ratio of mass to charge pass through. The last element is the ion detector. The different parts and operating principle is illustrated in Figure 5.1.

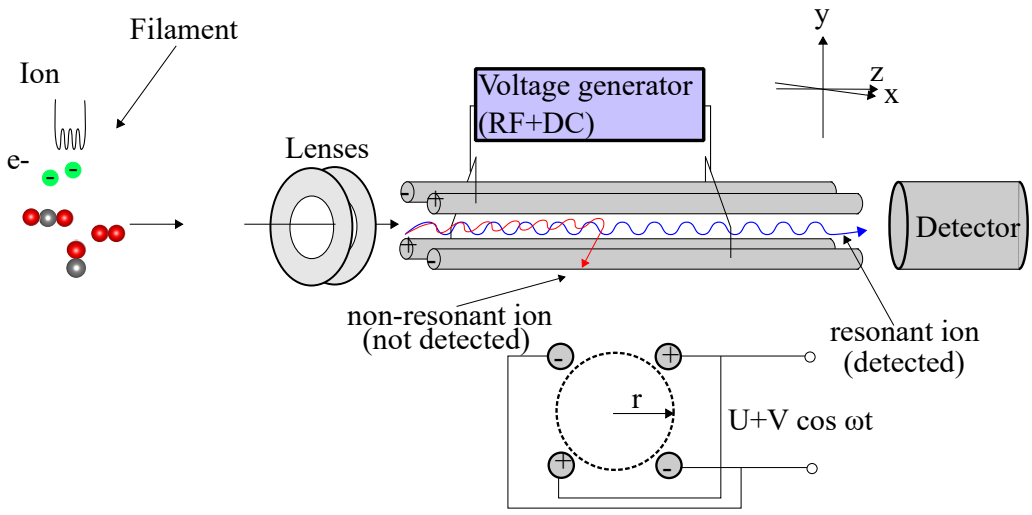

Figure 5.1.: Schematic of a quadropole mass spectrometer. Adapted with permission from [89].

Leak detection is done by spraying He on different parts of the system while monitoring the intensity of mass 4 particles. If there's a detectable leak, there will be a rapid increase of He in the chamber which shows up on the monitor connected to the spectrometer. A significant leak was found on the STM vacuum chamber located where the flange connecting the main chamber to the ion pump. This is a very large and inaccessible flange which makes it difficult to tighten the bolts further. To deal with this, vacuum tape was used to seal the leak.

5.1.1. Pumps

To achieve UHV, several different pumps are used, where each pump has its ideal operating pressure range and way of removing gas. Roughing and turbomolecular pumps are used to achieve a good vacuum before the ion pump can be started. The turbomolecular pump is removing particles mechanically by turbine blades that spins at a high frequency, typically 1000 Hz. Subsequent to the turbopump, before the outlet to atmosphere, there is a roughing pump connected to avoid exposing the turbopump to atmospheric pressures, which can damage the turbine blades. The roughing pump establishes a prevacuum such that the turbo pump can operate in the molecular flow regime. Because molecules can back-flow in through the turbo pump, the lowest pressure achievable for the turbo pump is depending on the pre-vacuum established. In the STM chamber, the turbo pump can be isolated from the chamber by a valve and due to the mechanical vibrations caused by it, the turbo pump was turned off when STM

was performed. A smaller turbopump is attached to the CO and O_2 gas lines and used when gas is changed.

When the pressure has reached $\sim 1 \cdot 10^{-8}$ mbar, an ion pump can be turned on to further lower the pressure. The operating principle is by ionizing gas atoms by electron bombardment, after which they are accelerated onto an electrode by an electric potential. The ion pump does not cause any vibrations and is the only pump running when performing STM.

A titanium sublimation pump (TSP) is used in between the lab sessions at the STM lab. It works by passing a large current through a titanium filament such that titanium evaporates. The evaporated titanium is highly reactive toward other gases, such as oxygen. When a gas molecule strike a fresh surface of Ti, they are irreversibly adsorbed [40]. The TSP is located behind a screen at the bottom of the chamber and the sample holder is facing away from the titanium source whenever it is turned on to avoid titanium contamination on the sample.

5.2. Sample preparation

The samples were cleaned by cycles of sputtering (ion bombardment) and annealing (heating). Sputtering physically removes the topmost layers of the crystals with ion energies in the range of 0.5 keV–5 keV depending on surface composition and how much material is necessary to sputter away. Subsequent annealing is necessary to remove Ar ions that can get embedded in the crystal, desorb adsorbed gas molecules and to recover the surface crystallography. Annealing is usually done with Ohmic heating if the desired temperatures are below $\sim 500\,^{\circ}$C. If higher temperatures or higher heating rates are necessary, electron bombardment can be used. This technique requires a heated filament at the rear side of the crystal and a high voltage bias at the crystal relative to the filament. During heat treatment, impurities from the bulk tend to diffuse to the surface, so that the cycle has to be repeated several times. The methods used are described in the following paragraphs.

De-gassing

Annealing with a high heating rate (flashing) to between 200-300 °C to desorb water and CO from the sample. This was done before subsequent sputtering and annealing cycles.

Sputtering

Ion bombardment (sputtering) of the sample was performed for either 20 or 30 minutes at room temperature. The ion energy used was always 1 keV and Ar pressure betwen $2 \cdot 10^{-5}$ mbar–$4 \cdot 10^{-5}$ mbar to have an ion current of 38 mA–40 mA. This method removes impurities from the surface, but also leaves it in a heavily damaged state.

High voltage annealing

To achieve the desired annealing temperature of 550 °C, high voltage annealing with a bias of 500 V on the crystal was performed. To oxidize some of the carbon which diffuses to the surface, O_2 was released into the chamber and kept at a pressure of around $2 \cdot 10^{-8}$ mbar. Each annealing session started with cycling the crystal from below 300 to 500 °C three times. This was done to let O_2 adsorb on the surface and react with the surface contaminants. Annealing time varied depending on the resulting images in the STM.

5.3. Oxidation

Attempts to form the Pd-($\sqrt{5} \times \sqrt{5}$)R 27° surface oxide was done by lowering a O_2 doser to just above the sample itself, open and lower the pressure which was kept at $5 \cdot 10^{-5}$ mbar or $7 \cdot 10^{-5}$ mbar during the procedure. The doser consists of a microchannel plate, resulting in constant flux across the sample surface. The microchannel plate causes the pressure on the sample surface to be much higher than the pressure measured in the chamber [90]. Between each oxidation session, the sample was cleaned by sputtering and annealing. During oxidation the samples was just heated using Ohmic heating with a starting temperature of around 350 °C. As the sample is out of sight during oxidation, the temperature was monitored using a voltmeter connected to a thermocouple on the manipulator inside the chamber. Tabulated values for the oxidation attempts performed in the STM chamber can be found in Appendix C.

Temperature control

In the STM lab, a thermocouple is attached close to the sample, but not onto to the sample, so the measured temperature is affected by previous heat treatments, thus an equilibrium temperature would take several hours to reach. A Land Cyclops C160L optical pyrometer with an accuracy of ±0.25% °C was used to monitor the temperature

when the sample was in line of sight, i.e. when the O_2 doser was retracted a bit. The pyrometer has a measurement range from 200 to 1400 °C and is connected to a computer running Cyclops logger which reads the temperature at given intervals. A pyrometer determines the temperature by comparing brightness of the object and a reference. As a measure of the reference temperature, a color change with the growth in temperature is taken. The device compares the brightness produced by the radiation of the object whose temperature is to be measured, with that of a reference temperature. The reference temperature is produced by a lamp with a brightness that can be adjusted until its intensity becomes equal to the brightness of the source object. The emissivity from the sample was set to 0.21, which is a bit lower than for pure Pd (0.23) and a window correction was set to account for the change in radiation due to the window between the chamber and the pyrometer.

5.4. LEED

To investigate the surface periodicity after one or several cleaning cycles and before using the STM, LEED was performed. The electron energy range was between 60-110 eV. Using four electrostatic lenses and a Wehnelt electrode the spots which appeared were tuned such that they were as bright as possible for each image. The screen voltage was set to 6 keV for all LEED images and both position on the sample and the electron energy used were as consistent as possible for each session to have comparable results. A standard digital camera (Casio EX-S10) set to a slow shutter speed and high light sensitivity was used to record the fluorescent screen.

5.5. STM

An Omicron UHV STM 1 from Omicron [91] was used to carry out surface investigations on small areas of the sample. A drawing of the UHV chamber used for STM can be seen in Figure 5.2. The STM itself consists of two parts, a scanner and a coarse movement unit that is suspended in springs when used. A coarse movement unit controlled by a remote is used when large movements are required either sideways for moving to a different area or to move the sample closer to the tip. When approaching the tip, a microscope is used to ensure that the tip is not crashed into the surface. The inset in Figure 5.3 shows when the tip is at an intermediate distance and can be moved closer to the sample by the remote control. When the tip almost touches its mirror image in the sample, an automatic step-wise approach controlled by a RHK R9 controller [92] is

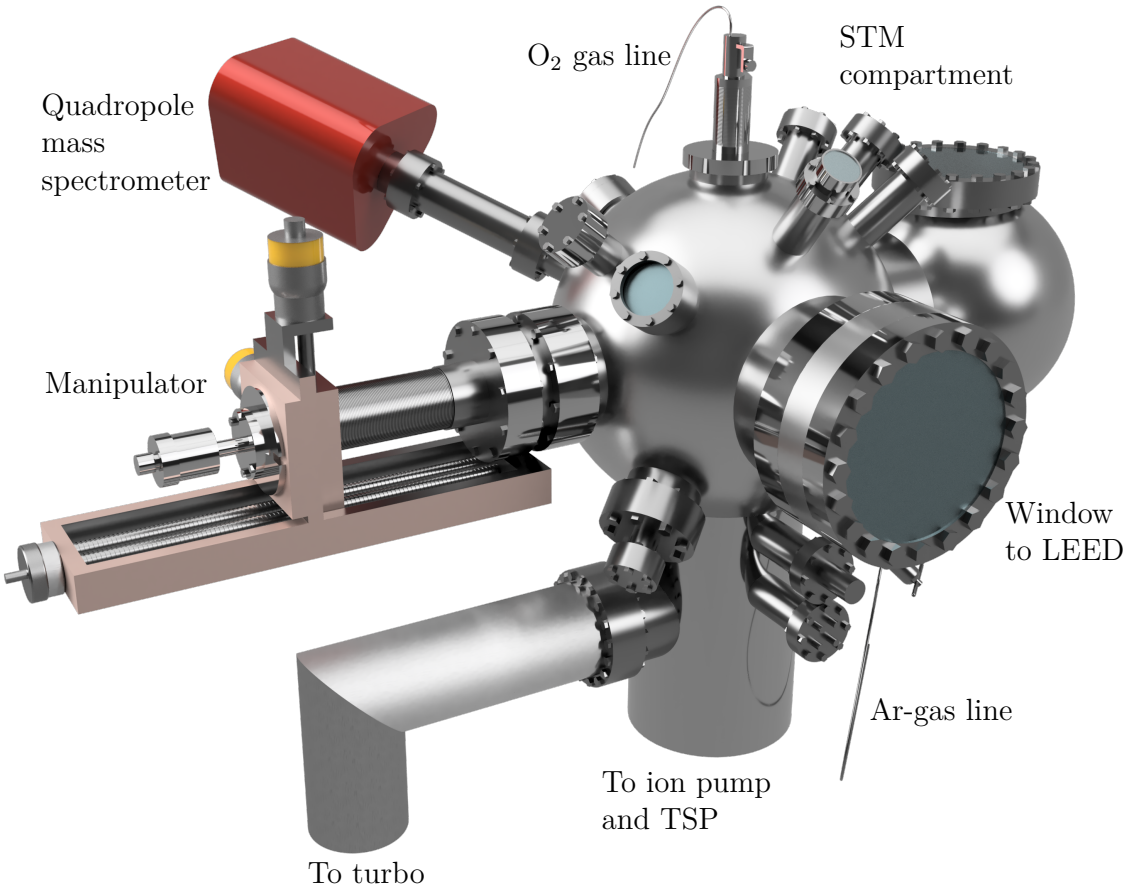

Figure 5.2.: Drawing of the STM chamber with some of its main parts labelled.

employed until a tunnelling current can be measured.

The STM stage is located on a platform which can be unlocked from its storage position and let to rest in springs to dampen vibrations when in use. Around the STM several magnets are placed which will induce an Eddy current in the copper plates attached along the side of the platform whenever the STM vibrates. The Eddy current generated induces an opposing force which further dampens vibrations. Scanning is controlled using software from RHK technologies which is made for the controller installed. Several parameters can be adjusted such as bias voltage, tunnelling current, integral and proportional gain, scan speed and area.

The mechanical pumps and the TSP are always turned off when STM is performed. After oxygen treatment, the pressure in the chamber is too high for the ion pump to be turned on and the chamber will have be pumped down for some hours. This could take from one to several hours depending on the amount of oxygen used, i.e. whether an

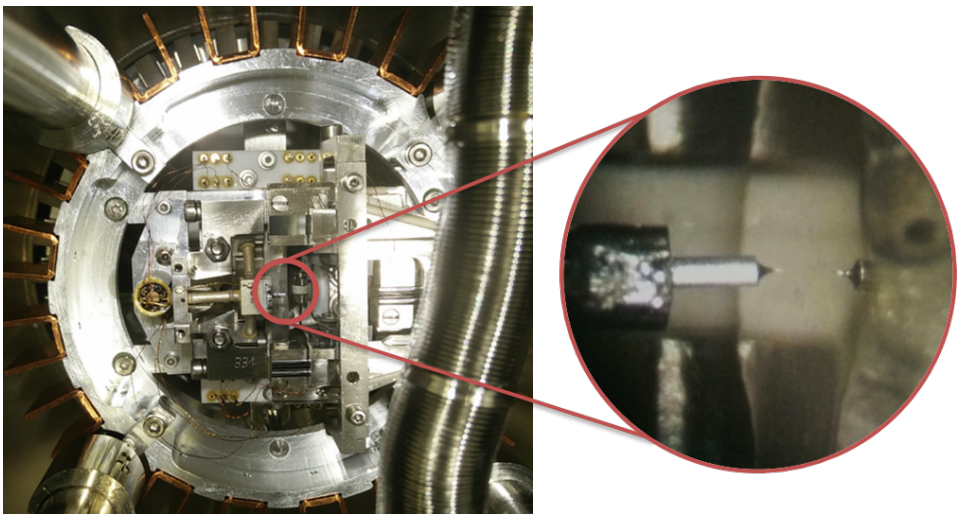

Figure 5.3.: The STM viewed from above without sample inserted. Four springs are used to have the stage hang freely to avoid vibrations. In the copper plates along the outer edge, Eddy currents are induced to further decrease oscillations which can alter the scanning. A wobblestick used for transferring samples and tips between the storage carousel and the STM stage can also be seen. Inset: Approach of the tungsten tip on to the sample viewed through a microscope attached on the outside of the chamber.

oxidation procedure or just annealing with oxygen treatment had been executed. Pressure were always lower than $1 \cdot 10^{-8}$ mbar when performing STM due to the operating limit of the ion pump and to ensure that the electron gun in the LEED did not become damaged, as it was used to verify the average surface structure before STM. Due to structural vibrations in the building and construction work on the outside, STM could only be performed in the late afternoon and during weekends as there would otherwise be too much vibrations.

All images were recorded with a resolution of 512 lines in constant current mode with both forward and backward directions recorded. The parameters were changed based on the topography of the scanning area and the feedback response from controller to achieve the best image possible. If a flat area was deemed large enough, further increase in resolution was attempted. To image larger parts of the surface, e.g. 250×250 nm^2 a high scan speed was used, the bias voltage and tunnelling current was varied to generate as good images as possible. This was done by scanning the same area several times while tweaking the parameters for each time. To remove any particles the tip might pick up, an automatic current pulse is manually triggered to remove any possible contaminants residing on the tip or surface. Both negative and positive bias was used, and for tip sharpening, a method by Wintterlin *et. al* [93] was applied. It involves raising the bias to a large negative value and scan for a few lines. This will cause electromigration of

the outmost atoms on the tip down towards the sample, resulting in a prolonged and hopefully sharper tip.

Image analysis

To analyze the images recorded from the STM, Gwyddion was used [94]. It provides a large number of data processing functions, such as statistical characterization, levelling and data correction, filtering or grain marking functions. The functions used for the images in this thesis includes levelling of data by mean plane subtraction, correct lines by matching median height, correct horizontal lines and stretch color range to a certain part of the data. These functions are used to make images clearer such that they are easier to interpret.

Tip preparation

A tungsten tip was prepared using electrochemical etching. The procedure is to etch a small piece of a polycrystalline W wire in a mixture of $3\,\mathrm{mol\,dm^{-3}}$ KOH and with a DC voltage set at 8 V and a cut-off current at 1.5 mA. The voltage and current are controlled by a script in Labview and a digital-to-analog converter that stops the etching when the cut-off current is reached. The tip is subsequently dipped in three different beakers with de-ionized water and inspected in a light microscope. If the tip is deemed suitable for STM it can be mounted on a Omicron tip holder and loaded into the vacuum chamber. If not, the etching procedure is repeated until a satisfying result is achieved. The etched tip should not be exposed to atmosphere for a prolonged period of time as W oxidizes in ambient air. The same tip was used for all STM results in this report.

5.6. XPS

In-house investigations of the surface composition was performed using a KRATOS Axis Ultra DLD system. The x-ray source was a monochromatic Al Kα, with an energy of 1486.7 eV and an analysis area of 700×300 µm^2. The Pd_3Au single crystal was placed in a quartz sample holder made by the Glass Blowing Workshop at NTNU and inserted into the chamber. Pass energy was set to 80 for survey scans with 1 eV steps for the whole survey (1200 to -5 eV) and 0.25 eV energy steps for surveys at lower energies (600 to -5 eV). All measurements were done at normal emission angle and core levels were acquired with a pass energy of 10, energy steps of 0.05 eV for C 1s and O 1s and 0.025 for Pd 3d and Au 4f. Dwell time was 400 ms for all core level scans. Survey scans and core

level scans were acquired before and after H_2 exposure. Since the sample is mounted on an insulating sample holder, photoelectrons that are emitted needs to be replaced to avoid charging of the sample. This was done using a charge neutralizer or flood gun which is a low energy electron gun that flood the sample with electrons to compensate for the positive charge left after electron emission.

5.6.1. Reaction cell

To expose the sample to H_2 a reaction cell connected to the XPS chamber was used. It is a high pressure and temperature cell which has operating limit of 30 bar or 1000 °C. In this project, (relatively) low partial pressure of H_2 were required, but the reaction cell needs pressures over 1 bar since there is no pump on the exhaust. Thus, in order to apply a low partial pressue of hydrogen pressure, it would have to be diluted with Ar. This is to avoid contamination coming from the outside exhaust into the cell and contaminating the sample. The flow rates for the gases were set to 2 ml/ min and 98 ml/ min for H_2 and Ar, respectively, corresponding to $2 \cdot 10^{-2}$ bar partial pressure of H_2. The sample was heated to the desired temperature, exposed to H_2 for 2 minutes and then let to cool down in Ar. An illustration of the reaction cell is seen in Figure 5.4.

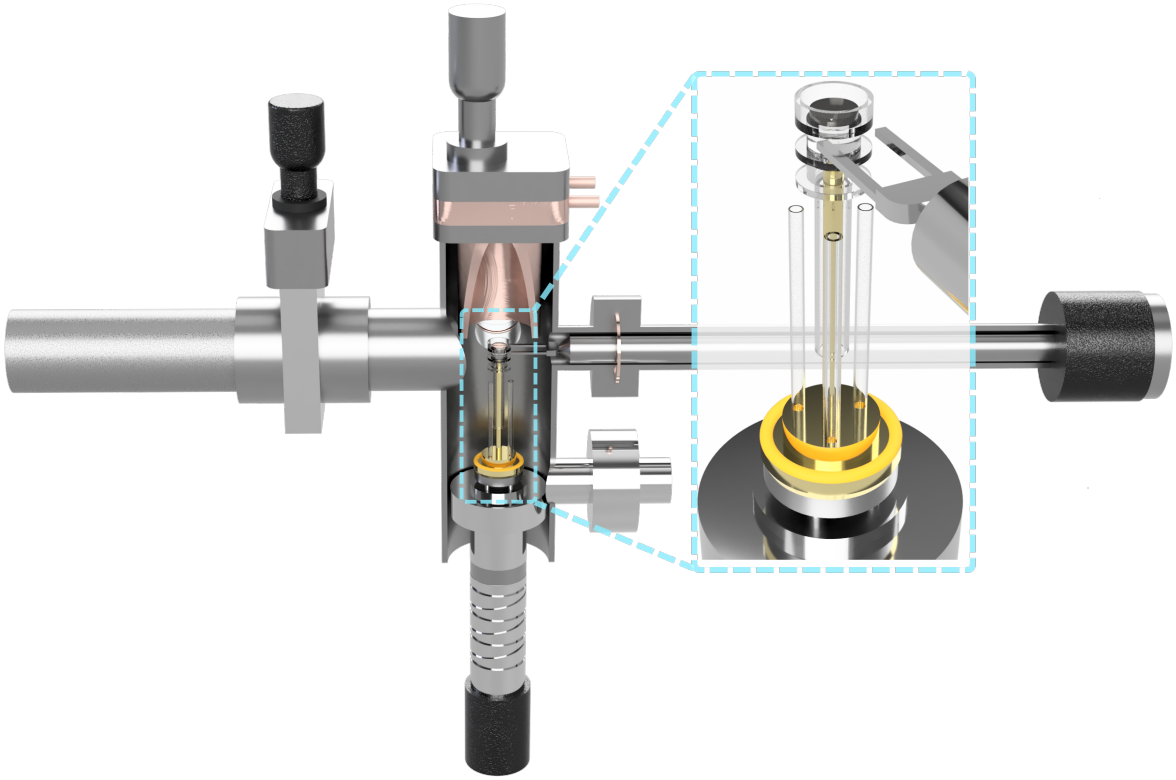

Figure 5.4.: Drawing of the reaction cell used to expose the sample to H_2. The transfer arm to move samples back and forth from the XPS chamber and its fork is seen. The sample holder is placed on top of a Au coated rod with two gas inlets and one outlet on the side, seen in the inset. To seal the reaction cell, the rod is lifted upwards toward the heating part located on top such that the orange PTFE gasket seen below the glass part seals of the cell from the vacuum environment. The heating is done Ohmicly and the housing is cooled with water to avoid damaging gaskets.

5.7. High-resolution XPS

To perform XPS with a varying photon energy, synchrotron radiation is needed. Synchrotron radiation is generated by bending electrons travelling close to the speed of light using bending magnets, wigglers or undulators. Bending magnets are used to change the direction of the beam, making it possible to have a circular accelerator. When the relativistic electrons are continuously bent using such a magnet they emit x-rays tangentially to the path of the electrons. This results in x-rays with a continuous energy spectrum.

In between bending magnets, in straight paths, wigglers or undulators are placed which are termed insertion devices because they are inserted into accelerator tracks. Insertion devices are made up of a series of small magnets with alternating polarity. When electrons enter such a device they are forced "up" and "down" several times, each time emitting x-rays. Since this occurs many times in the same device, the x-rays produced are many times more intense than those generated by the bending magnets. In a wiggler the period and the strength of the magnetic field is not tuned to the frequency of radiation produced by the electrons, which results in broad energy spectrum. It can be considered as a series of bending magnets concatenated together. In an undulator, rows of magnets having alternating polarity are placed which produces a narrow, but very intense energy spectrum. The gap between the rows of magnets can be changed to fine-tune the wavelength of the x-rays

The electrons are emitted from an electron source, accelerated by an electric field using either (or both) a linear accelerator or a booster ring and then let into the storage ring. The storage ring is where the electrons are stored (kinetic energy kept constant) after they have been accelerated to their desired kinetic energy and "kicked" in. On ASTRID 2, the light source applied here, they use the top-up mode to inject new electrons into the ring, which means that the electron current is maintained as steady as possible by injecting small amounts of current. It produces a more stable beam by keeping the heat loads and signal strengths constant over long time periods in both the storage ring and on the beamlines. A sketch of a synchrotron setup is seen in Figure 5.5.

5.7.1. MATline on ASTRID 2

To perform high-resolution XPS (HRXPS) with a tunable photon energy, the beamline MATline at Aarhus University was employed. The beam line is equipped with a Scienta electron energy analyser and a SX-700 monochromator and has a reported usable energy range from 20 eV to 700 eV. During the experiments, the base pressure was never below

Table 5.1.: Photon energies, pass energies and repetitions for different core levels acquired at MATline.

	O 1s	Pd 3d	C 1s	Au $4f_{7/2}$	Valence band
Photon energy (eV)	610	390	390	150	40
Pass energy (eV)	75	20	75	20	20
Repetitions	1/2	6	3	4	1

$5 \cdot 10^{-9}$ mbar due to a large amount of residual water in the chamber. In addition, the ion pumps contained large amounts of CO and were not pumping efficiently. This is believed to have an impact on the resolution of the spectra, where it will be more difficult to assign components to the various chemical states found on the surface. There is also a LEED system installed in the chamber, but this was not working, so one could not be certain about what type of overlayer structure there was on the sample.

Sputtering, annealing and oxidation were performed using the same procedure as described earlier in the text. Core levels were measured with the photon energies found in Table 5.1. The scans were performed with normal (0°) and grazing (60°) emission.

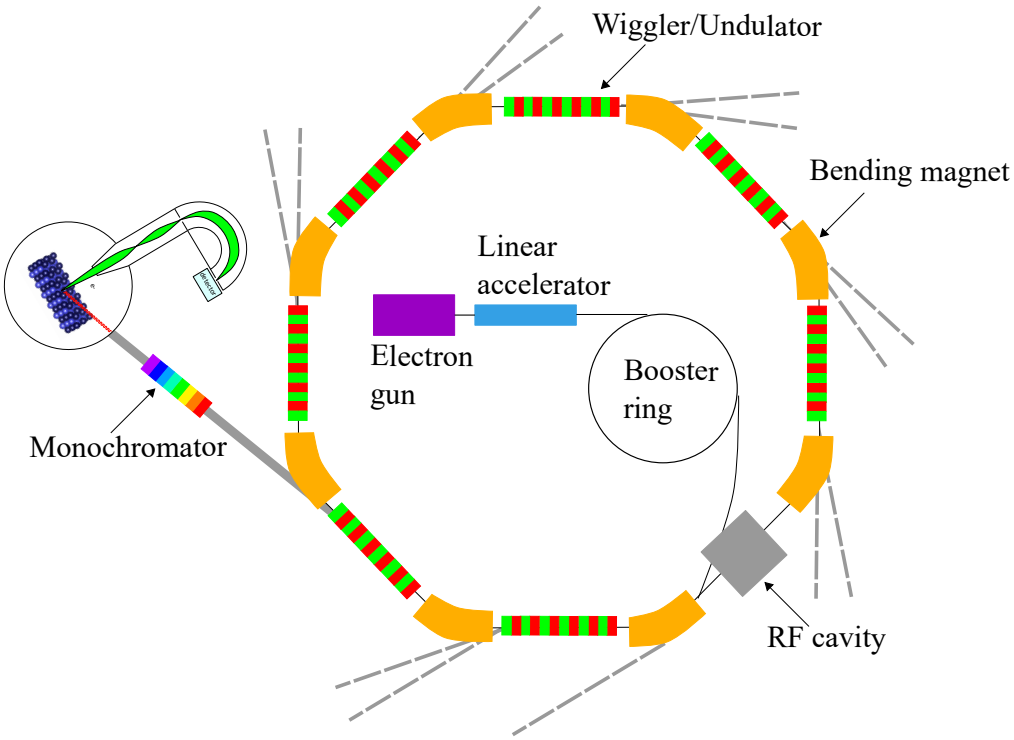

Figure 5.5.: Sketch of a syncrotron showing the most important parts. Electrons are emitted from an electron source, first accelerated in a linear accelerator and subsequently in a booster ring. When the electrons have reached a desired kinetic energy they are let into the storage ring. In the storage ring, bending magnets are used to bend the electron beam, making it possible to have a circular accelerator. Monochromators are adjusted to measure the sample with the desired photon energy. The kinetic energy of the electrons is adjusted each time they pass through the RF cavity. Adapted with permission from [89].

5.8. Spectrum analysis and quantification

Line shapes from XP spectra can be described using a convolution of Lorentzian and Gaussian functions. For asymmetric peaks, which is common for metals, an asymmetry factor has to be added to the convolution. Spectra were plotted, core levels analyzed and elements quantified using CasaXPS [95]. For XPS performed at NTNU, a shirley background was subtracted to decompose Pd $3d_{5/2}$, C 1s and Au $4f_{7/2}$ core levels. The Pd core levels were fitted using a Lorentzian asymmetric lineshape with a tail damping. The lineshape is equivalent to the asymptotic form of the Doniach-Sunjic linehsape, but it's not infinite in nature. The C 1s core levels were fitted using a Gaussian-Lorentzian product function and for Au $4f_{7/2}$, a numerical convolution of a Lorentzian with a Gaussian was used. It resembles the traditional Voigt profiles.

Relative sensitivity factors were obtained from a library for the Kratos XPS system which accounts for the dependence of the photoemission intensity on kinetic energy in the cross section. To determine the ratio of Au and Pd in the sample, the area of the Pd $3d_{5/2}$ and Au $4f_{7/2}$ core levels were used. Overview of cross sections for Pd, Au, O and C can be found in Table D.1 in Appendix D. Since the sample is mounted on a non-conductive sample holder of quartz, a charge neutraliser is employed which shifts the whole spectrum to lower energies by severel eV. To correct for this, the individual spectra has to be calibrated with a reference, which here was taken to be the bulk component from Pd $3d_{5/2}$.

HRXPS data from MATline were fitted using a linear background for C 1s and Pd 3d while a Shirley background was used for Au $4f_{7/2}$. The reason for the use of different backgrounds was due to the measured signal. Both Pd 3d and C 1s was measured across a wide energy range which resulted in a significant decrease of the measured intensity from high to low binding energy. Au $4f_{7/2}$ on the other hand was measured with a narrow energy range, which allowed the use of a Shirley background. This was done in order to be consistent with the measurements from home XPS. The core levels were fitted with the same lineshapes as mentioned above. Reference binding energy values for the elements present were obtained from [63]. The Fermi edge was recorded each time a core level was measured at a new photon energy, fitted using a complementary error function in CasaXPS and used to adjust the binding energy scale for the respective core level spectrum. The number of repetitions was for most cases consistent with those presented in Table 5.1, but a few spectra had deviations from the reported number of repetitions. To adjust for this, these spectra were multiplied with a factor depending on the number of missing repetitions.

5.9. Health, safety and environment

The gases used in the experiments were O_2, H_2 and Ar with smaller amounts of He for leak detection. Ar and He are inert and nonpoisonous gases, but if there is a significant leak, they can expel breathable air from the local environment. Significant O_2 leaks can cause explosive fires if there's a spark and H_2 is a highly explosive gas. The XPS and STM rooms have gas alarms for H_2 and CO which will detect any leak rapidly and sound the alarm. In both rooms there are gas bottles containing CO which is highly poisonous. In the XPS setup, an x-ray gun is used to excite electrons and is located inside the vacuum chamber which have radiation proof windows. One should be aware of the high voltage equipment in such a lab and not commit any fouls operating them as they can give the user significant electric shock. This is especially important for the STM lab where more of the equipment is manually operated compared to the XPS lab. In the STM lab there is also a working alone alarm which the user should wear when working alone in the lab. For spotwelding of samples and handling of solutions for etching and cleaning, safety goggles were used.

Chapter 6.

The materials system

Presented here is information regarding the materials investigated.

6.1. Single crystals

Two different single crystals, both with the bulk composition Pd_3Au and surface (100) were acquired from Surface Preparation Laboratory. The first crystal to be examined in the UHV chamber and later by XPS was approximately 6 mm in diameter. The second crystal investigated in the UHV chamber and later at the Matline beamline was slightly smaller. Both crystals had regions of different color contrast visible to the naked eye on the surface.

6.1.1. Palladium and gold

Palladium, atomic number 46, a 4d transition metal and gold, atomic number 79, forms a solid solution without miscibility gap in the whole range of concentrations when alloyed together [96]. Ruban et al. [97] calculated that if Au is the host and Pd the solute, there will be a moderate antisegreation. If Pd is the host and Au the solute, which is the case for Pd_3Au, there will be a moderate segregation and Au will be enriched in the surface in a non-reactive environment (UHV). Some of the main individual properties of Pd and Au are listed in Table 6.1.

Table 6.1.: Properties of Pd and Au. From [98]

	Lattice constant (Å)	Melting point (°C)	Crystal structure
Pd	3.8823	1554.8	fcc
Au	4.0786	1064.2	fcc

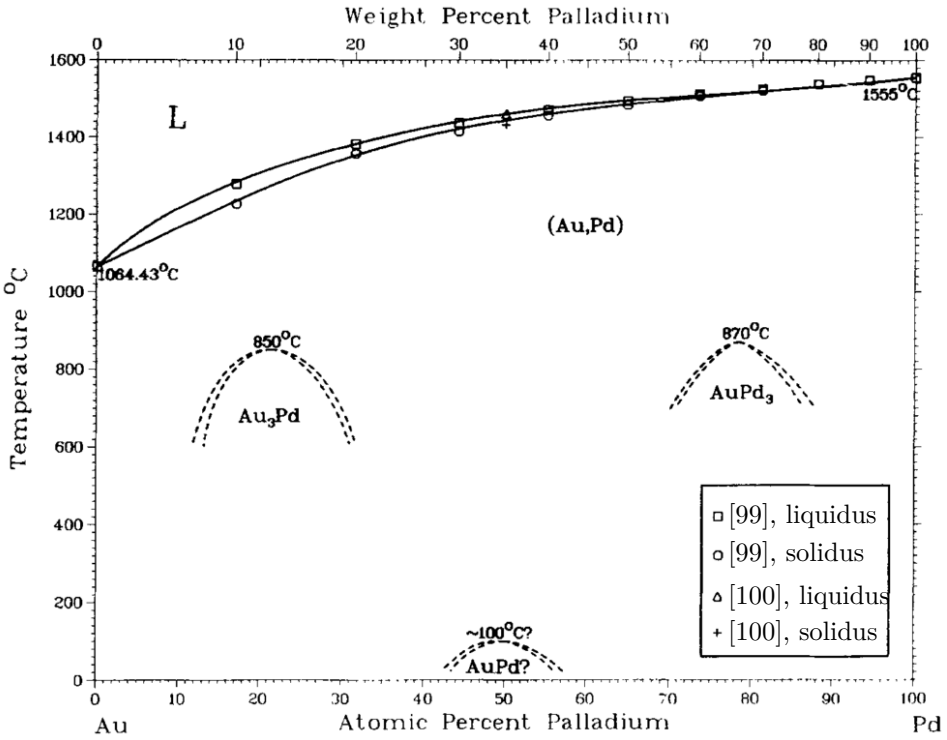

Figure 6.1.: Phase diagram for Au-Pd. Adapted with permission from [101].

In Figure 6.1, the dashed lines represents the transition temperature between the ordered (low temperature) and disordered (high temperature) states of the Pd-Au alloy systems. The alloy is completely ordered at absolute zero and becomes less ordered as the temperature is increased, until a transition temperature is reached above which the structure is disordered. This transition temperature has been determined experimentally using electron diffraction for a Pd-Au alloy by Matsuo et al. [102] and Kawasaki et al. [103]. It has been found that the degree of order for the ordered alloy Pd_3Au is much smaller than for the alloy $PdAu_3$ [101]. The transition temperature region between ordered and disordered phases for Pd_3Au alloys are shown in Figure 6.2.

Generally speaking about transition metals; in the periodic table the reactivity decreases farther down and the adsorbate bond becomes stronger farther to the left. Looking into the electronic properties of Pd and Au, they are very different. Au is known for being very inert, while Pd on the other hand is applied in a range of catalytic reactions due to its reactivity. This reactivity can be explained using the d-band model by Hammer and Nørskov [1, 77]. Since Pd has a d-band center closer to the Fermi energy due to more unfilled d-states above the Fermi energy, this causes an adsorbate to couple, giving rise to a bonding state below the Fermi energy and an antibonding state above, which results in a strong bond. Au on the other hand has completely filled d-bands well

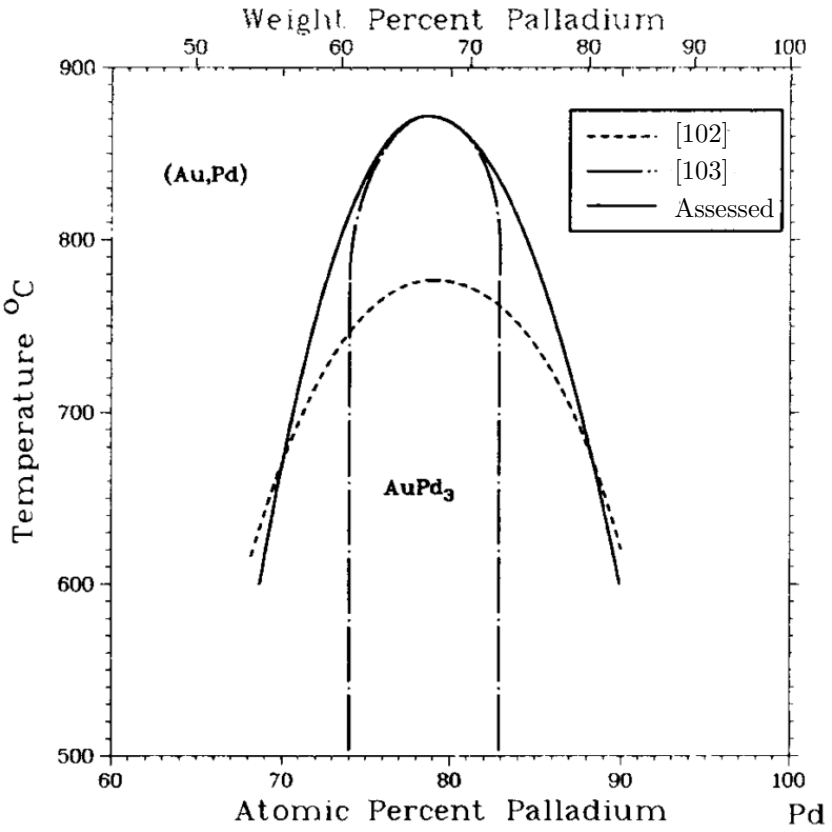

Figure 6.2.: Assessed phase diagram for Au-Pd, showing the order-disorder transition for Pd_3Au. Adapted with permission from [101].

below the Fermi energy, i.e. a d-band center further down, and subsequently a lower reactivity. An adsorbing atom or molecule on a Au surface will have both the bonding and anti-bonding state below the Fermi energy, resulting in a weaker bond [1].

6.1.2. Clean and oxidized Pd(100) surfaces

The clean Pd(100) surface has interatomic distance of $a/\sqrt{2} = 2.75$ Å. Exposing the surface to oxygen in UHV results in the formation of up to four different oxide structures depending on the monolayer coverage. At 0.25 ML a p(2×2) structure is formed, c(2×2) at 0.5 ML, p(5 × 5) at 0.75 ML and $(\sqrt{5} \times \sqrt{5})$R 27° at 0.8 ML [104–106]. The latter has been widely studied over the last decades. Its structure can be seen in Figure 6.4 and a STM image with atomic resolution in Figure 6.3a. It consists of a single, strained PdO(101) layer on top of the Pd(100) substrate. The Pd atoms in the $(\sqrt{5} \times \sqrt{5})$R27° oxide have two-fold and four-fold oxygen coordinated Pd atoms.

Bulk PdO can be formed by a transformation from the $\sqrt{5}$ oxide at 400 °C and 50 mbar O_2 pressure [24]. A bulk like epitxial PdO film is formed at pressures beyond 1 mbar

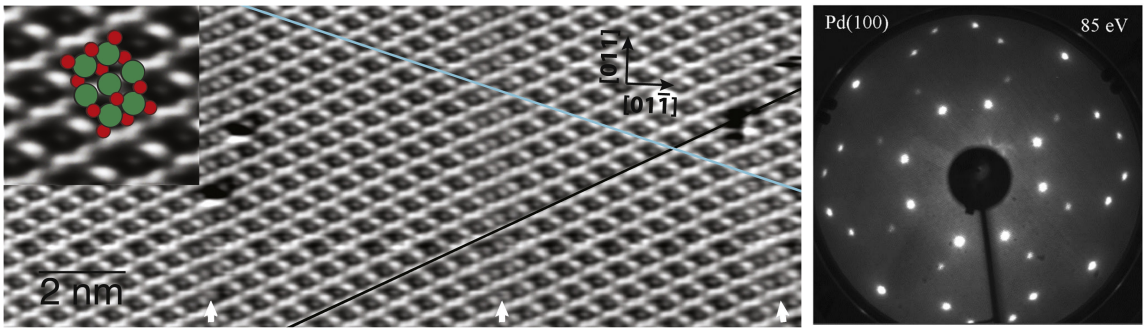

(a) (b)

Figure 6.3.: (a) Atomically resolved STM image of the Pd(100)-($\sqrt{5} \times \sqrt{5}$)R27°-PdO(101). White arrows indicates domains with distorted periodicity. The black line is along a row of Pd atoms which has preserved the two-oxygen coordination while the blue line indicates a coordination shift from two to four oxygen from left to right across the distorted region. Figure adapted with permission from [111]. (b) LEED pattern of the ($\sqrt{5} \times \sqrt{5}$)R27° surface oxide. Adapted with permission from [2].

and temperatures above 300 °C [107, 108]. Applying density function theory (DFT), Seriani et al. [109] have predicted that the surface oxide grow by a Stranski-Krastanov mode with a critical thickness of 1 ML. Islands of bulk oxide grow epitaxially in the same (101) direction as the ($\sqrt{5} \times \sqrt{5}$)R27° surface oxide when there is lower excess of O_2 in the gas mixture. This has recently been suggested by Shipilin et al. [110] and is illustrated in Figure 6.4c.

6.1.3. Surface of PdAu single crystals

Alloying Pd with Au affects the reaction dynamics on the active surface of a catalyst. Many studies have reported that heating PdAu in UHV results in Au enrichment in the surface [7, 112–116] where (110) and (111) surfaces have same amount of Au enrichment [117]. The surface composition can change drastically compared to the bulk by annealing, whereas Yi et al. [118] reported annealing a 1:1 Pd-Au mixture at 800 K resulted in formation of a surface with composition $Au_{0.8}Pd_{0.2}$.

To determine whether a surface alloy of Pd-Au is formed, model catalysts can be made in UHV by depositing a thin film of Au onto a Pd single crystal and heating to various temperatures to allow the gold to diffuse into the Pd substrate. Using this method, it is found that Au grows in a Frank-van der Merve (layer-by-layer) fashion at 300 K and starts to diffuse into the bulk (Pd) at annealing temperatures higher than 600 K [119].

Deposition of Pd on Au have shown that when Pd is deposited on Au(111) in thicker layers it displays a Volmer-Weber growth mode (island upon island) with the formation

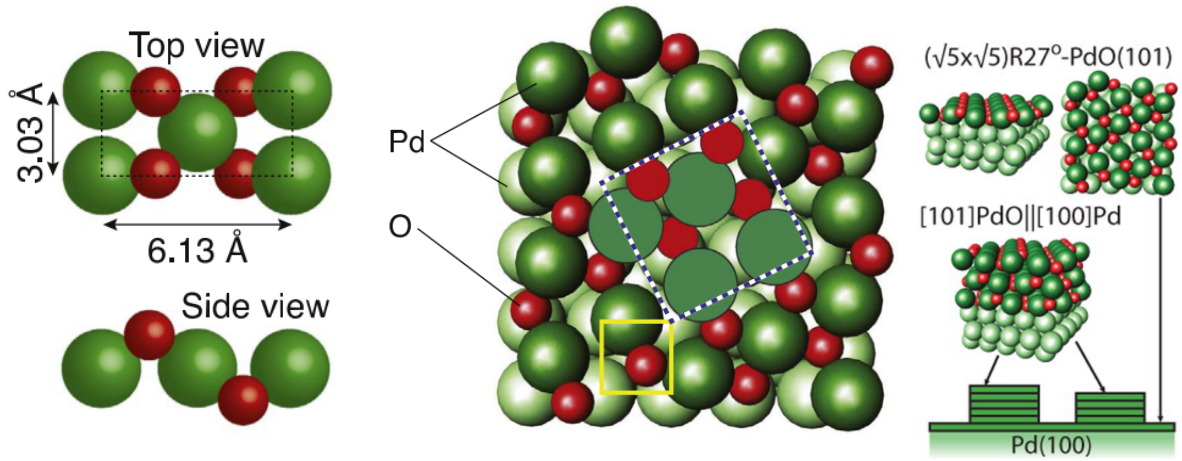

(a) **(b)** **(c)**

Figure 6.4.: (a) PdO(101) unit cell in bulk PdO. Figure from [111]. (b) Schematic representation of the $(\sqrt{5} \times \sqrt{5})$R27° surface oxide structure. The oxide unit cell is shown with dashed lines and the Pd(100) until cell with yellow lines. Figure from [111]. (c) Stranski-Krastanov growth mode of epitaxial oxide growth. Adapted with permission from [110]

of monolayer Pd islands observed up until 0.6 ML coverage. Above this coverage, the growth of higher layers leads to a roughened surface [120]. DFT calculations predicts interaction between Pd atoms to be small, with or without CO on them. Thus, they will not aggregate to form Pd islands within the surface layer due to adsorbants, nor will they form Pd domains in the bulk [121].

The segregation properties are changed if chemisorbing species are introduced. Pd which has a higher bonding energy than Au will segregate to the surface if the partial pressure of CO is higher than 0.13 mbar in room temperature [113, 122]. By introducing O_2, DFT calculations has predicted that the surface will be enriched in Pd in a PdAu(111) alloy [123] and for Pd atoms substituted in a Au(111) surface [124].

Chapter 7.

Computational results

The first step when characterizing a material by DFT is to investigate the bulk properties. We start with pure metals as a reference and to validate their lattice parameters, then we investigate the Pd_3Au alloy and effect of alloying on different properties of Pd-based systems.

The ideal, calculated lattice parameter is the one which results in the lowest energy of the system. This is done by calculating the energy for a range of lattice constants, a and taking the minimum by using a Birch-Murnaghan fit for the calculated lattice constants [125]. The resulting energy-minima curves are presented in Figure 7.1.

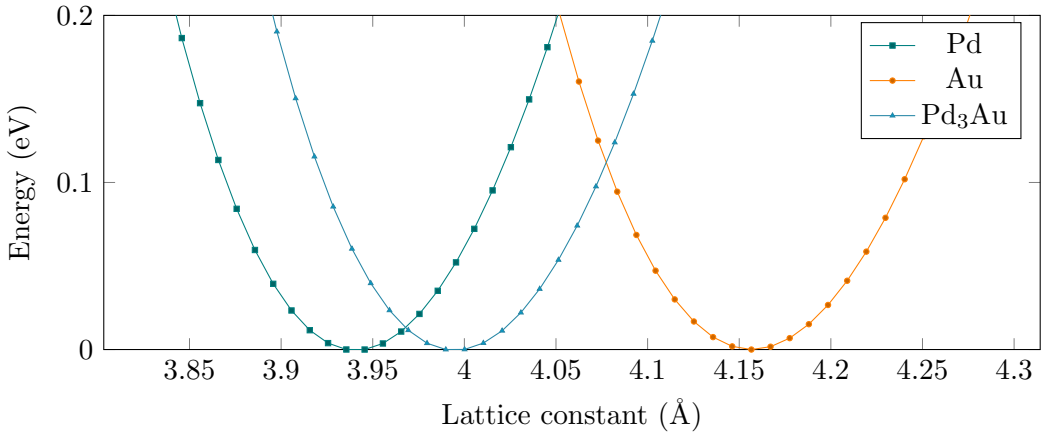

Figure 7.1.: Calculated lattice constants for Pd, Pd_3Au and Au. Energy scale set to 0 for the minima of each curve.

The results from calculations of the bulks phases are displayed in Table 7.1. The calculated lattice parameters shows good agreement with calculated values in the literature [126, 127]. PBE functionals have a tendency to overestimate interatomic distances due to the diverging exchange potential at the nuclei [128, 129]. A large deviation of the experimentally measured bulk moduli is found and the reason for this inconsistency

between experiment and calculations is caused by the inadequate description of van der Waals interactions in the calculations [130].

Table 7.1.: Bulk properties for Pd, Au and Pd_3Au. All reference values from [126] if nothing else specified.

	a (Å)			B (GPa)		
	This work	Exp	PBE	This work	Exp	PBE
Au	4.156	4.079	4.180	141	167	131
Pd_3Au	3.995		4.027[1]	162		
Pd	3.940	3.881	3.948	168	195	170

7.1. Surface Stability

The surface energies of monometallic slabs of Au and Pd with orientation (100) were also calculated, displayed in Table 7.2, and compared with the literature to verify the methodology used. The orientation chosen for calculations was (100) as it is the orientation of the crystals used in the experimental part, but it is evident from Table 7.2, that the (111) surfaces are more stable. The values calculated resemble closely those reported in the literature, verifying the methodology used in this work.

Table 7.2.: Surface energies of monometallic Pd and Au slabs.

.	Surface energy (meV/Å^2)		
	This work	Exp [132]	PBE [133]
Au(110)			51.64
Au(100)	54.64		53.71
Au(111)		93.63	46.31
Pd(110)			98.24
Pd(100)	95.37		95.22
Pd(111)		125.03	83.52

To investigate the stability of a $Pd_3Au(100)$ surface, calculations were performed with the different configurations presented in Figure 7.2. These results are presented in Table

[1]From Vasi *et. al* [131], performed using PWscf code of the Quantum ESPRESSO distribution.

7.3, and there is a clear trend of decreasing stability with increasing Pd concentration in the surface layer and it is more favourable for Au to reside closer to the surface than deeper into the bulk. Since the lowest surface energy is found for the Au-terminated slab, a more Au rich surface will be the most a more favourable termination in vacuum. This is in agreement with experimentally reported results [7, 31, 115, 116, 134–137], and previous DFT studies on Pd-Au alloys [45, 112, 121, 123, 124, 131, 138, 139]. The reader should note the labelling of these figures as they will be used extensively throughout this chapter to describe various properties on these surfaces.

Table 7.3.: Surface energies of structures with a varying ratio of Au/Pd in the surface.

Figure	Pd atoms in surface (subsurface)	Surface energy (meV/Å^2)
a)	0(8)	79.12
b)	1(8)	81.72
c)	1(7)	83.99
d)	4(8)	88.43
e)	4(5)	92.50
f)	6(6)	101.46
g)	7(5)	105.53
h)	8(4)	110.27

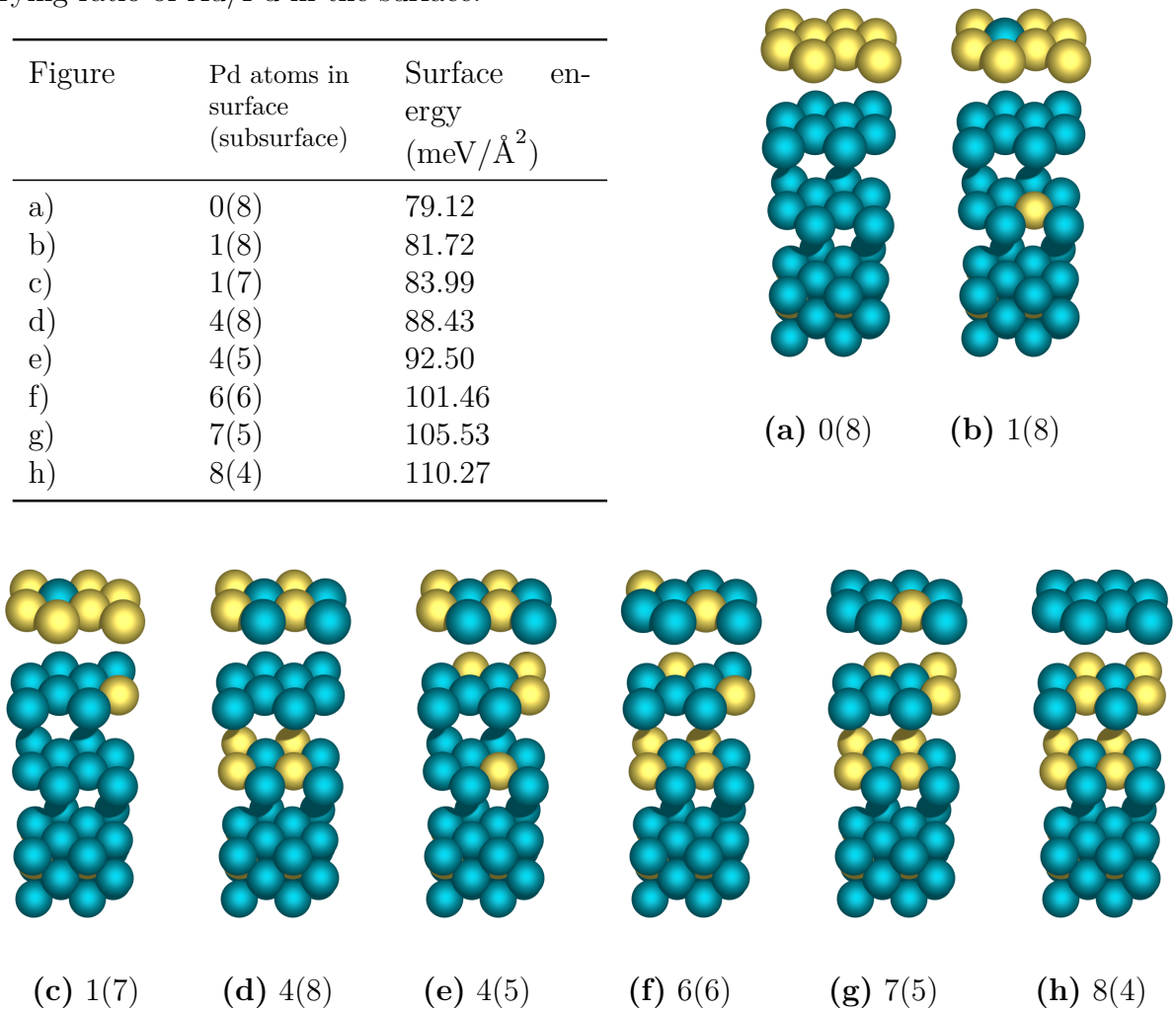

(a) 0(8) **(b)** 1(8) **(c)** 1(7) **(d)** 4(8) **(e)** 4(5) **(f)** 6(6) **(g)** 7(5) **(h)** 8(4)

Figure 7.2.: The structures used to calculate surface energies with the amount of Pd atoms found in the surface (subsurface) labelled. **(d)** is the slab with bulk composition. Additional space is added between the layers to make it easier to see the composition. Color code: Pd (blue), Au (yellow).

7.2. Adsorption of Carbon

Adsorption is one of the main features to study when investigating materials for catalytic properties. Experimentally it has been observed that C diffuses to the surface region when annealing in vacuum [140]. To better understand how this migration affects the termination of the slab, the adsorption energy of C atoms on different sites has been investigated.

A large overview over the possible adsorption sites is seen in Figure 7.3. Three different adsorption sites are considered for adsorption of C atoms on the $Pd_3Au(100)$ surface; the top site (T) is above a single atom, the bridge site (B) is between two neighbouring atoms, and the hollow site (H) is surrounded by four atoms. Figure 7.3 elucidate the changes in adsorption energies for different configuration and with respect to their adsorptions sites. Geometry optimization has been carried out without any constraints to find the most stable adsorption site. As shown in the energy profile in Figure 7.3, the hollow site is found to be the most favourable adsorption site for C atoms. The top and bridges sites were, however, found to be not stable adsorption sites (except for Au terminated surface) for C atoms, and they tend to diffuse to the adjacent hollow sites during the relaxation. Hence, we fixed the x and y coordinates of the C atoms to keep them in the top and bridge adsorption sites while relaxing the distance along the z-axis (perpendicular to the surface). The dashed lines in the energy profile represent the adsorption sites with constraints.

The most favourable adsorption sites are hollow sites with a Pd atom beneath. Hollow sites with an Au atom beneath are less favourable. The trend is however clear: the more Pd-rich surface, the larger the adsorption energy making it more favourable to form a bond.

An additional C atom was buried beneath the top-most layer. For a Au-rich surface it is more favourable for C to go into the bulk, due to the higher concentration of Pd. On the other hand, for a Pd rich surface, it is less favourable to reside below than on top of the surface.

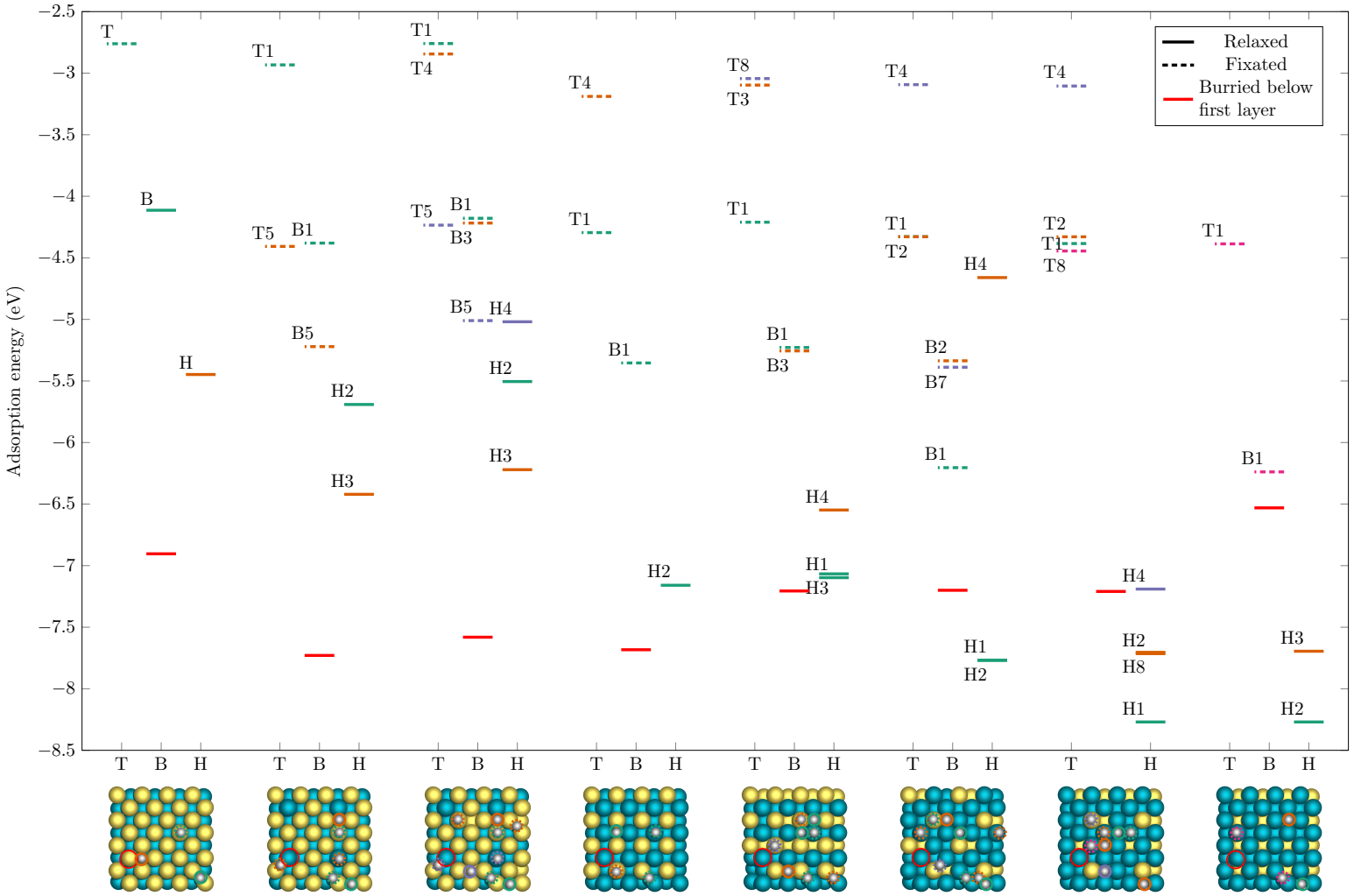

Figure 7.3.: The calculated adsorption energy for C atoms on different adsorptions sites (i.e. top (T), bridge (B), and hollow (H) sites) of various Pd3Au (100) configurations. The slabs in this figure are 2×2 that of the calculated slabs for visualization only and the surfaces have increasing surface energy from left to right (for the clean surface). Lines are coloured and drawn accordingly to the data points on the surface slabs. Buried C atom beneath red circled atom on the respective slab. The dashed lines in the energy profile represent the adsorption sites with constraints.

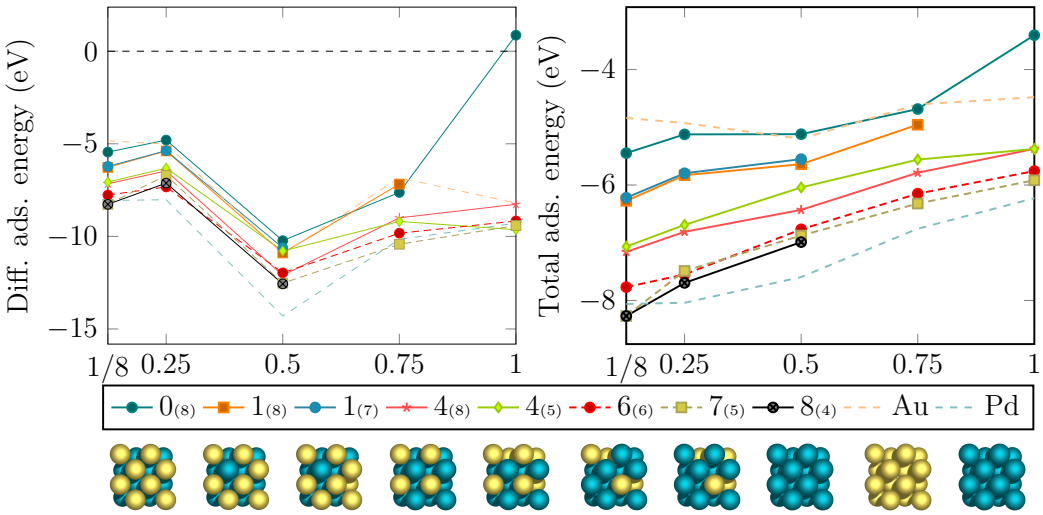

Figure 7.4.: Differential and total adsorption energy as a function of carbon coverage on the surface. The legend describes the amount of Palladium in the surface and (subsurface) with images of the clean surfaces attached. 7.2.

Effects of carbon coverage

Increasing the number of carbon on the surface will affect the stability of the systems. This was investigated by increasing the monolayer (ML) coverage from 1/8 which corresponds to 1 adsorbed C up to 1 ML coverage, where 8 C atoms are adsorbed. The calculations show that going from 0.75 coverage to 1 coverage for the Au terminated surface is not energetically favourable. All other terminations does not have a differential adsorption energy above 0 and will thus be stable for the full coverage. This is also the case for the monometallic Au slab. Atomic carbon has four coordination numbers, readily forming bonds to carbon or other elements as we dont have free carbon or carbon gas. There are however relatively large structural changes in the alloyed slabs when the coverage is increasing, which the structures in Figure 7.5 illustrates. Some of the adsorbed carbon atoms formed C–C bonds on the metal surface. This might be due to asymmetric distribution of Pd and Au atoms in the top-most layers which causes C atoms to migrate to more favourable positions. These features caused a large change in the total energy of the structure and are not added to the plots showing differential and total adsorption energy, Figure 7.4. However, such carbon structures have been observed experimentally by STM on $Pd_3Au(100)$[6] and Pd(100)[52] surfaces, in which they have been referred to as worm-like features. Further calculations can be performed to assess how these features form, but that is beyond the scope of this work.

For the bulk terminated surface, Figure 7.5d, the Au atoms are pushed upwards while the Pd atoms pulled downward. This causes the terminating Au atoms to be found 0.6

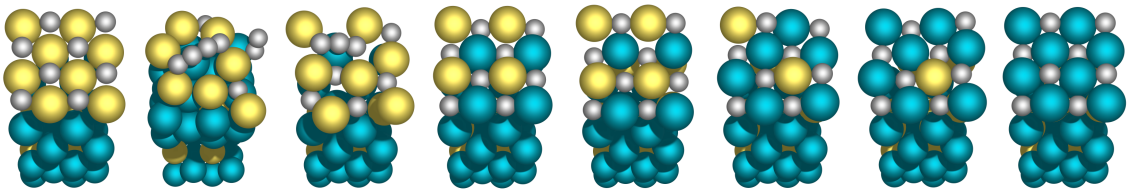

(a) 0(8) **(b)** 1(8) **(c)** 1(7) **(d)** 4(8) **(e)** 4(5) **(f)** 6(6) **(g)** 7(5) **(h)** 8(4)

Figure 7.5.: Surface slabs at 1 ML coverage with the number of Pd atoms in the surface and (subsurface) labelled. Especially some of the Au rich surfaces have large structural changes, but not the Au terminated surface.

Å higher up than the terminating Pd atoms. The bond length also varies depending on the adjacent atoms and whether the hollow site is Au or Pd. For the Pd terminated surface, Figure 7.5h, the bond length to the atom beneath is 1.89 Å and 3.12 Å if the atom is Pd and Au, respectively. Carbon on the Au terminated surface, Figure 7.5a, have a bond length to the atom beneath of 3.05 Å although the underlying atom is Pd. The surface atoms in this case are in compressive strain and that might be one of the reason for not allowing carbon to bond closer to the Pd atom. The reason for this strain is caused by the smaller lattice constant in Pd_3Au than for monometallic Au.

7.3. Charge analysis

The Bader analysis is also performed to quantify the mount of electron transfer between the adsorbed C atoms and the $Pd_3Au(100)$ surface. The adjacent (nearest neighbour) Pd/Au atoms to the carbon atom are selected for charge analysis. By taking the difference between the partial charges on adjacent atoms before and after adsorption of C atoms we can determine the amount of charge transfer. The correlation between the adsorption energy of C atoms on the surface, and the amount of electron transfer from C to the surface atoms, as a function of number of Pd/Au atoms in the surface are depicted in Figure 7.6. There is a large fluctuation in the amount of electron transfer from C atoms to the adjacent atoms of the surface. This might be due to the composition of Pd/Au in our slab which is not changing consistently. Therefore, there is not a clear correlation found between the amount of charge transfer and the adsorption energies.

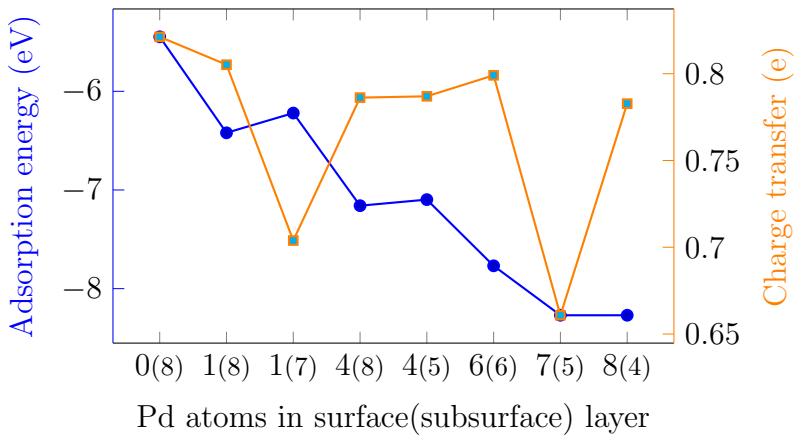

Figure 7.6.: Correlation between the adsorption energies of C atoms and the charge transfer atoms adjacent to the adsorbed C atom with respect to number of Pd atoms on the surface(subsurface).

The adsorption energies of C atoms on the $Pd_3Au(100)$ surface and the partial charge of the adsorbed C atom with respect to number of Pd atoms in the surface(subsurface) are depicted in Figure 7.7. The C atom has decreasing charge on it due to the increased number of Pd atoms in the surface and subsurface.

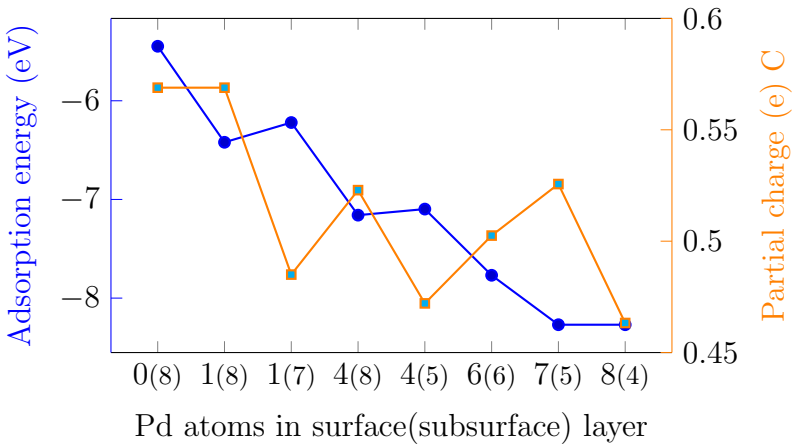

Figure 7.7.: Correlation between the adsorption energies of C atoms on the $Pd_3Au(100)$ surface and the partial charge of the carbon atom with respect to number of Pd atoms on the surface.

To better illustrate how the electron density changes when a C atom is adsorbed, isosurfaces are made which are contour plots of the electron density. The distribution of the electron density on C atom and the adjacent atoms illustrate the contribution from each atom on the $Pd_3Au(100)$ surface to the adsorption of C atom. Electron density isosurfaces displays a specified fraction of its electron probability density. This fraction is specified in per volume where the displayed volume is determined by the Bohr radius, which is defined as the maxima of finding an electron around a nuclei [72].

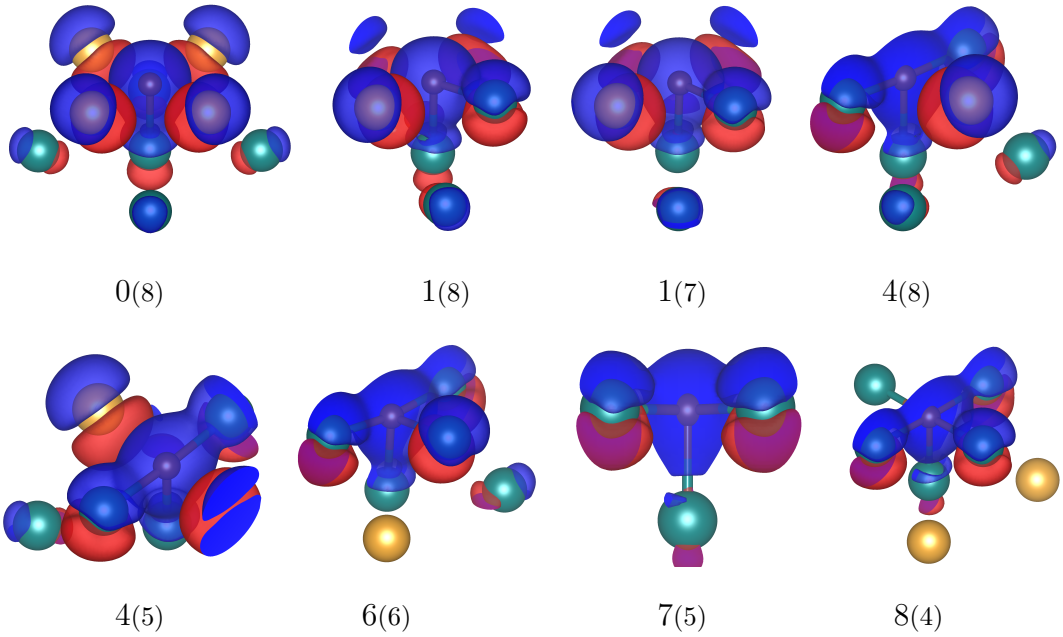

Figure 7.8.: Charge density difference iso-surfaces of C atom and the adjacent atoms on different configurations of $Pd_3Au(100)$ surface. Blue areas are characterized by an abundance of electrons. Red areas are characterized by a relative absence of electrons. Isosurface level: 0.02 a_0^{-3} (a_0: Bohr radius).

7.4. Density of states

To gain a more detailed insight of the electronic structure that play an important role in the adsorption of C atom on the $Pd_3Au(100)$ surface, we investigated the density of states projected on elements of the Alloy surface. This analysis will help for example to understand how metal d bands changes in different alloy composition, and also their effects on adsorption properties of C atoms.

Bulk and surface DOS

The d bands of monometallic Pd and Au surfaces and their corresponding bulk system are presented in Figure 7.9. The more noble Au have filled d bands resulting in a d band well below the Fermi energy ($E = E_F = 0$). Pd on the other hand have d band extending above the Fermi energy since it is not filled and is less crowded with electrons than Au. The more narrow d-bands for the surface atoms is caused by fewer neighbours, and thus a less filled band. This also shifts the d band center further up towards the Fermi energy, which shows that surface atoms are more reactive than atoms residing in the bulk. Here ϵ_d is found for surface atoms to be -1.48 eV for Pd(100), with -1.83 eV as reported value for Pd(111) and -2.99 eV for Au(100) with -3.56 as reported value for Au(111) [141]. The lower value found here can be explained with the less dense surface packing, whereas Ruban et al. [141] calculated the most close packed. Large discrepancies between the different terminations have been reported in the literature for various Pt terminations [142], and are consistent with the values reported here.

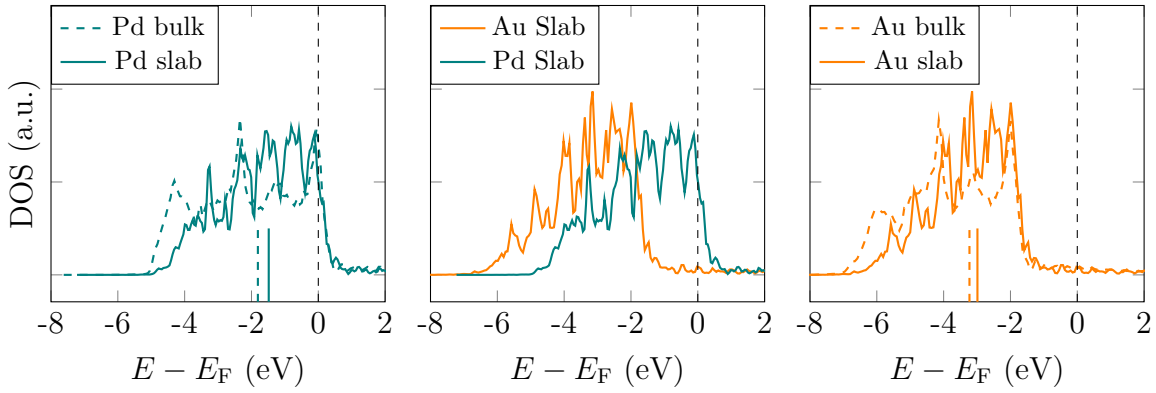

Figure 7.9.: Projected d bands for monometallic Pd and Au surface and bulk systems. For Pd ϵ_d is -1.81 eV for bulk atoms and -1.48 eV for surface atoms. For Au ϵ_d is -3.23 eV for bulk atoms and -2.99 eV for surface atoms. Vertical rods represent the individual bands' center, dashed and solid lines are projected d band DOS for bulk and surface, respectively.

A gradual trend is seen in Figure 7.10a-h where the filling of the states increases closer to the Fermi energy with an increasing amount of Pd atoms in the surface, which indicates that the surface is more reactive with an increasing amount of Pd in it. The lattice of the Pd_3Au alloy is slightly larger than that of monometallic Pd while it is considerably smaller than for monometallic Au. Strain in transition metal surfaces causes the d-states at neighbouring atoms to either increase or decrease, changing the width of the d-bands. And it is generally found that the d bands move in energy to maintain a constant filling. Compressive or tensile strain therefore leads to downshifts and upshifts of the d band centers, respectively [77]. Looking at the Pd terminated surface without adsorbate in Figure 7.10h, the d band center is located further up than that of a monometallic Pd slab which is in agreement with the d band model where tensile stress should indeed lead to an upshift of the d band center. This is a result of introducing Au and thus expanding the lattice. On the other hand, with a Au terminated surface, the d band center is close to that of monometallic Au. There is also an indirect effect contributing to the position of the d band center, which is caused by the hybridization of the d states between the topmost atoms and the atoms in the second layer [77]. This can explain why the Au terminated surface is not shifted further down than the pure Au surface as the Au atoms on the Pd_3Au surface are in compressive strain.

It is interesting to note that just 1 ML of Au on top of Pd causes the surface to become very Au-like from an electronic point of view. This will have consequences for any reaction where Pd_3Au is employed. Since Au is the most favourable termination in vacuum for this system, too little reactive species available to bond to Pd can fill the surface with Au, causing a significant reduction of the system's reactivity.

Introducing carbon onto the surface also has a clear effect on the electronic structure, displayed in Figure 7.10a'-h'. The different terminations have varying position of the bonding states and as the d band shifts up in energy, which leads to a stronger bond. The most Pd rich terminations, Figure 7.10g' and h' have both one single bonding contribution since all nearest neighbours are Pd atoms. When there are one or more Au atoms as nearest neighbours, the bonding state contribution is shifted further down in energy, which should result in a weaker bond according to the d band model [1].

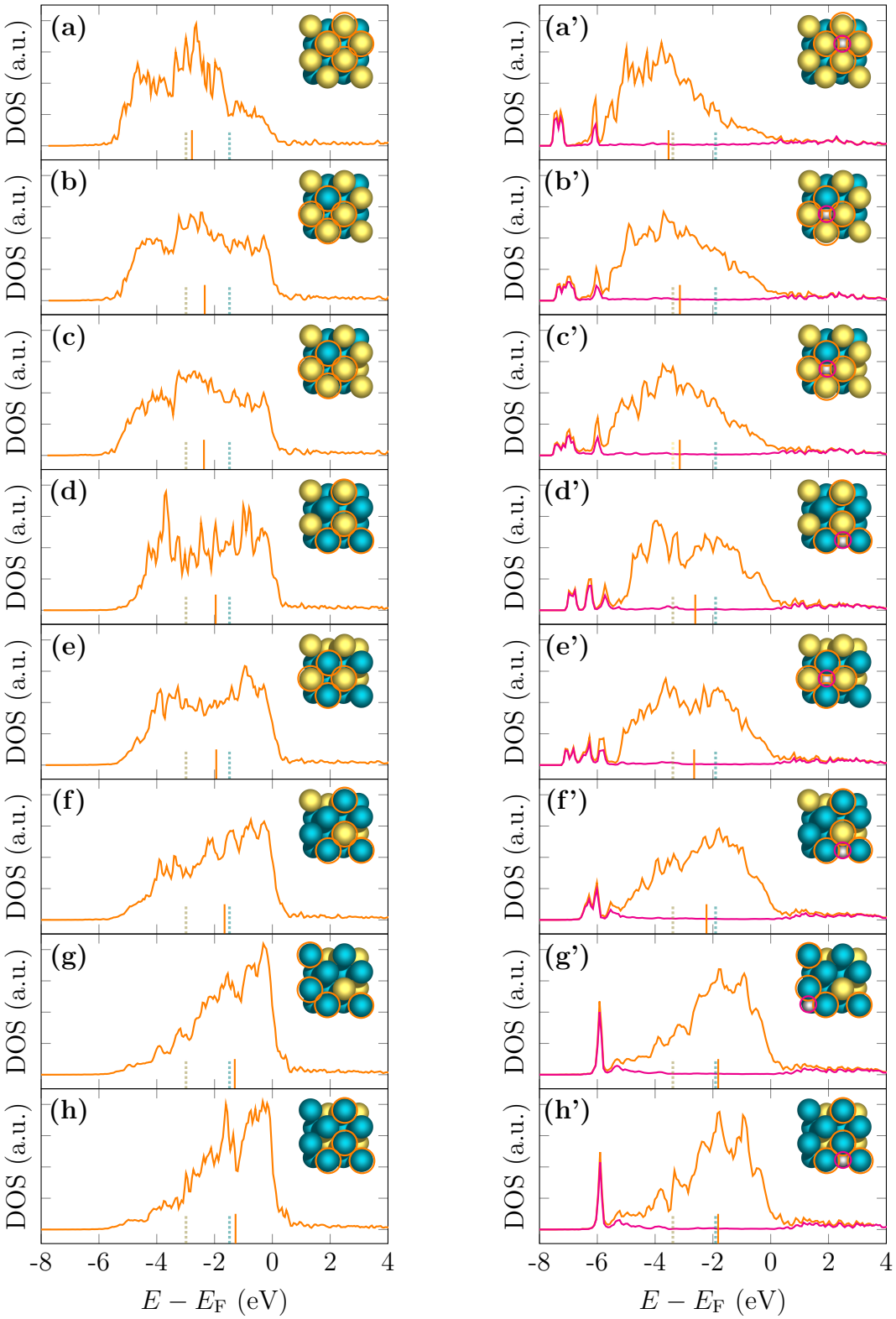

Figure 7.10.: Projected d bands of surface atoms adjacent to the adsorption site (encircled) before and after adsorption of C on the various surfaces investigated. Dashed vertical rods represents ϵ_d of monometallic slabs of Pd (blue) and Au (gray) while solid rods are the center of the total d band DOS of encircled atoms. The projected carbon p-DOS is included as a purple line.

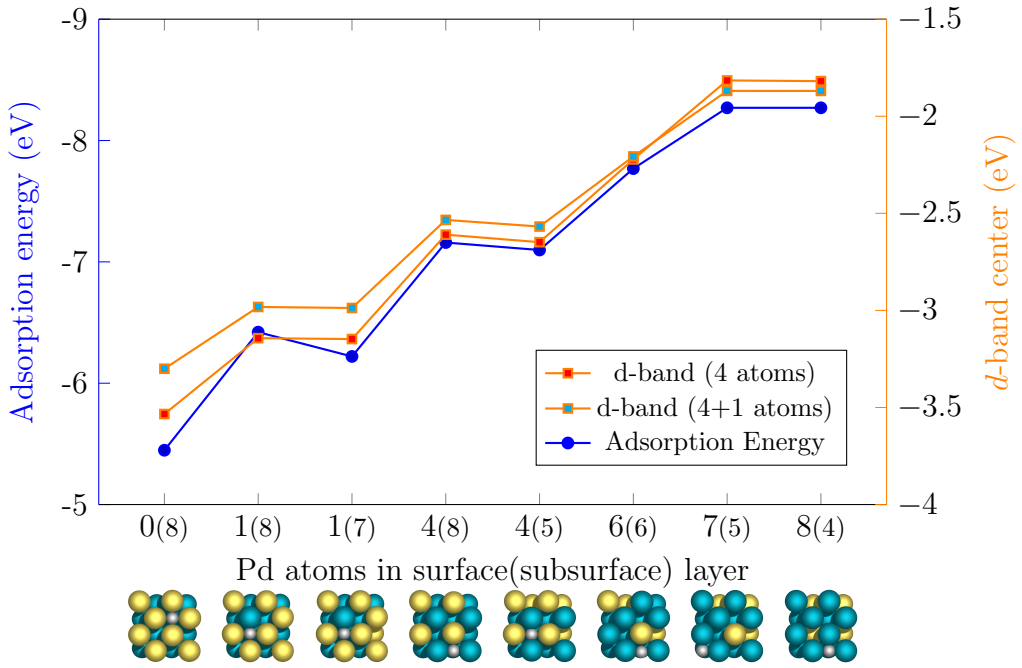

Figure 7.11.: Adsorption energy of the most favourable hollow sites plotted with the d band centers of the calculated slabs. A clear trend is seen that as the d band shifts up in energy, closer to the Fermi energy, the adsorption energy increases which will result in a stronger bond. The two different d band lines (orange) represents the surface nearest neighbours (4 atoms) and the surface nearest neighbours including the atom below the carbon (5 atoms) after adsorption.

In Figure 7.11, the correlation between the adsorption energy of C atoms on the most favourable adsorption sites, hollow, and the d band center of the selected atoms on the calculated slabs, after adsorption of carbon, are plotted with respect to number of Pd atoms in the surface(subsurface) of $Pd_3Au(100)$. A clear trend is seen where an upshift in the d states should lead to a strengthening of the bonding of the adsorbate to the transition metal surface. The reason for the increasing adsorption energy with an increasing amount of Pd atoms in the surface is that Pd has a d band center further up which gives rise to a large bonding contribution closer to the Fermi energy than Au. This is the cause for the increased adsorption energy and also a fingerprint on the reactivity of the $Pd_3Au(100)$ surface.

A larger amount of Pd atoms in the surface will increase the reactivity towards carbon and other adsorbing species [33, 77, 123, 124, 143]. The d-band center for the Au terminated surface is -2.78 eV before and -3.53 eV after adsorption of carbon while for the Pd terminated surface it is -1.27 eV before and -1.82 eV after adsorption. The shifts are -0.75 eV and -0.55 eV for Au and Pd terminated surfaces, respectively. A significantly

larger shift for the Au terminated surface. This could help in explaining why adsorption of more atoms is less favourable for a Au terminated surface as 1 ML carbon coverage was found to be unstable for this termination. This will have implications for bonding of more atoms to surface, where a Pd rich will be able to adsorb more atoms than a Au rich surface.

Chapter 8.

Experimental results

Presented in this chapter are the results obtained from experimental investigations of the $Pd_3Au(100)$ system. Presented first are results obtained from hydrogenation of the sample using the reaction cell, Figure 5.4, and characterized using a in-house XPS system with a fixed photon energy. Next follows results obtained from oxidation of the $Pd_3Au(100)$ surface, with results obtained from HRXPS using synchrotron radiation presented first and in-house investigations with LEED/STM presented thereafter.

8.1. Hydrogenation of the $Pd_3Au(100)$ crystal

By exposing the $Pd_3Au(100)$ single crystal to H_2 gas and subsequently measure it, insight into the segregation properties of Au and Pd and how temperature affect hydrogenation of residual carbon can be obtained. Investigating how Pd, Au and C reacts to H at different temperatures is important in order to better understand how the surface dynamically changes on a Pd-based membrane under relevant operating conditions. Hydrogen interacts with palladium, but spectroscopic methods have a very low sensitivity towards H and thus the interaction has to be deduced from the altered shape of the various elements present in the sample [144].

As mentioned in the Experimental part, but repeated here for clarity, all spectra in this section were acquired using a monochromatic Al kα X-ray source with excitation energy of 1486.7 eV. A charge neutraliser was also used to avoid build up of charge on the sample since it was mounted on an insulating sample holder. This caused a large shift to lower binding energies and to shift the peaks back, the component belonging to bulk Pd was used as reference.

Figure 8.1 shows the evolution of Pd $3d_{5/2}$, C 1s and Au $4f_{7/2}$ obtained after exposure to $2 \cdot 10^{-2}$ bar H_2 for 2 minutes at different temperatures. The Pd $3d_{5/2}$ spectra acquired after H_2 exposure at room temperature (RT) and 100 °C, does not display any

large change in shape, but they have lower intensity compared with spectra acquired after exposure at higher temperature. The Pd $3d_{5/2}$ peaks measured after exposure at 300 and 400 °C have a larger contribution from the component on the higher binding energy side. This may indicate that hydrogen has interacted chemically with palladium. Assuming that the treatment saturated Pd with hydrogen, these shifts can be caused by the hydrogenation of C, bringing the surface closer to the clean metallic state [145]. Chemical shifts of Pd $3d_{5/2}$ due to hydrogen exposure has been reported as +0.1 eV [146] ($Pd_{75}Ag_{25}$, polycrystalline membrane) and +0.15 eV [147] (Pd foil). From high-pressure XPS measurements on Pd(111), the measured shift due to hydride formation in-situ has been reported as +0.2 eV [144]. If a hydride phase was measured in this experiment, the shape of Pd $3d_{5/2}$ should have been altered and become distinctly more symmetric [144]. This is not visible here and thus, no hydride phase is measured, only the effect of hydrogenation of residual carbon which affects the shape and segregation of Pd. Pd-H is unstable upon evacuation and will withdraw from the Pd lattice provided sufficient temperature to migrate [144]. The prolonged time at elevated temperature in Ar causes rapid out diffusion of the hydrogen in the lattice.

Core levels of Pd $3d_{5/2}$ also includes Au $4d_{5/2}$, which in this report has been fitted using a the same lineshape as Au $4d_{5/2}$ in a sample of pure Au. The area of this component is 50 % larger than the Au $4d_{3/2}$, so by measuring this peak in the Pd_3Au sample, an approximate area and shape of the Au $4d_{5/2}$ component has been found. This is included as a yellow component on the lower binding energy side. As explained in the Theory chapter; in all core-level spectra of clean Pd 3d there is a small "hump" on the high energy side of the peak, which is not properly modelled by the asymmetry parameter and an additional component has to be added. It is however at this position that most adsorbates also induces a core level shift, which causes the problem to disappear [68]. At 300 °C Pd $3d_{5/2}$ has a small shoulder at higher binding energy. Albeit small, there is no visible change in the CO components in the relevant C 1s spectrum, so the change might be attributed to more metallic Pd measured.

Carbon is most likely found in various forms in the surface region. In Figure 8.1 there are two different components attributed to the C 1s spectra. One at 286.0 eV which is thought to originate from oxygen-containing carbon (e.g. CO) while the main peak, located at 284.7 eV, is from various carbon species such as C-Pd, C-C and C-H. The exact identification of these species is not unambiguous, but according to the literature they correspond to (chain) carbon that is likely attached by several bonds to the metal, to graphitic carbon and to hydrogen-containing aliphatic carbon [144, 145, 148]. For C 1s, there is an increasing amount of CO and carbon-species after exposure and heating

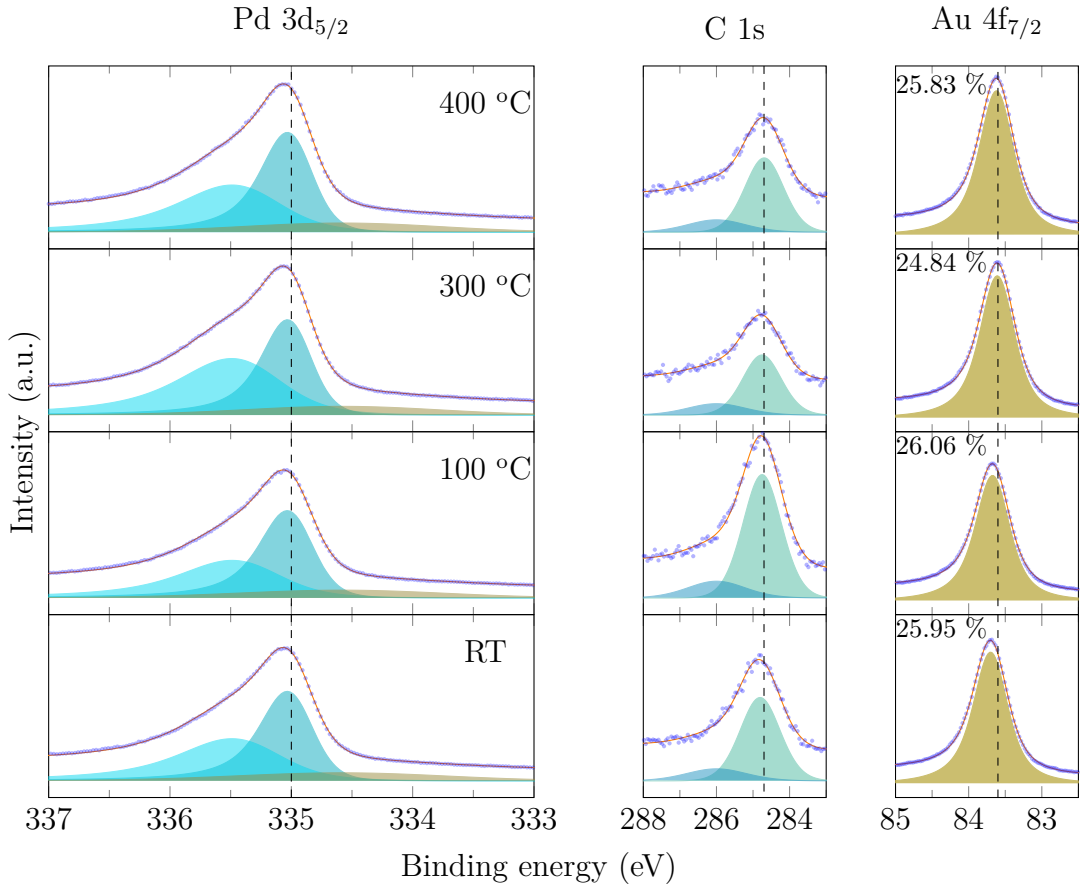

Figure 8.1.: Core level spectra (from left to right) of Pd $3d_{5/2}$, C 1*s* and Au $4f_{7/2}$ obtained after H_2 exposure of $2 \cdot 10^{-2}$ bar for 2 minutes at different temperatures. Dashed lines at 335 eV, 284.7 eV and 83.6 eV. The calculated atomic concentration of Au is written in the top left corner of each Au $4f_{7/2}$ spectrum. Intensities given in arbitrary units and intensity scales differ between individual core levels. Yellow component in Pd $3d_{5/2}$ belongs to Au $4d_{5/2}$. Excitation energy: 1486.6 eV.

to 100 °C. This might be caused by the higher temperature, which allows more carbon to migrate to the surface. Measurements performed after exposure to H_2 gas at 300 °C, indicates that hydrogenation of residual carbon found on the surface is occurring. The lowest concentration of carbon is measured after exposing to H_2 at 300 °C while the measured carbon increases at 400 °C. The increased concentration of carbon found after exposing at 400 °C is thought to be caused by the slow cooling rate of the reaction cell, which allows for carbon to migrate to the surface in the atmosphere containing only Ar. Another contributing factor could be caused by a too high temperature for H_2 to adsorb onto the surface at this temperature. This will cause H_2 to bond weaker and thus affecting the coverage on the surface whereas less hydrogenation of residual carbon will occur.

Au $4f_{7/2}$ has the same shape for all measurement, indicating that Au is found in the same chemical state and is not changing due to the H_2 exposure. However, the different temperatures and the introduction of gas which readily bonds to Pd has an effect on the measured intensity. The atomic concentration of Au was determined to be in the range between 24 and 26 % for all measurements, thus no large change in the composition volume sampled due to H_2 exposure. The uncertainty in the calculated concentrations are of the same size as the changes themselves although the calculations were performed as consistent as possible. However, the lowest concentration of Au is found after the exposure at 300 °C which also saw greatest reduction of residual carbon on the surface. This could indicate that there is a preferential segregation of Pd to the surface under these reaction conditions. In Figure 8.1 Au $4f_{7/2}$ seems to have a small shift to lower binding energy with higher temperature, but this shift is within the error margins caused by the use of the charge neutralizer, and therefore not discussed further. Using high energy X-rays from an Al anode causes the photons to have large penetration depth, such that the bulk is always giving a large contribution to the spectrum and one is not able to distinguish between contributions coming from the surface and bulk. This is the reason why synchrotron light is applied.

8.2. Oxidation of the $Pd_3Au(100)$ surface

8.2.1. High-resolution XPS

High resolution XPS measurements of the clean and oxidized surface of Pd3Au(100) were performed to elucidate the changes in the surface composition upon oxidation and temperature increase. The HRXPS measurements were aquired at the MATLINE beamline of the ASTRD2 synchrotron at Aarhus University, Denmark. The use of synhcrotron radiation allows for the tuning of the photon energy to become more surface sensitive. This was done in order to investigate the properties of Pd_3Au alloys on CO oxidation and formation of the $(\sqrt{5} \times \sqrt{5})$R 27° surface oxide was attempted and its contribution to the measured signal decomposed. All spectra were acquired with normal (0°) and grazing (60°) emission angles. The photon energy used for each core level is stated in the respective spectra. Exposure of the surface to $5 \cdot 10^{-5}$ mbar of O_2 across a temperature interval from 350 °C to 280 °C results in the preferential segregation of Pd to the surface as reported by Strømsheim et al. [7]. This preferential segregation of Pd atoms to the surface is because Pd is more reactive to adsorbates and readily form bonds due to its electronic structure [43, 121, 123, 124]. Since oxygen is introduced in relatively large amounts, oxidation of residual carbon in the surface region should occur and decrease its contribution to the spectra.

Pd 3d

Presented first are spectra of Pd 3d after oxidation and subsequent heating up to 500 °C. Both normal (left) and grazing emission (right) are shown in Figure 8.2. In all spectra, Pd $3d_{3/2}$ and $_{5/2}$ are presented because Pd $3d_{5/2}$ also contains contribution from Au $4d_{5/2}$ at 335 eV. Due to a large difference in the cross-sections at 390 eV (1.5 versus 0.25 [149]), it has not been included as a dedicated component and is combined with the Pd $3d_{5/2}$ bulk component at binding energy 334.8 eV. The Pd $3d_{3/2}$ peak is distinctly less steep on the higher energy side than Pd $3d_{5/2}$, which is thought to be caused by photoelectron diffraction effects which enhances the surface emission at excitation energies around 390 to 400 eV for Pd [150]. This broadening of the Pd $3d_{3/2}$ peak causes the respective components to be shifter further apart than for Pd $3d_{5/2}$.

After oxidation (bottom), both peaks are fitted using three components since the peak is distinctly more broad than from measurements obtained on the clean surface. The relatively high base pressure ($5 \cdot 10^{-9}$ mbar) contained a significant contribution from CO. After oxidation, CO may be present on the surface, which will result in a

contribution at BE 335.4 eV for Pd $3d_{5/2}$ [7]. CO has been reported by Languille et al. [116] to adsorb on-top (341.3 eV) and in bridge sites (340.8 eV) on AuPd(110). Here, the author reported values for Pd $3d_{3/2}$ to avoid any contribution from Au 4d. However, these components can also be attributed to the $(\sqrt{5}\times\sqrt{5})$R 27° surface oxide [151], which will result in two additional components to the measured spectra. These components are attributed to two-fold and four-fold oxygen coordinated Pd atoms found at 335.6 and 336.2 eV, respectively. This is at 0.3 and 0.2 eV higher binding energy than reported by Strømsheim et al. [7] for $Pd_3Au(100)$ and 0.17 and 0.08 eV higher binding energy than by Walle et al. [2] for $Pd_{75}Ag_{25}(100)$. Both these investigations used photon energies of 400 eV, and the additional shift might be attributed to the decreased photon energy used here which broadens the peak due to diffraction effects on the surface. The contribution from chemisorbed O is in the same area as two-fold O coordinated Pd atoms [2], but one is not able to distinguish between them. The increased surface contribution caused by tilting the sample is visible, in particular from the spectra acquired after the oxidation attempts. The Pd $3d_{5/2}$ core level recorded at grazing emission is distinctly more broad, and with a larger contribution from the components attributed to two-fold and four-fold oxygen coordinated Pd atoms, compared to the recorded spectrum at normal emission.

Surface core level shifts in general reflect an initial state change in the electrostatic potential in the atomic core region. For Au, these shifts can be partly due to s-d re-hybridization effects at the surface, resulting in a shift of the 4f levels towards the Fermi level [152]. CLS due to alloying has been observed for various Pd-Au alloys, and is negative for both Pd and Au [153]. The reason for both peaks having a negative shift is due to hybridization of Pd d-bands with the Au bands.

After annealing to 200 °C (row 2 from bottom), there is a significant reduction of the amount of surface oxide found on the surface. However, the component for two-fold oxygen coordinated Pd atoms (or chemisorbed O) is not visible from normal emission, but it has a small contribution from grazing emission. These components can also be attributed to CO bonded to the surface. A new oxidation procedure after annealing to 200 °C (row 3 from bottom) returns the surface oxide, albeit with a lower detected intensity and slightly broader peaks. Annealing to 300 °C causes desorption of most oxide on the surface, but there is still a large contribution on the higher energy side at 335.6 eV, which could be attributed to more Pd atoms available in the surface where CO or O can bond. Finally, annealing to 500 °C, results in the main contribution from the measured Pd signal being bulk Pd 3d.

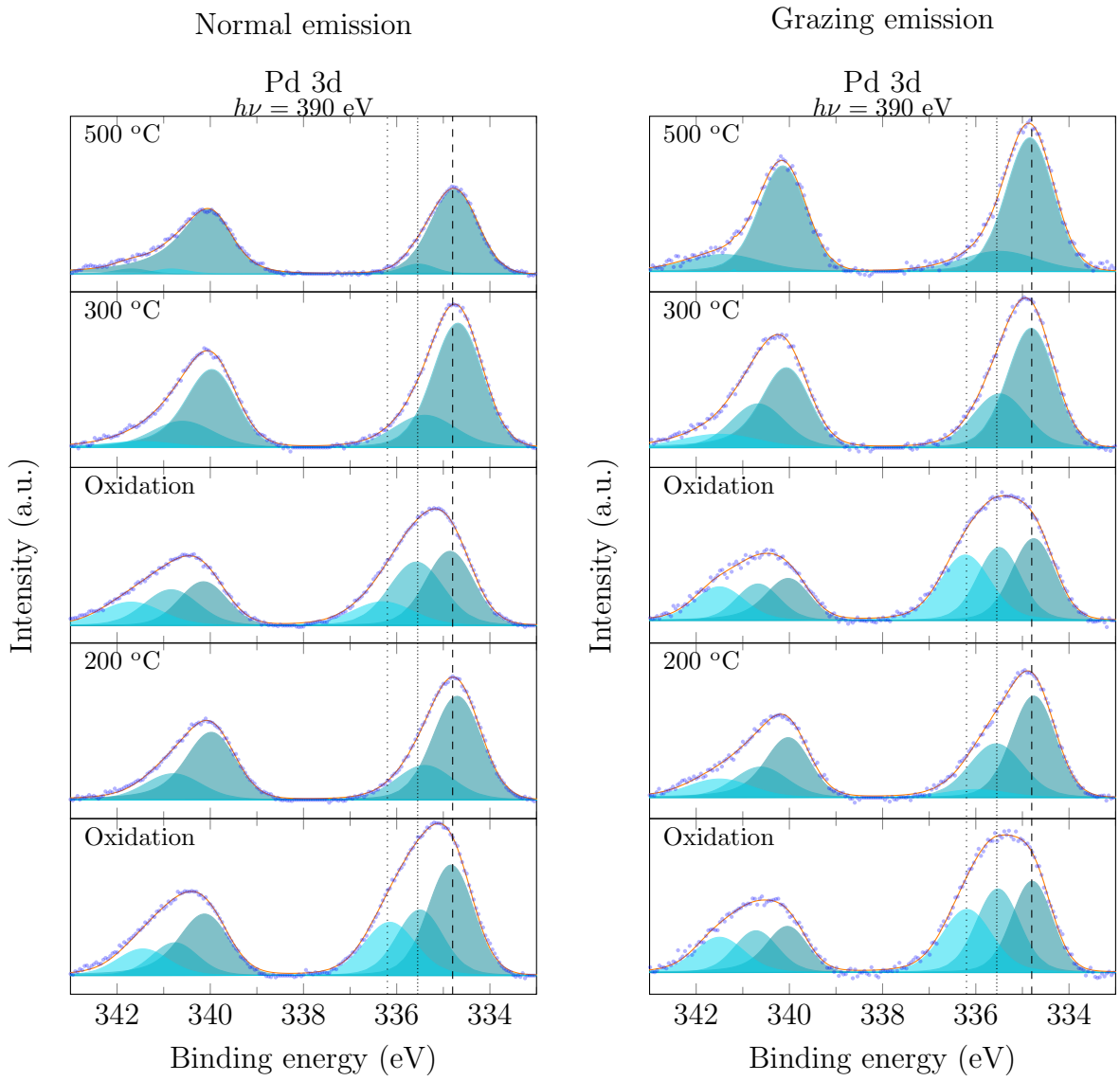

Figure 8.2.: Pd 3d spectra obtained with normal and grazing emission of the oxidized $Pd_3Au(100)$ surface with subsequent heating to the indicated temperatures. All spectra acquired at temperatures below 100 °C. Dashed line at 334.8 eV, densely dotted line at 335.6 eV belong to two-fold, and dotted line at 336.2 eV belong to four-fold oxygen coordinated Pd atoms. The oxidation procedure is mentioned in the introduction to this section, and described in Section 5.3. Intensities given in arbitrary units and with the same intensity scaling for the respective emission angle.

C 1s and Au $4f_{7/2}$

Displayed in Figure 8.3 are the spectra of Au $4f_{7/2}$ and C 1s obtained for normal emission (left) and grazing emission (right) after oxidation and subsequent heating up to 500 °C.

During oxidation, oxygen will bond to and cause preferential segregation of Pd to the surface [123, 124], in a (2×2) pattern and/or form a surface oxide. This results in fewer sites for CO to bond and a lower signal detected to the component at 286 eV (blue). Subsequently heating to 200 °C can cause oxidation of carbon with the O atoms on the surface. The signal from C 1s is poor, especially from grazing emisson, but there is less carbon in C-C or C-Pd form (green) after heating to 200 °C (row 2 from bottom). The increased amount of adsorbed CO may be attributed to less chemisorbed oxygen/surface oxide present on the surface, allowing more CO to bond to surface it. This implies that the surface still contains many Pd sites where CO can bond.

Annealing to 300 °C (row 4 from bottom) results in a reduction in the measured CO contribution in comparison to annealing to 200 °C (row 2 from bottom). This corresponds to the larger contribution from Au in the surface at 300 °C relative to 200 °C, as observed in the Au $4f_{7/2}$ core levels at these temperatures. If the composition of the surface is mainly comprised of Au, CO has fewer sites to bond to and will not give a large contribution to the measured signal. After annealing to 500 °C, the component belonging to CO (blue) is found at 0.5 eV higher binding energy. This increase in binding energy for CO can be caused by fewer Pd atoms in the surface, causing CO to bond on-top and not in the more favourable bridge sites [116].

Considering the contribution from Au $4f_{7/2}$ after an oxidation procedure (bottom and third row), Au is only present in the bulk and can be fitted with only one component (brown). The peak is located at 83.4 eV, a negative shift of 0.6 eV from the pure Au peak at 84 eV. This is in agreement with the Au $4f_{7/2}$ binding energy values obtained with in-house XPS and other reported values for Au in Pd [7, 45, 154]. This is assumed to come from a strong hybridization effect between Au and Pd in the near surface region [116]. The measured signal is also larger for normal emission than for grazing, which corresponds to Au being found in the layers below the surface.

The recorded Au $4f_{7/2}$ core level after heating to 200 °C suggests that Au is situated in two different environments. The Au $4f_{7/2}$ peak has been decomposed into two different components. One component (brown) is thought to originate from Au embedded further down in the surface due to the segregation of Pd to the surface during the oxidation procedure. The yellow component may be ascribed to Au atoms which are located in the surface, at binding energy of 83.2 eV. The increase of the surface component is also larger with grazing emission. Although there is more Au in the surface after heating to

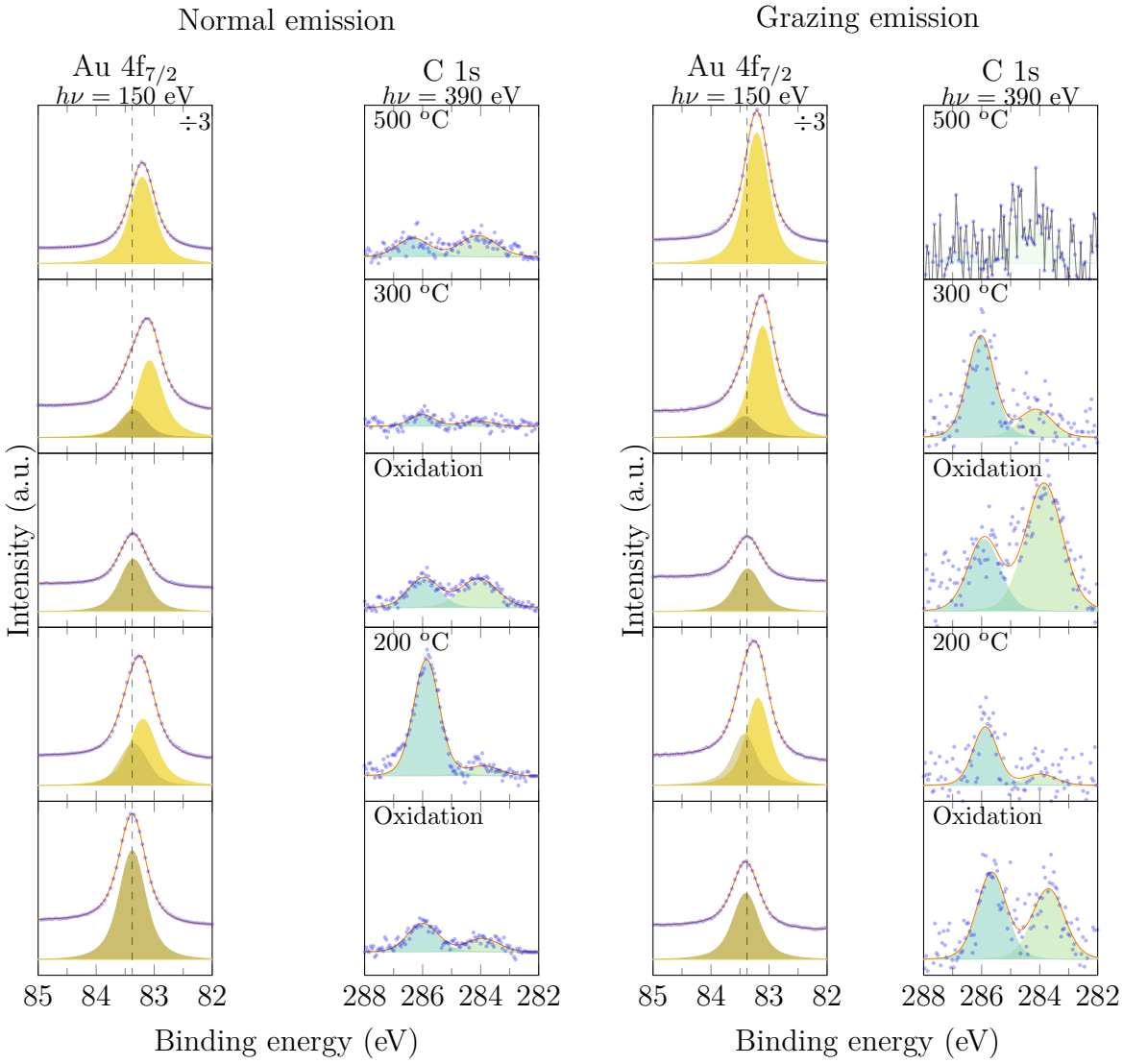

Figure 8.3.: XPS spectra of Au $4f_{7/2}$ and C 1s obtained for normal emission (left) and grazing emission (right) after oxidation with subsequent heating to the indicated temperatures. Dashed line at 83.4 eV. The oxidation procedure is mentioned in the introduction to this section, and described in Section 5.3. Intensities given in arbitrary units and intensity scales differ between individual core levels and emission angles and are scaled to their relative maximum value.

200 °C, a new oxidation procedure causes Au to be found in layers below since Pd is preferentially segregating to the surface under these conditions [123, 124].

After annealing to 300 °C Au $4f_{7/2}$ has a further shift down to approximately 83.1 eV for both emission angles. The increased intensity of Au $4f_{5/2}$ indicates Au enrichment of the surface, in accordance with what has been reported in several previous publications [7, 31, 115, 116, 134–137]. This component has a core level shift of -0.3 eV, due to the changed environment of Au atoms residing in the top-most layer. This surface core level shift of Au has been reported in the literature as -0.32 eV for Au(100) [152].

There is an increasing amount of Au in the surface when heating to 500 °C, and the component belonging to bulk Au is no longer present. Since the Au $4f_{5/2}$ contains contributions from mainly one component at 83.2 eV after heating to 500 °C, Au is assumed to be located mostly in the surface. This is consistent with the interpretation that difference in chemical environment has less effect on the measured CLS of Au atoms which will only have small CLS for various chemical environments. As one component yields a good fit, this could indicate that the surface consists of an Au-rich layer [45, 112, 116–118]. To better illustrate how Au changes as a result of the high O_2 pressure a collection of Au $4f_{7/2}$ measurements taken after the oxidation procedure is displayed in Figure 8.4 together with the acquired spectra after annealing at 300 and 500 °C.

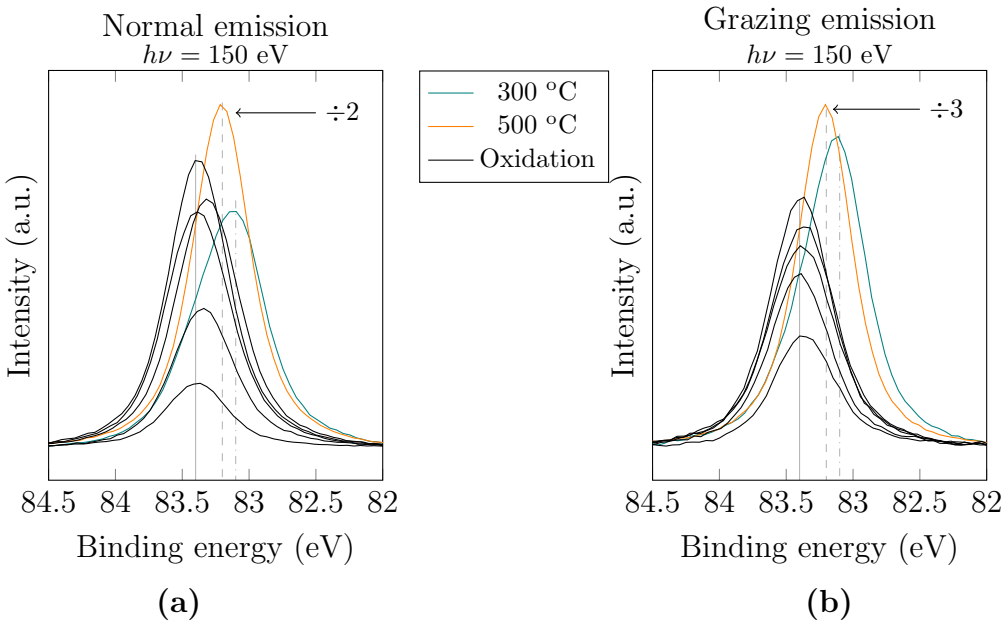

Figure 8.4.: XP spectra of Au $4f_{7/2}$ taken after various oxidation attempts (black) with the corresponding measurement done at 300 and 500 °C. Solid line at 83.4 eV, dashed line at 83.2 eV and dot dashed line at 83.1 eV. Intensities given in arbitrary units and intensity scales differ between normal and grazing emission. The measured intensity from Au after annealing to 500 °C is much larger than the other measurements and to ease in visualising peak positions, the orange lines have been divided by the factor displayed.

After the oxidation attempts, there is a shift to higher binding energies for Au $4f_{7/2}$ of 0.2 eV. The measured shift is 0.2 eV for the grazing emission, with a slightly larger variation in the size of the shift for the spectra recorded with normal emission. A shift to higher binding energy for Au $4f_{7/2}$ has been reported for AuPd(110) with increasing CO pressure, causing migration of Pd atoms to the surface [116]. After annealing to 300 °C Au $4f_{7/2}$ has a small shift to lower binding energies and is positioned at 83.1 eV, compared with 83.2 eV after annealing at 500 °C. The relative intensity is larger from grazing emission, indicating that the increase is caused by segregation to the surface. This might be related to the amount of bulk Pd measured, as it is found that at 300 °C there is more Pd in the surface than at 500 °C.

Valence band

Valence band spectra were also acquired, and a indication of a more Au rich surface should result in a shift of the centre towards higher binding energies, according to the calculations performed, seen in Figure 7.11. Figure 8.5 exhibits such a trend; when the annealing temperature is raised to 500 °C, there is more gold in the surface, thus a lower density of the states closest to the Fermi level and a downshift of the band centre, i.e. higher binding energy. This is in agreement with the calculations performed. Due to a relative large amount of CO and water present in the chamber and a large amount of oxygen found on the surface, the valence bands obtained directly after oxidation were not displaying this trend and had d band centres shifted to higher binding energies than for the valence band obtained after annealing to 300 and 500 °C. CO and O on these surfaces, results in a large bonding contribution at around 8 eV, which causes the centre to be shifted to higher binding energies and were therefore not included in the figure [96, 155]. The C 1s spectra from Figure 8.3 show the presence of CO and various forms of C on the surface after annealing to 300 and 500 °C, which will shift the d band center to higher binding energies. In addition, the photon energy used here gives rise to a large sp-contribution from the Pd-atoms [156], which means that one can not correlate the d band center values from these measurements with the values obtained from the calculations performed. Further information regarding experimentally determined d band centres can be consulted in recent publications by Okada et al. [157] and Kumara et al. [158] for CuAu and PtPd systems, respectively.

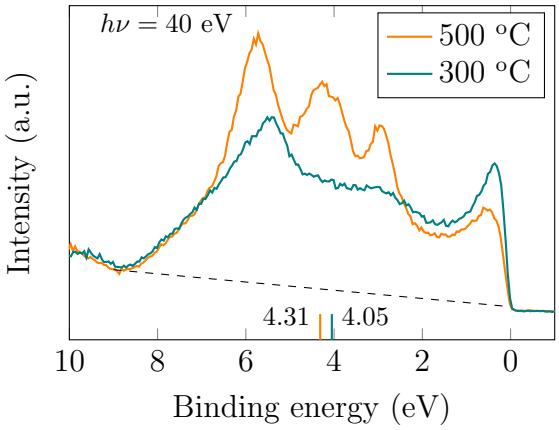

Figure 8.5.: Valence band obtained after annealing at 300 °C (blue) and 500 °C (orange) with grazing emission and photon energy of 40 eV. Dashed line represents the background that has been subtracted before integrating over the area under the curve.

The major effects of segregation of Au, where it is believed that Au is a thin film on

top of Pd [116], is the appearance of an additional structure at 4.2 eV caused by the Pd-Au interaction [156], which is not visible after annealing at 300 °C. From previous valence band studies in an excellent paper by Weissman-Wenocur et al. [156], clean Pd has structures stemming from the 4d valence electrons at 0.4, 1.5 and 3.8 eV for $h\nu = 40.8$ eV and a thick overlayer of Au has 5d electrons with peaks at 2.3, 3.1, 5.8 and 6.6. Au 5d electrons are spin-orbit split with a splitting of ~ 1.5 eV for isolated Au atoms [156, 159] and the spin-orbit split is decreasing when Au forms an alloy with Pd.

The peak originating from Au 5d and has a small change from 5.5 eV to 5.7 eV when annealing, which is an additional indication that the concentration of Au has increased in the surface [156].

8.2.2. STM and LEED

To investigate the average surface structure after oxidation, LEED was applied and STM was used to investigate small areas of the surface on a nanoscale. Formation of the $(\sqrt{5} \times \sqrt{5})$R27° surface oxide on the $Pd_3Au(100)$ single crystal was repeatedly achieved. A low-energy electron diffraction (LEED) image of it is visible in Figure 8.6. Rotation of the surface oxide can be either 27° or −27° with respect to the substrate direction, thus domains forming a 54° angle are present. Pd in Pd-Au alloys has been reported as more difficult to oxidize than pure Pd [31], which indicates that the temperature range over which oxidation occurs is more crucial to control. The pressure of O_2 used when forming the oxide on the surface of $Pd_{75}Ag_{25}(100)$ is considerably higher than what is used for the pure Pd(100) surface. Fernandes et al. [4] used O_2 pressure during oxidation of $5 \cdot 10^{-4}$ mbar and $5 \cdot 10^{-6}$ mbar for $Pd_{75}Ag_{25}(100)$ and Pd(100), respectively. Here, the pressure used is around $5 \cdot 10^{-5}$ mbar. The intensity from the spots appearing in the LEED is more diffuse and not as bright as those found on monometallic Pd(100) single crystals [2]. This coincides with the observed LEED pattern for $Pd_{75}Ag_{25}(100)$[2] and other reported findings for $Pd_3Au(100)$[7], which also has lower spot intensity. The interpretation that the surface oxide is not entirely covering the $Pd_3Au(100)$ surface is supported by these more diffuse LEED patterns.

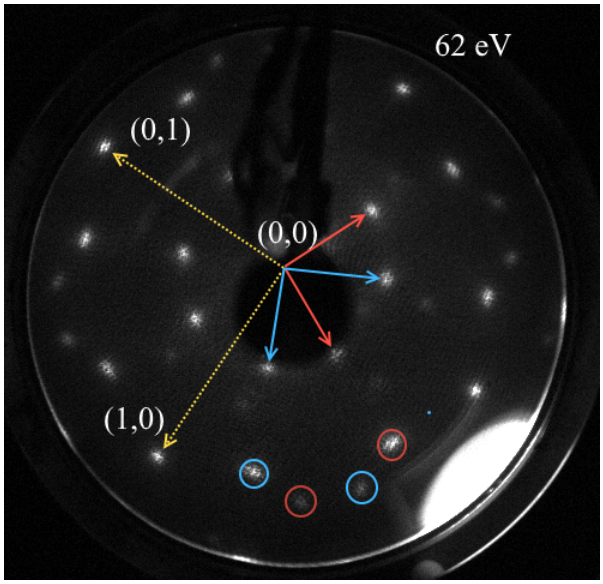

Figure 8.6.: LEED pattern showing the $(\sqrt{5} \times \sqrt{5})$R 27° surface oxide on the Pd_3Au single crystal. The unit cell of two domains is indicated and their reciprocal lattice vector has half the length of the PdO reciprocal lattice vector, marked here with circles. Electron energy indicated in top right corner.

The results obtained with STM are presented in the following paragraphs with the clean surface presented first and the oxidized surface thereafter. For each STM image presented, the bias applied (U) and the set tunnelling current (I_t) are stated. The clean surface of the $Pd_3Au(100)$ surface is displayed in Figure 8.7. Visible is a highly rough surface with depressions (black areas) with a depth in the range of 2.5-5 Å. This corresponds to one or two atomic layers in the $Pd_3Au(100)$ surface.

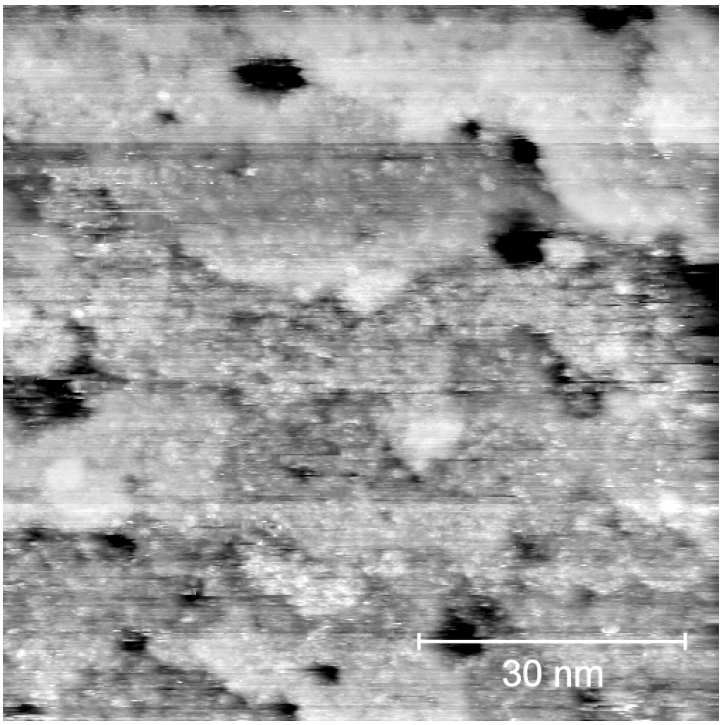

Figure 8.7.: STM image of the clean surface. Black areas are depressions that 2.5-5 Å deep. The surface contains many step edges and is rough. $U = 0.7$ V, $I_t = 1$ nA

After a partly unsuccessful oxidation attempt where the oxide pattern was very weak in LEED, the surface was covered with many depressions which were between 2 and 6 Å deep, illustrated in Figure 8.8. These features were found on most of the surface where STM was attempted, and the cause of these depressions is not known, but as the oxide pattern was weak in LEED, this might be considered an intermediate step of the oxide formation where the oxide has formed in small areas. Whether it's the depressions or the brighter surface that contains a layer of surface oxide is not known as imaging the surface with atomic resolution was not successful.

After oxidation of the surface, it is found to be rough with many step edges, as Figure 8.9 illustrates. There are also cluster-like formations present on all terraces. The cause of this rough surface is related to a shortened annealing time before oxidation. As Au

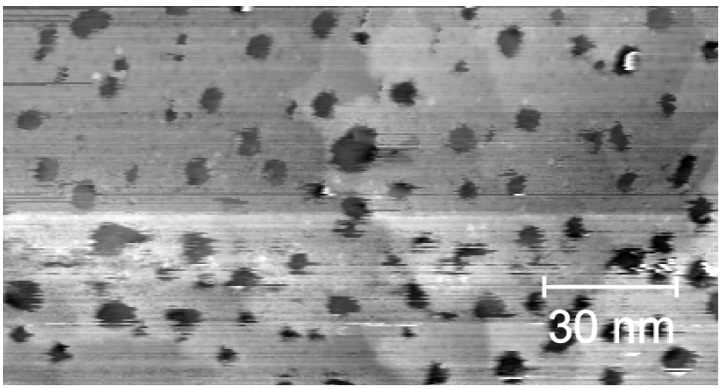

Figure 8.8.: STM image of the surface when the oxide pattern was weak in LEED. There are more depressions visible which are between 2-5 Å deep. $U = 1.1$ V, $I_t = 0.5$ nA

segregates to the surface when annealing in vacuum a shorter annealing time was used to smoothen the surface in order to have Pd atoms in the surface. A too long annealing time resulted in no formation of the surface oxide, which is believed to be caused by too high concentration of Au in the surface, and thus a lower reactivity towards O. It was attempted to anneal the sample at 500 °C beneath the oxygen doser for a prolonged period of time, but this did not smoothen the surface to a much larger extent, judging from the obtained STM images, than the usual 5-10 minute long annealing time before the oxidation procedure. The prolonged annealing time at higher temperatures with increased O_2 pressure also increased the time to pump down the chamber to a level where STM could be performed, and by this time, the surface oxide would have been partly reduced. This is believed to be caused by small amounts of CO and H_2 in the chamber that will reduce the surface oxide over time. This slow reduction was also verified with LEED. Some hours after the oxidation, the oxide pattern is considerably weaker than it was to begin with, before e.g. starting an STM session. Starting temperature for oxidation was for most attempts 350 °C, but lower temperatures were also attempted to narrow down the temperature range for oxide formation. It was confirmed that the formation will also occur at starting temperatures of 320 °C.

The lack of clusters in the STM images of the clean and the partly unsuccessful oxidation is evident judging from these very local examinations, compared with Figure 8.9 and 8.10. DFT has, on the other hand, predicted that Pd will not form clusters in a CO rich atmosphere [121], but we cannot rule out that some of these clusters seen are made from Pd. The clusters may also be impurities. However, they were not investigated systematically through imaging with a range of tunnelling currents and bias voltages, nor changing the bias.

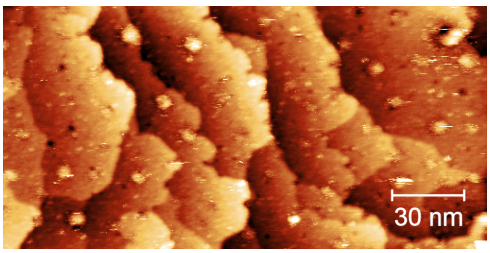

(a) $U = 1.4$ V, $I_t = 1$ nA

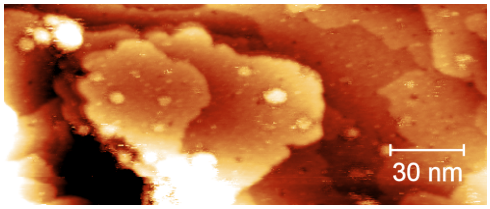

(b) $U = 1.4$ V, $I_t = 0.9$ nA

Figure 8.9.: STM images acquired after oxidation. **(a)** Terraces with clusters embedded on it. **(b)** Layered island-formation on the surface.

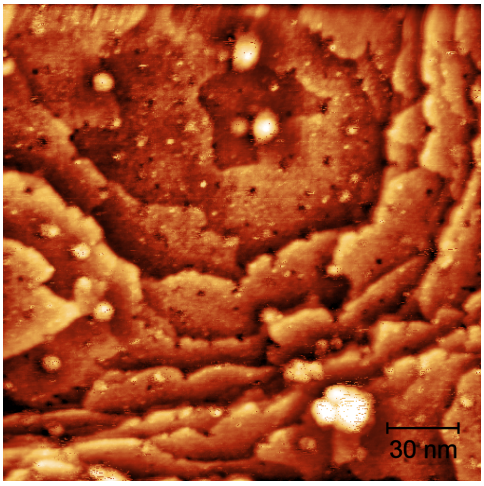

Figure 8.10.: STM image of Highly stepped surface after oxidation of the $Pd_3Au(100)$ surface. Black dots are here seen as depressions that are 1-2 Å deep. $U = 1.4$ V, $I_t = 0.9$ nA.

Visible in Figure 8.9a and 8.10 are small protrustions (black dots). These were found to be between 1 and 2 Å deep and are obtained with positive bias. From other studies of O_2 dissociation on metallic surfaces, individual O atoms appear as depressions on the surface [160–165]. Thus, the depressions seen here could be caused by adsorbed O atoms, but seeing that there are relatively few of them, this corresponds to a low O coverage which may indicate that there is low coverage of the surface oxide in the areas imaged. No atomically resolved image of the surface oxide was acquired, so we do not know where the oxide resides, its orientation and domain size.

Chapter 9.

Conclusion

The goal of this thesis was to characterize $Pd_3Au(100)$ as a catalytic model system for CO oxidation and hydrogenation through first-principle calculations and from experimental investigations by XPS, HRXPS, LEED and STM to better understand how the surface changes depending on the reaction conditions.

From first principle calculations, the Au-rich surface is found to be the most stable configuration in vacuum, and the stability decreases with increasing Pd coverage in the surface. However, this was shown to have implications on the adsorption energy of carbon, as carbon will preferentially adsorb to surfaces with a higher amount of Pd. For a Au covered surface, it is favourable for carbon to reside below the surface in a more Pd-rich environment. With an increasing C-coverage, it becomes more favourable for C to adsorb on a Pd-rich than Au-rich surface, with adsorption of 1 ML C on the Au-terminated surface being unstable.

The charge density difference analysis illustrated the distribution of the electron density between the adsorbed C atom and the adjacent atoms on the surface, and Pd (Au) atoms showed more (less) contribution to adsorption of C atoms on the $Pd_3Au(100)$ surface. The charge transfer analysis, however, did not show a clear trend with the adsorption energy of C atoms, a large fluctuations is found which might be due to the fact that the Pd/Au composition in our slabs was not changing consistently.

Analysis of DOS's indicated that a Au rich surface has a d band center close to that of pure Au, indicating that segregation of Au to the surface will cause the surface to become less reactive even if the layer is just one atomic layer thick. The reactivity of the surface was found to increase with increasing coverage of Pd in the surface as its d band center moves closer to the Fermi level. The d band center position and adsorption energy was found to correlate well, where the adsorption energy increases as the d band center moves up, closer to the Fermi level. This is in agreement with the d band model proposed by Hammer and Nørskov.

From characterization of the model system using XPS with a fixed photon energy, hydrogenation of the $Pd_3Au(100)$ crystal has a clear effect on the amount of residual carbon on the surface and it is found that the greatest effect of hydrogenation is at around 300 °C. At this temperature, the minimum concentration of Au was found, which implies that under these reaction conditions there is a preferential segregation of Pd to the surface. Hydrogenation also had an effect on Pd, where it is assumed that the Pd atoms in the surface region will be in a more pure metallic state after hydrogenation at 300 and 400 °C.

Applying synchrotron radiation to perform HRXPs, with a variable, and considerably lower photon energy, oxidation of the $Pd_3Au(100)$ surface causes preferential segregation of Pd to the surface, while Au is believed to be found below the surface. This is because segregation of Pd is more favourable under the high partial pressure of O_2 at elevated temperatures. Heating to 200 °C in vacuum causes reduction of the oxygen found on the surface, and causes Au to segregate to the surface, but considerable amount of it is still present in the subsurface layers. At 300 °C there is more segregation of Au to the surface, but still Au present in layers below the surface. After annealing to 500 °C, the Au measured is concentrated in the surface and no large contribution from Au in the bulk is found. From valence band investigations, the d band center shifts towards higher binding energies with an increasing amount of Au in the surface, in agreement with the calculations performed.

From investigations of the $Pd_3Au(100)$ surface with LEED after exposing to high partial pressures of O_2 at elevated temperatures, the formation of the Pd-$(\sqrt{5}\times\sqrt{5})$R27° surface oxide is confirmed. By subsequently investigating with STM, the local structure of the $Pd_3Au(100)$ surface is highly stepped with many clusters on the surface.

In conclusion, increasing coverage of Pd in the surface is important to have large reactivity towards adsorbing species. The amount of Pd in the surface is depending on the partial pressure of H_2 and O_2 and is very sensitive to the temperature applied.

Chapter 10.

Outlook

Further investigations of the $Pd_3Au(100)$ system should include calculations of adsorption energies for H_2, O_2 and CO. For investigations of the system as a hydrogen-permeable membrane it would be interesting to look into the diffusion properties of hydrogen, both from DFT and through experimental methods. Calculations of the surface oxide on various terminations of $Pd_3Au(100)$ will be insightful to learn more about what is the most favourable termination for the surface oxide and where Au is located in these structures.

Future work should also include smaller temperature steps of the hydrogenation reaction, preferably executed in-situ. One should also emphasize the use of lower photon energies to investigate how the valence band changes due to the different segregation properties of Au and Pd. This is also a method to correlate DFT calculations with experimental methods. The choice of photon energy should also be carefully selected to have most contribution from the d-orbitals of Au and Pd.

Continued work with the STM in imaging the atomic structure of the surface oxide to determine its local structure and domain size is emphasized. Using DFT one could also simulate STM images of the surface oxide to verify images obtained experimentally.

Bibliography

[1] B. Hammer, J. K. Norskov, *Nature* **1995**, *376*, 238–240.

[2] L. Walle, H. Grönbeck, V. Fernandes, S. Blomberg, M. Farstad, K. Schulte, J. Gustafson, J. Andersen, E. Lundgren, A. Borg, *Surface Science* **2012**, *606*, 1777–1782.

[3] V. Fernandes, J. Gustafson, M. Farstad, L. Walle, S. Blomberg, E. Lundgren, H. Venvik, A. Borg, *Applied Surface Science* **2014**, *313*, 794–803.

[4] V. Fernandes, J. Gustafson, I.-H. Svenum, M. Farstad, L. Walle, S. Blomberg, E. Lundgren, A. Borg, *Surface Science* **2014**, *621*, 31–39.

[5] V. Fernandes, M. V. D. Bossche, J. Knudsen, M. H. Farstad, J. Gustafson, H. J. Venvik, H. Grönbeck, A. Borg, *ACS Catalysis* **2016**, *6*, 4154–4161.

[6] L. Sørvik, Master thesis, Norwegian University of Science and Technology, Department of Chemical Engineering, **2015**.

[7] M. D. Strømsheim, J. Knudsen, M. H. Farstad, L. Sørvik, X. Guo, H. J. Venvik, A. Borg, *Topics in Catalysis* **2017**, *60*, 1439–1448.

[8] U. Diebold, S.-C. Li, M. Schmid, *Annual Review of Physical Chemistry* **2010**, *61*, 129–148.

[9] M. D. Ackermann, T. M. Pedersen, B. L. M. Hendriksen, O. Robach, S. C. Bobaru, I. Popa, C. Quiros, H. Kim, B. Hammer, S. Ferrer, J. W. M. Frenken, *Physical Review Letters* **2005**, *95*, 255505.

[10] B. L. M. Hendriksen, J. W. M. Frenken, *Physical Review Letters* **2002**, *89*, 46101.

[11] R. Toyoshima, M. Yoshida, Y. Monya, Y. Kousa, K. Suzuki, H. Abe, B. S. Mun, K. Mase, K. Amemiya, H. Kondoh, *Journal of Physical Chemistry C* **2012**, *116*, 18691–18697.

[12] S. Blomberg, M. J. Hoffmann, J. Gustafson, N. M. Martin, V. R. Fernandes, A. Borg, Z. Liu, R. Chang, S. Matera, K. Reuter, E. Lundgren, *Physical Review Letters* **2013**, *110*, 117601.

[13] J. Zhou, S. Blomberg, J. Gustafson, E. Lundgren, J. Zetterberg, *Catalysts* **2017**, *7*, 29.

[14] E. Lundgren, A. Mikkelsen, J. N. Andersen, G. Kresse, M. Schmid, P. Varga, *Journal of Physics: Condensed Matter* **2006**, *18*, R481–R499.

[15] J. Gustafson, R. Westerström, A. Mikkelsen, X. Torrelles, O. Balmes, N. Bovet, J. N. Andersen, C. J. Baddeley, E. Lundgren, *Physical Review B* **2008**, *78*, 045423.

[16] I. Chorkendorff, J. W. Niemantsverdriet in *Concepts of Modern Catalysis and Kinetics*, Wiley-VCH Verlag GmbH & Co. KGaA, Weinheim, FRG, **2005**, Chapter 5, pp. 167–214.

[17] M. Baerns, M. Holeňa, *Combinatorial Development of Solid Catalytic Materials*, Imperial College Press, **2009**.

[18] H. Over, *Science* **2000**, *287*, 1474–1476.

[19] B. Hendriksen, S. Bobaru, J. Frenken, *Surface Science* **2004**, *552*, 229–242.

[20] D. W. Goodman, *Chemical Reviews* **1995**, *95*, 523–536.

[21] J. F. Weaver, *Chemical Reviews* **2013**, *113*, 4164–4215.

[22] E. Laegsgaard, L. Österlund, P. Thostrup, P. B. Rasmussen, I. Stensgaard, F. Besenbacher, *Review of Scientific Instruments* **2001**, *72*, 3537–3542.

[23] E. Lundgren, C. Zhang, L. R. Merte, M. Shipilin, S. Blomberg, U. Hejral, J. Zhou, J. Zetterberg, J. Gustafson, *Accounts of Chemical Research* **2017**, *50*, 2326–2333.

[24] A. Stierle, N. Kasper, H. Dosch, E. Lundgren, J. Gustafson, A. Mikkelsen, J. N. Andersen, *The Journal of Chemical Physics* **2005**, *122*, 044706.

[25] M. Vannice, *Journal of Catalysis* **1979**, *56*, 236–248.

[26] M. V. Twigg, *Applied Catalysis B: Environmental* **2007**, *70*, 2–15.

[27] S. Tagliaferri, R. Köppel, A. Baiker, *Applied Catalysis B: Environmental* **1998**, *15*, 159–177.

[28] R. Farrauto, M. Hobson, T. Kennelly, E. Waterman, *Applied Catalysis A: General* **1992**, *81*, 227–237.

[29] D. Ciuparu, M. R. Lyubovsky, E. Altman, L. D. Pfefferle, A. Datye, *Catalysis Reviews* **2002**, *44*, 593–649.

[30] H. Henkel, W. Weber, Manufacture of hydrogen peroxide, **1914**.

[31] F. Gao, Y. Wang, D. W. Goodman, *The Journal of Physical Chemistry C* **2009**, *113*, 14993–15000.

[32] N. Lopez, J. K. Nørskov, *Journal of the American Chemical Society* **2002**, *124*, 11262–11263.

[33] B. Zhu, J. Creuze, C. Mottet, B. Legrand, H. Guesmi, *Journal of Physical Chemistry C* **2016**, *120*, 350–359.

[34] T. Graham, *Philosophical Transactions of the Royal Society of London* **1866**, *156*, 399–439.

[35] B. G. J. Grashoff, C. E. Pilkington, C. W. Corti, *Platinum Metals Review* **1983**, *27*, 157–169.

[36] M. L. Wise, J. P. Farr, I. R. Harris, *Journal of The Less-Common Metals* **1975**, *41*, 115–127.

[37] N. Al-Mufachi, N. Rees, R. Steinberger-Wilkens, *Renewable and Sustainable Energy Reviews* **2015**, *47*, 540–551.

[38] M. Prutton, *Introduction to Surface Physics*, Clarendon Press, **1994**, pp. 11–45, 49–106, 154–181.

[39] J. B. Hudson, *Surface science : an introduction*, Butterworth-Heinemann, **1998**, pp. 3–24, 89–98, 121–135, 175–183.

[40] K. W. Kolasinski, *Surface Science*, John Wiley & Sons, Ltd, Chichester, UK, **2012**, pp. 11–32, 57–106, 127–147, 207–246.

[41] D. Tománek, S. Mukherjee, V. Kumar, K. Bennemann, *Surface Science* **1982**, *114*, 11–22.

[42] L. C. a. V. D. Oetelaar, O. W. Nooij, S. Oerlemans, a. W. D. V. D. Gon, H. H. Brongersma, T. C. Thornton, P. O. Box, C. Ch, J. a. R. V. Veen, *J. Phys. Chem. B* **1998**, *5647*, 3445–3455.

[43] I.-H. Svenum, J. Herron, M. Mavrikakis, H. Venvik, *Catalysis Today* **2012**, *193*, 111–119.

[44] L. J. Lauhon, W. Ho, *Physical Review Letters* **2000**, *85*, 4566–4569.

[45] R. Toyoshima, N. Hiramatsu, M. Yoshida, K. Amemiya, K. Mase, B. S. Mun, H. Kondoh, *The Journal of Physical Chemistry C* **2016**, *120*, 416–421.

[46] R. P. Gupta, *Physical Review B* **1981**, *23*, 6265–6270.

[47] R. Smoluchowski, *Physical Review* **1941**, *60*, 661–674.

[48] E. A. Wood, *Journal of Applied Physics* **1964**, *35*, 1306–1312.

[49] N. Cabrera, N. F. Mott, *Reports on Progress in Physics* **1949**, *12*, 308.

[50] A. Atkinson, *Reviews of Modern Physics* **1985**, *57*, 437–470.

[51] P. Hofmann, *Surface Physics: An Introduction*, **2016**, pp. 134, 137.

[52] M. H. Farstad, PhD thesis, Norwegian University of Science and Technology, Department of Physics, **2014**.

[53] G. Binnig, H. Rohrer, C. Gerber, E. Weibel, *Physical Review Letters* **1982**, *49*, 57–61.

[54] G. Binnig, H. Rohrer, *Reviews of Modern Physics* **1987**, *59*, 615–625.

[55] J. Tersoff, D. R. Hamann, *Physical Review B* **1985**, *31*, 805–813.

[56] G. Bracco, B. Holst, *Surface Science Techniques*, (Eds.: G. Bracco, B. Holst), Springer Berlin Heidelberg, **2013**, p. 575.

[57] S. Hüfner, *Photoelectron Spectroscopy*, Springer Berlin Heidelberg, Berlin, Heidelberg, **1996**, pp. 61–107, 70–111, 173–209, 367–402.

[58] V. R. Fernandes, PhD thesis, Norwegian University of Science and Technology, Department of Physics, **2014**.

[59] S. Hüfner, S. Schmidt, F. Reinert, *Nuclear Instruments and Methods in Physics Research Section A: Accelerators Spectrometers Detectors and Associated Equipment* **2005**, *547*, 8–23.

[60] H. Lüth, *Solid Surfaces, Interfaces and Thin Films*, Springer Berlin Heidelberg, Berlin, Heidelberg, **2010**, pp. 539–543.

[61] S. Kohiki, *Spectrochimica Acta Part B: Atomic Spectroscopy* **1999**, *54*, 123–131.

[62] S. P. Kowalczyk, L. Ley, R. L. Martin, F. R. McFeely, D. A. Shirley, *Faraday Discussions of the Chemical Society* **1975**, *60*, 7.

[63] J. Moulder, W. Stickle, P. Sobol, B. K.D., J. Chastain, *Handbook of X-ray Photoelectron Spectroscopy: A Reference Book of Standard Spectra for Identification and Interpretation of XPS Data*, Physical Electronics Division, Perkin-Elmer Corporation, **1992**, pp. 118–119, 182–183.

[64] J. N. Andersen, M. Qvarford, R. Nyholm, S. L. Sorensen, C. Wigren, *Physical Review Letters* **1991**, *67*, 2822–2825.

[65] A. M. Stoneham, *Journal of Physics D: Applied Physics* **1972**, *5*, 430.

[66] L. Ballentine, *Reviews of Modern Physics* **1970**, *42*, 358–381.

[67] S. Doniach, M. Sunjic, *Journal of Physics C: Solid State Physics* **1970**, *3*, 285–291.

[68] M. Göthelid, H. von Schenck, J. Weissenrieder, B. Åkermark, A. Tkatchenko, M. Galván, *Surface Science* **2006**, *600*, 3093–3098.

[69] D. A. Shirley, *Physical Review B* **1972**, *5*, 4709–4714.

[70] S. Tougaard, *Surface and Interface Analysis* **1988**, *11*, 453–472.

[71] D. S. Sholl, J. A. Steckel, *Density Functional Theory*, John Wiley & Sons, Inc., Hoboken, NJ, USA, **2009**, pp. 1–233.

[72] P. P. P. W. Atkins, R. S. Friedman, *Molecular Quantum Mechanics*, **2011**.

[73] P. Hohenberg, W. Kohn, *Physical Review* **1964**, *136*, B864–B871.

[74] J. P. Perdew, K. Burke, M. Ernzerhof, *Physical Review Letters* **1996**, *77*, 3865–3868.

[75] J. P. Perdew, M. Ernzerhof, K. Burke, *The Journal of Chemical Physics* **1996**, *105*, 9982–9985.

[76] D. Santos-Carballal, A. Roldan, R. Grau-Crespo, N. H. de Leeuw, *Phys. Chem. Chem. Phys.* **2014**, *16*, 21082–21097.

[77] B. Hammer, J. Norskov, *Advances in Catalysis* **2000**, *45*, 71–129.

[78] A. Nilsson, L. G. Pettersson, J. K. Nørskov, *Chemical Bonding at Surfaces and Interfaces*, Elsevier, **2008**, p. 520.

[79] R. F. W. Bader, *Chemical Reviews* **1991**, *91*, 893–928.

[80] G. Henkelman, A. Arnaldsson, H. Jónsson, *Computational Materials Science* **2006**, *36*, 354–360.

[81] K. Momma, F. Izumi, *Journal of Applied Crystallography* **2008**, *41*, 653–658.

[82] G. Kresse, J. Furthmüller, *Computational Materials Science* **1996**, *6*, 15–50.

[83] G. Kresse, J. Furthmüller, *Physical Review B - Condensed Matter and Materials Physics* **1996**, *54*, 11169–11186.

[84] D. Joubert, G. Kresse, D. Joubert, *Physical Review B* **1999**, *59*, 1758–1775.

[85] A. H. Larsen, J. J. Mortensen, J. Blomqvist, I. E. Castelli, R. Christensen, M. Dułak, J. Friis, M. N. Groves, B. Hammer, C. Hargus, E. D. Hermes, P. C. Jennings, P. B. Jensen, J. Kermode, J. R. Kitchin, E. L. Kolsbjerg, J. Kubal, K. Kaasbjerg, S. Lysgaard, J. B. Maronsson, T. Maxson, T. Olsen, L. Pastewka, A. Peterson, C. Rostgaard, J. Schiøtz, O. Schütt, M. Strange, K. S. Thygesen, T. Vegge, L. Vilhelmsen, M. Walter, Z. Zeng, K. W. Jacobsen, *Journal of Physics: Condensed Matter* **2017**, *29*, 273002.

[86] S. P. Ong, W. D. Richards, A. Jain, G. Hautier, M. Kocher, S. Cholia, D. Gunter, V. L. Chevrier, K. A. Persson, G. Ceder, *Computational Materials Science* **2013**, *68*, 314–319.

[87] H. J. Monkhorst, J. D. Pack, *Physical Review B* **1976**, *13*, 5188–5192.

[88] J. D. Pack, H. J. Monkhorst, *Physical Review B* **1977**, *16*, 1748–1749.

[89] M. D. Strømsheim, PhD thesis, Norwegian University of Science and Technology, Department of Chemical Engineering, **2017**.

[90] C. T. Campbell, S. M. Valone, *Journal of Vacuum Science & Technology A: Vacuum Surfaces and Films* **1985**, *3*, 408–411.

[91] Omicron UHV STM 1, `http://www.scientaomicron.com/en/products/scanning-probe-microscopy`.

[92] RHK Technologies R9 SPM Control System, `http://www.rhk-tech.com/wp-content/uploads/2015/12/RHK-R9-BROCHURE-display.pdf`.

[93] J. Wintterlin, J. Wiechers, H. Brune, T. Gritsch, H. Höfer, R. J. Behm, *Physical Review Letters* **1989**, *62*, 59–62.

[94] Gwyddion, version 2.49, `http://gwyddion.net/`.

[95] Casa Software Ltd, *CasaXPS*, version 2.3.18, `http://www.casaxps.com/`, **2016**.

[96] L. Hilaire, P. Légaré, Y. Holl, G. Maire, *Surface Science* **1981**, *103*, 125–140.

[97] A. V. Ruban, H. L. Skriver, J. K. Nørskov, *Physical Review B* **1999**, *59*, 15990–16000.

[98] D. R. Lide, *CRC handbook of chemistry and physics : a ready-reference book of chemical and physical data*, CRC Press, **2004**.

[99] R. Ruer, *Zeitschrift für anorganische Chemie* **1906**, *51*, 391–396.

[100] A. Jabloński, S. Overbury, G. Somorjai, *Surface Science* **1977**, *65*, 578–592.

[101] H. Okamoto, T. B. Massalski, *Bulletin of Alloy Phase Diagrams* **1985**, *6*, 229–235.

[102] Y. Matsuo, A. Nagasawa, J. Kakinoki, *Journal of the Physical Society of Japan* **1966**, *21*, 2633–2637.

[103] Y. Kawasaki, S. Ino, S. Ogawa, *Journal of the Physical Society of Japan* **1971**, *30*, 1758–1759.

[104] T. Engel, H. Kuipers, *Surface Science* **1979**, *90*, 181–196.

[105] E. Stuve, R. Madix, C. Brundle, *Surface Science* **1984**, *146*, 155–178.

[106] E. Stuve, S. Jorgensen, R. Madix, *Surface Science* **1984**, *146*, 179–198.

[107] A. Noordermeer, G. Kok, B. Nieuwenhuys, *Surface Science* **1986**, *165*, 375–392.

[108] H. Amandusson, L.-G. Ekedahl, H. Dannetun, *Applied Surface Science* **2000**, *153*, 259–267.

[109] N. Seriani, J. Harl, F. Mittendorfer, G. Kresse, *The Journal of Chemical Physics* **2009**, *131*, 054701.

[110] M. Shipilin, J. Gustafson, C. Zhang, L. R. Merte, A. Stierle, U. Hejral, U. Ruett, O. Gutowski, M. Skoglundh, P.-A. Carlsson, E. Lundgren, *The Journal of Physical Chemistry C* **2015**, *119*, 15469–15476.

[111] M. Shipilin, A. Stierle, L. R. Merte, J. Gustafson, U. Hejral, N. M. Martin, C. Zhang, D. Franz, V. Kilic, E. Lundgren, *Surface Science* **2017**, *660*, 1–8.

[112] I. V. Yudanov, K. M. Neyman, *Physical Chemistry Chemical Physics* **2010**, *12*, 5094.

[113] F. Gao, Y. Wang, D. W. Goodman, *Journal of the American Chemical Society* **2009**, *131*, 5734–5735.

[114] R. Toyoshima, M. Yoshida, Y. Monya, K. Suzuki, B. S. Mun, K. Amemiya, K. Mase, H. Kondoh, *Journal of Physical Chemistry Letters* **2012**, *3*, 3182–3187.

[115] R. Toyoshima, N. Hiramatsu, M. Yoshida, K. Amemiya, K. Mase, B. S. Mun, H. Kondoh, *Chemical Communications* **2017**, *53*, 12657–12660.

[116] M. A. Languille, E. Ehret, H. C. Lee, C. K. Jeong, R. Toyoshima, H. Kondoh, K. Mase, Y. Jugnet, J. C. Bertolini, F. C. S. F. Aires, B. S. Mun, *Catalysis Today* **2016**, *260*, 39–45.

[117] L. Piccolo, A. Piednoir, J. C. Bertolini, *Surface Science* **2005**, *592*, 169–181.

[118] C.-W. Yi, K. Luo, T. Wei, D. W. Goodman, *The Journal of Physical Chemistry B* **2005**, *109*, 18535–18540.

[119] Z. Li, F. Gao, Y. Wang, F. Calaza, L. Burkholder, W. T. Tysoe, *Surface Science* **2007**, *601*, 1898–1908.

[120] C. J. Baddeley, R. M. Ormerod, A. W. Stephenson, R. M. Lambert, *The Journal of Physical Chemistry* **1995**, *99*, 5146–5151.

[121] V. Soto-Verdugo, H. Metiu, *Surface Science* **2007**, *601*, 5332–5339.

[122] F. Gao, D. W. Goodman, *Chemical Society Reviews* **2012**, *41*, 8009.

[123] H. Guesmi, C. Louis, L. Delannoy, *Chemical Physics Letters* **2011**, *503*, 97–100.

[124] A. Dhouib, H. Guesmi, *Chemical Physics Letters* **2012**, *521*, 98–103.

[125] M. Hebbache, M. Zemzemi, *Physical Review B - Condensed Matter and Materials Physics* **2004**, *70*, 224107.

[126] F. Tran, R. Laskowski, P. Blaha, K. Schwarz, *Physical Review B* **2007**, *75*, 115131.

[127] V. N. Staroverov, G. E. Scuseria, J. Tao, J. P. Perdew, *Physical Review B - Condensed Matter and Materials Physics* **2004**, *69*, DOI 10.1103/PhysRevB.69.075102.

[128] P. Janthon, S. Luo, S. M. Kozlov, F. Viñes, J. Limtrakul, D. G. Truhlar, F. Illas, *Journal of Chemical Theory and Computation* **2014**, *10*, 3832–3839.

[129] R. Peverati, D. G. Truhlar, *Philosophical Transactions of the Royal Society A: Mathematical Physical and Engineering Sciences* **2014**, *372*, DOI 10.1098/rsta.2012.0476.

[130] J. Klimes, D. R. Bowler, A. Michaelides, *J. Phys.: Condens. Matter* **2010**, *22*, 022201.

[131] D. D. Vasić Anićijević, V. M. Nikolić, M. P. Marčeta Kaninski, I. A. Pašti, *International Journal of Hydrogen Energy* **2015**, *40*, 6085–6096.

[132] W. Tyson, W. Miller, *Surface Science* **1977**, *62*, 267–276.

[133] R. Tran, Z. Xu, B. Radhakrishnan, D. Winston, W. Sun, K. A. Persson, S. P. Ong, *Scientific Data* **2016**, *3*, 160080.

[134] J. Kuntze, S. Speller, W. Heiland, A. Atrei, G. Rovida, U. Bardi.

[135] M. Chen, *Science* **2005**, *310*, 291–293.

[136] Y. F. Han, J. H. Wang, D. Kumar, Z. Yan, D. W. Goodman, *Journal of Catalysis* **2005**, *232*, 467–475.

[137] S. Ogura, M. Okada, K. Fukutani, *Journal of Physical Chemistry C* **2013**, *117*, 9366–9371.

[138] O. M. Løvvik, *Surface Science* **2005**, *583*, 100–106.

[139] H. L. Skriver, A. V. Ruban, J. K. Nørskov, L. Vitos, J. Kollár, *Progress in Surface Science* **2000**, *64*, 193–198.

[140] Y.-F. Han, Z. Zhong, K. Ramesh, F. Chen, L. Chen, T. White, Q. Tay, S. N. Yaakub, Z. Wang, *The Journal of Physical Chemistry C* **2007**, *111*, 8410–8413.

[141] A. Ruban, B. Hammer, P. Stoltze, H. L. Skriver, J. K. Nørskov in Journal of Molecular Catalysis A: Chemical, *Vol. 115*, **1997**, pp. 421–429.

[142] B. Hammer, O. Nielsen, J. K. Nørskov, *Catalysis Letters* **1997**, *46*, 31–35.

[143] X. Ke, G. J. Kramer, O. M. Løvvik, *Journal of Physics Condensed Matter* **2004**, *16*, 6267–6277.

[144] D. Teschner, A. Pestryakov, E. Kleimenov, M. Hävecker, H. Bluhm, H. Sauer, A. Knop-Gericke, R. Schlögl, *Journal of Catalysis* **2005**, *230*, 186–194.

[145] Z. Paál, U. Wild, R. Schlögl, *Physical Chemistry Chemical Physics* **2001**, *3*, 4644–4649.

[146] J. Shu, B. Bongondo, B. Grandjean, A. Adnot, S. Kaliaguine, *Surface Science* **1993**, *291*, 129–138.

[147] K. Otto, L. P. Haack, J. E. DeVries, *Applied Catalysis B Environmental* **1992**, *1*, 1–12.

[148] Z. Paål, R. Schlögl, G. Ertl, *J. Chem. Soc. Faraday Trans.* **1992**, *88*, 1179–1189.

[149] J. J. Yeh, I. Lindau, *Atomic Data and Nuclear Data Tables* **1985**, *32*, 1–155.

[150] R. Nyholm, M. Qvarford, J. N. Andersen, S. L. Sorensen, C. Wigren, *Journal of Physics: Condensed Matter* **1992**, *4*, 277–283.

[151] M. Todorova, E. Lundgren, V. Blum, A. Mikkelsen, S. Gray, J. Gustafson, M. Borg, J. Rogal, K. Reuter, J. N. Andersen, M. Scheffler, *Surface Science* **2003**, *541*, 101–112.

[152] P. Heimann, J. F. van der Veen, D. E. Eastman, *Solid State Communications* **1981**, *38*, 595–598.

[153] P. A. P. Nascente, S. G. C. De Castro, R. Landers, G. G. Kleiman, *Physical Review B* **1991**, *43*, 4659–4666.

[154] W. Olovsson, C. Göransson, L. V. Pourovskii, B. Johansson, I. A. Abrikosov, *Physical Review B* **2005**, *72*, 064203.

[155] P. Légaré, L. Hilaire, G. Maire, G. Krill, A. Amamou, *Surface Science* **1981**, *107*, 533–546.

[156] D. L. Weissman-Wenocur, P. M. Stefan, B. B. Pate, M. L. Shek, I. Lindau, W. E. Spicer, *Physical Review B* **1983**, *27*, 3308–3317.

[157] M. Okada, Y. Tsuda, K. Oka, K. Kojima, W. A. Diño, A. Yoshigoe, H. Kasai, *Scientific Reports* **2016**, *6*, 31101.

[158] L. S. R. Kumara, O. Sakata, H. Kobayashi, C. Song, S. Kohara, T. Ina, T. Yoshimoto, S. Yoshioka, S. Matsumura, H. Kitagawa, *Scientific Reports* **2017**, *7*, DOI 10.1038/s41598-017-14494-7.

[159] P. W. Chye, I. Lindau, P. Pianetta, C. M. Garner, C. Y. Su, W. E. Spicer, *Physical Review B* **1978**, *18*, 5545–5559.

[160] C. Klink, L. Olesen, F. Besenbacher, I. Stensgaard, E. Laegsgaard, N. D. Lang, *Physical Review Letters* **1993**, *71*, 4350–4353.

[161] S. Schintke, S. Messerli, K. Morgenstern, J. Nieminen, W.-D. Schneider, *The Journal of Chemical Physics* **2001**, *114*, 4206–4209.

[162] J. Wintterlin, R. Schuster, G. Ertl, *Physical Review Letters* **1996**, *77*, 123–126.

[163] B. C. Stipe, M. A. Rezaei, W. Ho, S. Gao, M. Persson, B. I. Lundqvist, *Physical Review Letters* **1997**, *78*, 4410–4413.

[164] H. Brune, J. Wintterlin, J. Trost, G. Ertl, J. Wiechers, R. J. Behm, *The Journal of Chemical Physics* **1993**, *99*, 2128–2148.

[165] B. G. Briner, M. Doering, H.-P. P. Rust, A. M. Bradshaw, *Physical Review Letters* **1997**, *78*, 1516–1519.

Appendices

Appendix A.

DFT results

Presented here are some results which were not presented in the main text. In addition calculated charge values for the individual atoms can be consulted.

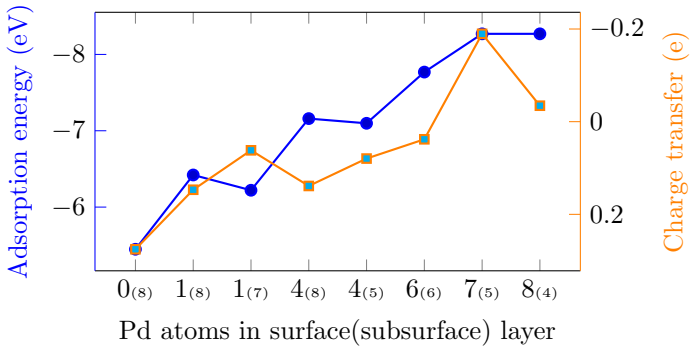

Figure A.1.: Calculated partial charge of the atoms adjacent to the carbon before adsorption. There is an increasing charge transfer to the atoms adjacent to the carbon with an increasing amount of Pd in the surface.

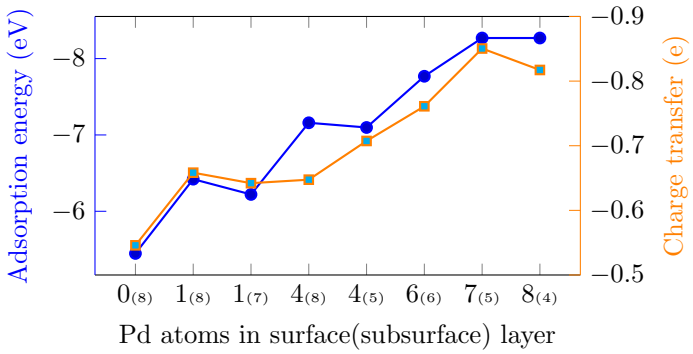

Figure A.2.: Calculated partial charge of the atoms adjacent to the carbon after adsorption. There is an increasing charge transfer to the atoms adjacent to the carbon with an increasing amount of Pd in the surface.

Table A.1.: Calculated charges (e) and partial charges (e) on atoms before and after adsorption.

		Before adsorption		After adsorption	
Structure	Position	Charge	Partial charge	Charge	Partial charge
0(8)	Below (Pd)	9.953	−0.047	9.853	−0.147
	North (Au)	11.040	0.040	10.899	−0.101
	West (Au)	11.121	0.121	10.903	−0.098
	South (Au)	11.040	0.040	10.899	−0.101
	East (Au)	11.121	0.121	10.901	−0.099
	Carbon			4.569	0.569
	Sum	54.275	0.275	58.023	0.023
1(8)	Below (Pd)	9.956	−0.044	9.807	−0.193
	North(Pd)	9.923	−0.077	9.770	−0.230
	West (Au)	11.095	0.095	10.921	−0.079
	South (Au)	11.065	0.065	10.920	−0.080
	East(Au)	11.108	0.108	10.923	−0.077
	Carbon			4.522	0.522
	Sum	53.147	0.147	56.863	−0.137
1(7)	Below (Pd)	9.903	−0.097	9.860	−0.140
	North(Pd)	9.923	−0.077	9.759	−0.241
	West (Au)	11.099	0.099	10.908	−0.092
	South (Au)	11.039	0.039	10.922	−0.078
	East(Au)	11.099	0.099	10.908	−0.092
	Carbon			4.485	0.485
	Sum	53.062	0.062	56.843	−0.157
4(8)	Below (Pd)	9.919	−0.081	9.796	−0.204
	North(Au)	11.144	0.144	10.997	−0.003
	West (Pd)	9.966	−0.034	9.781	−0.219
	South (Au)	11.144	0.144	10.997	−0.003
	East(Pd)	9.966	−0.034	9.781	−0.219
	Carbon			4.523	0.523
	Sum	52.139	0.139	55.875	−0.125

Continued from previous page

		Before adsorption		After adsorption	
Structure	Position	Charge	Partial charge	Charge	Partial charge
4(5)	Below (Pd)	9.928	−0.072	9.818	−0.182
	North (Pd)	9.913	−0.087	9.759	−0.241
	West (Au)	11.165	0.165	10.978	−0.022
	South(Pd)	9.913	−0.087	9.759	−0.241
	East(Au)	11.161	0.161	10.979	−0.021
	Carbon			4.472	0.472
	Sum	52.080	0.080	55.765	−0.235
6(6)	Below	9.932	−0.068	9.807	−0.193
	North(Au)	11.166	0.166	11.025	0.025
	West (Pd)	9.978	−0.022	9.793	−0.207
	South (Pd)	9.984	−0.016	9.823	−0.177
	East (Pd)	9.978	−0.022	9.791	−0.209
	Carbon			4.503	0.503
	Sum	51.038	0.038	54.741	−0.259
7(5)	Below (Pd)	9.949	−0.051	9.802	−0.198
	North (Pd)	9.971	−0.029	9.810	−0.190
	West (Pd)	9.975	−0.025	9.833	−0.167
	South (Pd)	9.923	−0.077	9.874	−0.126
	East (Pd)	9.993	−0.007	9.831	−0.169
	Carbon			4.526	0.526
	Sum	49.810	−0.190	53.675	−0.325
8(4)	Below (Pd)	9.890	−0.110	9.813	−0.187
	North(Pd)	9.995	−0.005	9.840	−0.160
	West (Pd)	10.043	0.043	9.845	−0.155
	South (Pd)	9.995	−0.005	9.840	−0.160
	East(Pd)	10.043	0.043	9.845	−0.155
	Carbon			4.463	0.463
	Sum	49.966	−0.034	53.646	−0.354

Appendix B.

XPS

Spectra obtained for O 1s are displayed in Figure B.1 and B.2. In Figure B.1 there is a large contribution coming from Pd $3p_{3/2}$ at 531.1 eV and O 1s at 528.8. These spectra were not calibrated as no Fermi edge was recorded for 610 eV, but they were shifted so that the largest peak corresponds to the binding energy for O 1s, 529 eV. Due to the low resolution of the spectra, O 1s was fitted using only one component, but in principle, if formation of the surface oxide was successful, it would posses components for two-fold and four-fold coordinated Pd atoms. It is worth noticing the less intense oxygen peak from grazing emission compared to normal emission. This is contradicting the Pd spectra where the oxygen derived components from grazing emisson is contributing significantly more to the measured signal than from normal emission. Another O 1s spectra was also

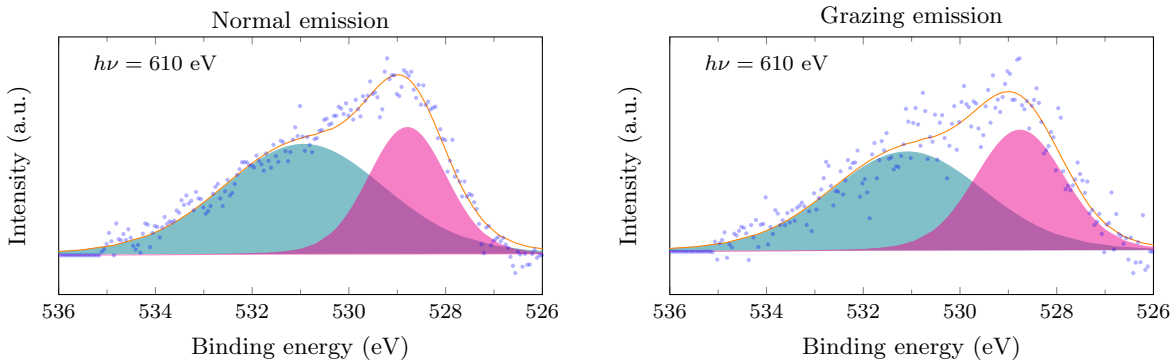

Figure B.1.: Spectra of O 1s obtained after oxidation. The peak has a large contribution coming from Pd 3p at 530.7 and an oxygen derived component at 528.8 eV.

acquired at a later stage with slightly better resolution, but due to the lack of a Fermi edge to calibrate with, they are both presented here in the Appendix.

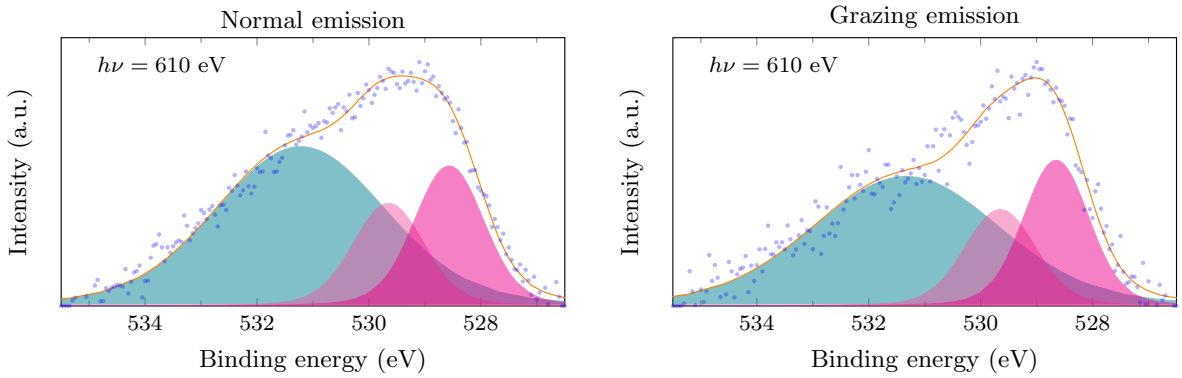

Figure B.2.: Spectra of O 1s obtained after oxidation. The peak has a large contribution coming from Pd 3p at 530.7 and two different oxygen derived components.

Appendix C.

Oxidation procedures

Here are the various procedures to obtain the Pd ($\sqrt{5}\times\sqrt{5}$)R 27° surface oxide presented. The coverage is mentioned in each table with a LEED image from the session attached.

Well-defined oxide pattern

P_O (mbar)		T_{start} (°C)	T_{end} (°C)	I_{start}	I_{end}	time (min)
5	$\cdot 10^{-5}$	318	275	1.95	1.55	18

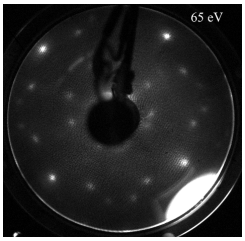

Well-defined oxide pattern

P_O (mbar)		T_{start} (°C)	T_{end} (°C)	I_{start}	I_{end}	time (min)
5	$\cdot 10^{-5}$	350	270	1.8	1.4	21

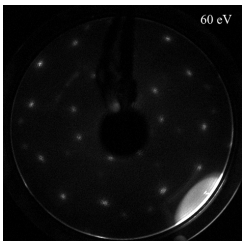

Weak oxide pattern

P_O (mbar)		T_{start} (°C)	T_{end} (°C)	I_{start}	I_{end}	time (min)
5	$\cdot 10^{-5}$	355	280	1.8	1.4	20

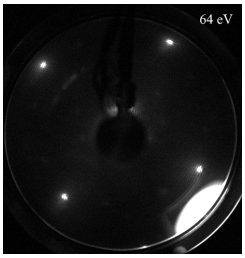

Weak oxide pattern

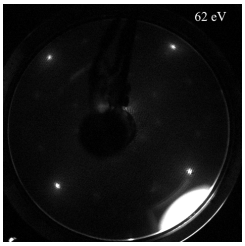

P_O (mbar)		T_{start} (°C)	T_{end} (°C)	I_{start}	I_{end}	time (min)
6	$\cdot 10^{-5}$	349	283	1.9	1.7	20

Well-defined oxide pattern

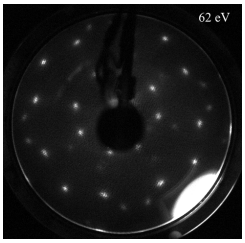

P_O (mbar)		T_{start} (°C)	T_{end} (°C)	I_{start}	I_{end}	time (min)
7	$\cdot 10^{-5}$	350		1.9	1.5	40

Well-defined oxide pattern

P_O (mbar)		T_{start} (°C)	T_{end} (°C)	I_{start}	I_{end}	time (min)
7	$\cdot 10^{-5}$	365	250	1.5	1.2	40

Appendix D.

Binding energies and cross sections for Pd, Au, O and C

Table D.1.: Binding energies and photoionization Cross Sections for Pd, Au, C and O. Data from [149].

				Excitation energy (eV)				
Z	Element	Orbital	B.E. (eV)	40.8	151.4	300	600	1486.6
6	C	1s	290.9			0.8591	0.168	$1.30\ 10^{-2}$
	C	2s	17.5	1.17	0.1714	$3.80\ 10^{-2}$	$7.30\ 10^{-3}$	$6.60\ 10^{-4}$
	C	2p	9	1.875	$4.70\ 10^{-2}$	$6.00\ 10^{-3}$	$7.50\ 10^{-4}$	$1.00\ 10^{-5}$
8	O	1s	536.8				0.4119	$4.00\ 10^{-2}$
	O	2s	29.2	0.8342	0.2984	$8.30\ 10^{-2}$	$1.80\ 10^{-2}$	$1.90\ 10^{-3}$
	O	2p	14.2	6.816	0.4037	$5.30\ 10^{-2}$	$6.10\ 10^{-3}$	$2.40\ 10^{-4}$
46	Pd	3s	619.8					$3.90\ 10^{-2}$
	Pd	3p	525.4				0.5612	0.1564
	Pd	4s	84.2		0.2184	0.1087	$3.90\ 10^{-2}$	$8.10\ 10^{-3}$
	Pd	3d	349.3				2.314	0.2197
	Pd	4p	54.6		0.4139	0.2887	0.1228	$2.50\ 10^{-2}$
	Pd	4d	8	32.52	0.4057	0.4789	0.16	1.60
79	Au	4s	619.8					$3.50\ 10^{-2}$
	Au	4p	524.4				0.337	0.1223
	Au	6s	91.1		0.1733	$9.10\ 10^{-2}$	$3.30\ 10^{-2}$	$7.70\ 10^{-3}$
	Au	4d	347.8				0.684	0.2739
	Au	5p	60.4		0.3168	0.1846	$8.50\ 10^{-2}$	$2.20\ 10^{-2}$
	Au	4f	109.4		0.6247	5.274	2.599	0.2511
	Au	5d	12.5	38.67	0.233	0.1186	$9.30\ 10^{-2}$	$2.60\ 10^{-2}$
	Au	6s	6.5	$2.80\ 10^{-2}$	$9.40\ 10^{-3}$	$3.50\ 10^{-3}$	$1.30\ 10^{-3}$	$2.90\ 10^{-4}$

Appendix E.

DFT input files

INCAR

```
INCAR created by Atomic Simulation Environment

ISTART = 0
ICHARG = 2

! Electronic relaxation
ENCUT = 550.000000 ! Cut-off energy for plane wave expansion
SIGMA = 0.050000   ! Smearing width
POTIM = 0.500000   ! = 0.5 if IBRION = 1,2,3
EDIFF = 1.00e-06   ! Accuracy for electronic groundstate
PREC = Accurate    ! Normal/Accurate/High
GGA = PE           ! GGA pseudopotentials of Perdew-Burke-Ernzerhof
ALGO = Fast        ! electronic minimisation algorithm
ISPIN = 1          ! ISPIN=1 non spin polarized calculations
MAXMIX = 40        ! Maximum number steps stored in Broyden mixer
ISMEAR = 0         ! Smearing of partial occupancies. Metals: 1; else < 1.
NELMIN = 8         ! Minimum # of electronic steps

! Ionic relaxation
EDIFFG = -1.00e-03 ! Tolerance for ions
NSW = 0            ! Max # of ionic steps
IBRION = -1        ! Algorithm for ions. 0: MD 1: QN/DIIS 2: CG
ISIF = 2           ! Relaxation. 2: ions 3: ions+cell

NPAR = 4           ! Number of cores
NSIM = 4           ! Number of bands that are optimized simultaneously
LWAVE = .FALSE.    ! Wavefunctions written to WAVECAR
LDIPOL = .TRUE.    ! Include dipole?
IDIPOL = 3         ! Direction of dipole moment:1,2,3
LSCALU = .FALSE.   ! Default
LPLANE = .TRUE.    !
LAECHG = .TRUE.    ! Default
LREAL = .FALSE.    ! Projection in reciprocal space

LORBIT = 11        ! Writes DOSCAR for use in DOS analysis
LCHARG = .TRUE.    ! Writes CHGCAR for use in Bader analysis
```

POSCAR

```
Au C Pd
1.0000000000000000
7.9893921950817193 0.0000000000000000 0.0000000000000000
0.0000000000000000 7.9893921950817193 0.0000000000000000
0.0000000000000000 0.0000000000000000 25.9867402438521431
Au  C  Pd
12  1  36
Selective dynamics
Direct
0.7484894857785326 0.2515435897341417 0.3095342032664094 T T T ! Au
.
.
.
0.0001735527915985 0.0017898629053816 0.3868191693582650 T T T ! C
0.0000000000000000 0.0000000000000000 0.0004082006753734 F F F ! Pd
.
.
.
0.7489663131532666 0.0002883946963179 0.3890419048821750 T T T ! Pd
```

KPOINTS

```
KPOINTS created by Atomic Simulation Environment
0
Gamma
7 7 1 ! For DOS calculations
0 0 0
```

Appendix F.

Python scripts

Extract DOS from selected folders and atoms. Py3

```
# -*- coding: utf-8 -*-
from __future__ import print_function
import numpy as np
import matplotlib as mpl
import os, sys, shutil
exitcode =os.system('vasp')
"""
Created on Tue May 8 19:17:04 2018

@author: Gaute
"""
from pymatgen.io.vasp.outputs import Vasprun # read vasprun.xml output file of VASP
from pymatgen.electronic_structure.core import Spin, OrbitalType
from pymatgen.electronic_structure.dos import Dos, CompleteDos
from scipy.integrate import simps

dbandoutput =open('d-band_ALL.txt', 'a')
directory_to_check =os.getcwd()
def my_function(directory):
print("Listing: " +directory)
directories =[os.path.abspath(x[0]) for x in os.walk(directory_to_check)]
directories.remove(os.path.abspath(directory_to_check)) # If you don't want your main
                                                        directory included

for i in directories:
  os.chdir(i)      # Change working Directory
  my_function(i) # Run your function

foldername =os.path.relpath(".","..")
filename =foldername+ '-d-DOS'+'.txt'
output =open(filename, 'w')
dosrun =Vasprun("vasprun.xml")  # Contains all the information about the simulations
spd_dos =dosrun.complete_dos.get_spd_dos()

E_F =dosrun.efermi
if foldername =="0(8)":   # Name of one of the folders containing vasprun.xml
  s =[43, 10, 6, 2,5]    # Which atoms to grab DOS from, check the CONTCAR file and
                                                    use the atomic numbers there
  name =["Below (Pd)", "North (Au)", "West (Au)", "South (Au)", "East (Au)"]  #
                                                    Position of the atoms
```

```
  tit="Energies, E_Fermi=%f, x_shifted, tot d_DOS, Below (), North (Au), West (Au),
                                        South (Au), East (Au)"%E_F

# Here you should list all the folders you want to extract the d-band from, the s-
                                        vector and also names

tDOS=dosrun.tdos.densities[Spin.up]
Energies =dosrun.tdos.energies

data =np.column_stack([Energies])
x_shifted =dosrun.tdos.energies -dosrun.efermi
print(foldername, dosrun.efermi)
data =np.column_stack([data, x_shifted])
struct =dosrun.complete_dos.structure
y1 =spd_dos[OrbitalType.d].densities[Spin.up]
data =np.column_stack([data, y1])
print("\n",foldername, "E_fermi = %f" %(dosrun.efermi), sep ='\t', file= dbandoutput)

d_center_vec=[]
for j in s:
  site_dos =dosrun.complete_dos.get_site_dos(struct[j])
  site_d_dos =dosrun.complete_dos.get_site_spd_dos(struct[j])
  y_site =site_d_dos[OrbitalType.d].densities[Spin.up]
  data =np.column_stack([data, y_site])
  dn_states =y_site*x_shifted
  d_center_simps =(simps(dn_states,x_shifted))/(simps(y_site, x_shifted))
  d_center_vec.append(d_center_simps)

print(name[s.index(j)], d_center_simps, sep='\t', file =dbandoutput)
if len(d_center_vec)>4:
  print("Surface atoms (4 atoms) \t Adjacent atoms (5 atoms)", file= dbandoutput)
  surface_average =sum(d_center_vec,-d_center_vec[0])/4
  adjacent_average =(sum(d_center_vec))/5
  print(surface_average, adjacent_average,sep='\t', file =dbandoutput)
np.savetxt(output,data, header=tit)
output.close()
dbandoutput.close()
```

Bader analysis, extracts information about selected atoms. Py3

```
#!/usr/bin/env
# -*- coding: utf-8 -*-
from __future__ import print_function
import numpy as np
import matplotlib as mpl
import os, sys, shutil
exitcode =os.system('vasp')
"""
Created on Tue May 8 19:17:04 2018

@author: Gaute
```

```
"""

from pymatgen.io.vasp.outputs import Vasprun # read vasprun.xml output file of VASP
from pymatgen.command_line.bader_caller import BaderAnalysis # Requires Bader
                                              executable from Henkelman's group to be in
                                               path. Only for Linux/OS x

from pymatgen.io.vasp.outputs import Chgcar
from pymatgen.io.vasp.inputs import Potcar

output_all =open("All_Bader_charges",'w')

directory_to_check =os.getcwd()
def my_function(directory):
  print("Listing: " +directory)
directories =[os.path.abspath(x[0]) for x in os.walk(directory_to_check)]
directories.remove(os.path.abspath(directory_to_check)) # If you don't want your main
                                                 directory included
for i in directories:
  os.chdir(i)      # Change working Directory
  my_function(i) # Run your function
  foldername =os.path.relpath(".","..")

  filename =foldername+ '_charges'+'.txt'
  output =open(filename, 'w')
  if foldername=="8(4)": # Name of the folder/structure you want to check
    s= [14, 24, 34, 47, 15] # Atomic index which you want to extract charge
                                               information about
    name =["Below (Pd)", "North(Pd)", "West (Pd)", "South (Pd)","East(Pd)"] # Position
                                               of these atoms
    check =1
  if os.path.isfile("vasprun.xml") is True and check ==1:
    bader =BaderAnalysis("CHGCAR",potcar_filename="POTCAR")
    for j in s:

      charge =bader.get_charge(j)
      charge_transfer =bader.get_charge_transfer(j)
      bader_summary =bader.summary

      print(foldername, name[s.index(j)], charge, charge_transfer, sep="\t", file=
                                               output_all)
      print(foldername, name[s.index(j)], charge, charge_transfer, sep="\t", file=
                                               output)
    output.close()
output_all.close()
```